Theses and Dissertations

December 2020

Novel Approaches to the Determination of Toxic Metals in Industrial Waste and Soil Extracts

Garrett Bruce Finn
University of Wisconsin-Milwaukee

NOVEL APPROACHES TO THE DETERMINATION OF TOXIC METALS IN INDUSTRIAL WASTE

AND SOIL EXTRACTS

by

Garrett Finn

A Thesis Submitted in

Partial Fulfillment of the

Requirements for the Degree of

Master of Science

in Chemistry

at

The University of Wisconsin-Milwaukee

December 2020

ABSTRACT

NOVEL APPROACHES TO THE DETERMINATION OF TOXIC METALS IN INDUSTRIAL WASTE
AND SOIL EXTRACTS

by

Garrett Finn

The University of Wisconsin-Milwaukee, 2020
Under the Supervision of Professor Aldstadt

Because of their environmental impact, the contamination and migration of

heavy metals is an important field of study. In this thesis, two novel methods for

measuring toxic metals over a broad concentration range in complex matrices were

successfully developed and applied to authentic samples. This research focused on

toxic metals in two disparate environments: industrial effluent and soil. The primary

work reported in this research focused on developing a Sequential Injection Analysis

(SIA) process monitor to measure metals in industrial process waste streams in near

real-time. Molecular Absorption Spectroscopy was used to determine levels of Zn and

several other metals. To increase throughput, the initial rate of absorbance was

studied, i.e., the slope of absorbance vs time was the signal. Various time frames for

the initial rate were investigated to further increase throughput and decrease reagent

use and chemical waste. The sample processing time was typically 12 minutes. The

concentration range studied was from 0.1 to 1.0 parts per million (mg L^{-1}). The LOD

for the SIA initial rate method was 0.1 ppm for Zn.

To test the prototype monitor, industrial effluent samples from the Milwaukee area were collected from a diverse group of manufacturing operations that involved metal processing. These samples were studied for factors that would influence analyte binding including ionic strength; pH; and presence of interfering elements.

Elemental analysis of the industrial samples by ICP-MS was conducted. The most common potential interferences were Fe, Ga, and Ba, with concentrations ranging from 1.68×10^3 to 2.10×10^5 ppb. The ICP-MS method showed excellent precision for example, the average amount of Br in one sample was found to be 1.13×10^5 ppb with a Student's t value at the confidence interval 95% (n=3) of 2.58×10^3 ppb (0.92% relative standard deviation).

The dye films used in the SIA prototype for Zn binding were based upon PAN (1-(2-Pyridylazo)-2-naphthalene). The dye films exhibited two noteworthy complications: (a) significant matrix effects were observed that caused instrumental drift resulting in irreversible alteration of the dye film's response to Zn, and (b) the physical detachment of the dye film from the glass slides in which they were affixed. These problems emphasized the need for more robust dye films, which must be addressed in future work to ensure the most accurate outcomes.

The second project in this thesis was an investigation of heavy metal deposition at a Civil War battlefield in Manassas, VA. This site is of interest because the battle resulted in heavy metal contamination over a brief period of time in a well defined area. The metals in the soil core fractions (Pb, Cu, and Hg) were extracted by applying a modified Sequential Extraction scheme followed by Inductively Coupled

Plasma-Mass Spectrometry (ICP-MS). Sequential Extraction was performed by subjecting the fractions to an optimized Microwave-Assisted Extraction (MAE) method. Additionally, ICP-MS allowed for an examination of other metals (Mn, Fe, Co, Ni, Cu, Zn, Ga, Ba, La, Ce, Au, Hg, Pb) present in the samples.

Interesting trends in the abundance and distribution of the target analytes were observed, particularly for Mn and Co. Co levels were higher than expected (4.91 x 10^4 ppb on average), while Mn had unexpected variability (2.94 x 10^5 on average with a range of 4.71 x 10^5 ppb). The levels observed for Mn, Fe, Co, Ni, Cu, Zn, Ga, Ba, La, Ce, Au, Hg, and Pb ranged from 4.36 to 4.44 x 10^3 ppm, which is consistent with normal background levels for soils in northern Virginia.

TABLE OF CONTENTS

LIST OF FIGURES:

LIST OF TABLES:

Chapter 1: Introduction

1.1 Overview

This project is based upon methods for measuring trace metals. There are two parts: development of a prototype process monitor by SIA and study of metals in soil by ICP-MS. In the following, after a discussion of general aspects of metal chemistry, the SIA and ICP-MS projects will be described.

1.2 Analytical Chemistry of Metals

Metals can be either vital or harmful depending upon both their identity and amount. For example, dietary Fe (in general, element symbols will be used without indicating their oxidation state, e.g., "Zn" instead of "Zn(II)") is an essential nutrient and a key component of hemoglobin. Hemoglobin is responsible for exchanging oxygen from the lungs with carbon dioxide throughout the body. Nevertheless, too much Fe may result in toxic effects which may cause symptoms that include diarrhea, vomiting with abdominal pain, and nausea. Zn is another critical dietary mineral. It is needed for growth and development. Zn also plays an important role in the catalytic activity of many enzymes and the synthesis of protein. There are risks to ingesting excessive amounts of Zn. Some of these symptoms are similar to those of Fe toxicity.[1]

Unlike Fe, some metals are of concern because they have no confirmed health benefits and are toxic; common examples include Pb, Cd, As, and Hg.[2] Not

surprisingly, Hg has no known beneficial value if consumed. The WHO (World Health Organization) considers Hg to be a major health concern. Elemental Hg (and especially methyl Hg) adversely affect both the central and peripheral nervous systems.[3] Interestingly, "Mad Hatter's Disease" was an occupational hazard in the 18th and 19th centuries. Haberdashers and milliners used $Hg(NO_3)_2$ for part of the hat-making process to convert rabbit and hare pelts into felt. Hat-makers brushed the fur with Hg, making the fur stick together to form felt. In doing so, toxic fumes were inhaled.[4-5] Multiple ailments resulted; including hallucinations, tremors, and emotional instability from toxicity through prolonged exposure.[6]

To protect water quality, the U.S. Environmental Protection Agency (EPA) sets strict standards for various metals including Cu, Hg, Zn, and Pb in industrial waste water.[7] Table 1 shows standards set for Primary Maximum Contaminant Levels (MCLs) for several metals, adverse health effects, and common sources of contamination.

National Primary Drinking Water Regulations ⊕EPA

Contaminant	MCL or TT[1] (mg/L)[2]	Potential health effects from long-term[3] exposure above the MCL	Common sources of contaminant in drinking water
Copper	TT[5]; Action Level=1.3	Short-term exposure: Gastrointestinal distress. Long-term exposure: Liver or kidney damage. People with Wilson's Disease should consult their personal doctor if the amount of copper in their water exceeds the action level	Corrosion of household plumbing systems; erosion of natural deposits
Lead	TT[5]; Action Level=0.015	Infants and children: Delays in physical or mental development; children could show slight deficits in attention span and learning abilities; Adults: Kidney problems; high blood pressure	Corrosion of household plumbing systems; erosion of natural deposits
Mercury (inorganic)	0.002	Kidney damage	Erosion of natural deposits; discharge from refineries and factories; runoff from landfills and croplands

Table 1. National Primary Drinking Water Regulations from the EPA, including Maximum Contaminant Levels (MCLs) and Health Effects. Adapted from Reference 8 for Pb, Cu, and Hg.

The EPA also sets Secondary MCLs. These secondary guidelines may not be enforced at the state level. For example, Secondary MCL levels for Cu and Zn are 1.0 mg/L and 5 mg/L respectively.[7]

Of course, the accurate measurement of metals is of critical importance in environmental, food, and clinical samples in particular because of their potential effect on human health. The most common methods are Atomic Absorption Spectroscopy (AAS), Inductively Coupled Plasma-Mass Spectrometry (ICP-MS), and ICP-Optical Emission Spectrometry (ICP-OES). The evolution of modern instrumental techniques over the past 150 years began with Flame Photometry to measure Na and K in a variety of samples.[9-10] Operating on the principle that excited atoms emit light of specific wavelength(s), this technique is limited to easily excited analytes (i.e.,

namely alkali and alkaline earth metals). In the 1920's, the introduction of Polarography by Heyrovský extended the range of analytes to heavy metals, including Pb and Cd. Like Flame Photometry, Polarography was limited in sensitivity, with detection limits in the parts per million (mg L^{-1}, ppm) range.[11]

Because of the limitations of these early methods, Flame Atomic Absorption Spectroscopy (FAAS) was introduced in the early 1960's. FAAS permitted the determination of a much greater range of analytes at much lower levels with better selectivity.[12] The EPA currently lists 25 elements that can determined by FAAS at low or sub-ppm levels.[13] With the advent of multi-element hollow cathode lamps (HCLs) as well as multi-lamp "turrets", the utility of FAAS improved dramatically.

In the 1980s, the introduction of ICP-MS revolutionized elemental analysis, enabling the greatest number of simultaneous determinations. It also possesses much lower limits of detection (LODs) than FAAS, reaching the low ng L^{-1} range for several heavy metals.[14]

The selectivity as well as the sensitivity is the hallmark of ICP-MS for two reasons. First, the ICP torch is remarkably energetic and reaches temperatures between 7,000 to 10,000 K. It thus is able to break apart many more kinds of metal complexes than FAAS, which only reaches temperatures between 2,000 to 3,000 K. Secondly, there are fewer interferences, especially for elements with lower Z values (elements possess vastly fewer isotopes than lines in their absorption spectra). Below is a comparison of spectra for the determination of Ce by ICP-OES and ICP-MS.
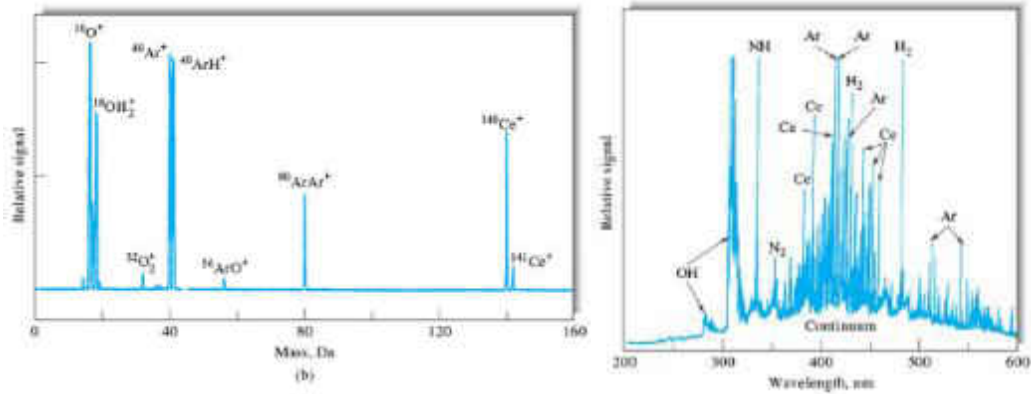
Figure 1. Comparison of ICP-OES spectrum for 100 ppm Ce (right), and ICP-MS spectrum for 10 ppm Ce (left).[15]

Another ICP-MS benefit that allows for better determinations of complex samples is that the lower LODs permit greater dilutions of samples. This can allow for one to "dilute away" interferences. In this way, more energy from the plasma can be devoted to breaking apart molecules and ionizing atoms when the analyte-to-solvent ratio is lower.

Thus modern analytical techniques for quantifying heavy metals are ICP-MS, AAS, and ICP-OES. These techniques are the state-of-the-art because they are generally precise, accurate, selective, sensitive, and robust. While practical in a research laboratory, these techniques are rare choices for industrial process monitoring because of their relative fragility, as well as expense, maintenance costs, and other logistical concerns.

1.3 Process Monitoring by SIA

On-line process monitors are used in industry as a means of quality control during manufacturing as well as verifying that waste has been properly treated. The most common process monitors are based upon colorimetric or electrochemical techniques. They are inexpensive, rugged, and require relatively low maintenance. However, their low sensitivity and inadequate selectivity are disadvantages. Selectivity can be particularly crippling because of the remarkably complex matrices of typical industrial samples, such as waste water. For example, because of direct sample contact, electrodes often become fouled or "passivated" by interfering species adsorbing to them, resulting in the response no longer being reliable. One solution is to design a flow-based sampling scheme that is placed before the monitor as a means to remove interfering species as well as preconcentrate the analyte. Various flow-based approaches have been used over the past five decades, starting with Segmented Flow Analysis (SFA) in the 1970's.[15] When SFA was introduced, microprocessors for analytical instruments were in their infancy, so instruments used simple control and timing schemes. Compared to modern automated instruments, the early SFA instruments were simple, with only two moving parts (an autosampler and a liquid pump). Zones of sample and reagent were pumped into a tube with air bubbles separating them (thus the term "segmented" flow). Because of the segmentation of the zones and the large diameter tubing, the flow was turbulent which allowed for efficient mixing of the two reactants. A detector would be placed downstream to measure the derivatized analyte.[16] In the 1980's, Flow Injection Analysis (FIA) was invented.[17] The most obvious difference between FIA and SFA is that FIA is

unsegmented. A background unsegmented "carrier" solution is continuously pumped through the instrument which is used to both push through the injected sample and simultaneously derivatize the analyte for downstream analysis. A more subtle difference is the ability of FIA to exploit the controlled dispersion of the zones such that kinetic method of analysis are possible.[18] In 1990, a variation of FIA dubbed Sequential Injection Analysis (SIA) was introduced, which greatly simplified the design of FIA instruments by reducing the hardware to only one pump and one valve.[19]

SIA instruments have become the "state-of-the-art" for flow-based on-line monitoring. The methods which can be developed using SIA as a platform are versatile and can often provide the needed selectivity and sensitivity. They are also more practical because they are relatively inexpensive, possess low reagent consumption and waste generation, have a small footprint, and can be operated by relatively unskilled technicians. However, another advantage with using an SIA instrument is automated sample manipulation. Multiple samples can be automatically introduced in precise volumes and then manipulated in the micro-scale conduits to effect a wide variety of sample pretreatment approaches.[20]

A schematic diagram of an SIA instrument (Figure 2) reveals the simplicity of the design. The instrument consists of: a bi-directional Pump (P), a Holding Coil (HC), a Multi-Position Valve (MPV), a Flow Cell (FC), and a Detector (D).
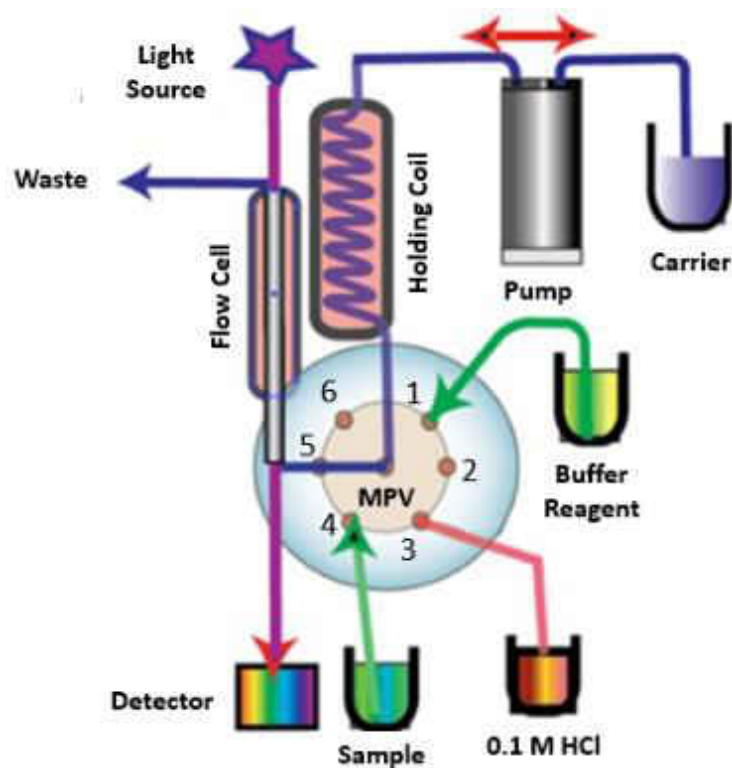
Figure 2. Schematic diagram of an SIA instrument. Adapted from Reference 21 .

Dispersion plays a critical role when derivatizing or intentionally diluting a sample.[22] This phenomenon would be key if the chemosensor was soluble (i.e., suspended in the carrier). However, this approach would increase reagent use and operating costs, which is undesirable in an industrial setting. Instead, chemosensor molecules immobilized on a glass slide were chosen because they could last several months before replacement.[23] Additionally, on-line chemical reactions were not performed in this project, and the possibility of on-line sample dilution was not required.

It may be tempting to picture the MPV connecting the P to various samples, loading them as discrete rectangular slugs into the HC for temporary storage, and

finally delivering them to the FC for spectrophotometric (or other) analysis. Despite

possessing tubing with a small inner diameter (i.d.) to create laminar conditions, the

fluid dynamics are more complex than this simple image suggests. This is shown for a

single zone of sample flowing in a continuous direction in Figure 3. Initially, the

simple image is the correct one (Figure 3, inset A). This state of affairs soon breaks

down because streamlines closer to the walls of the tubing move slower than the

streamlines at the center because of wall friction.[24] This leads to the classic "bullet"

shape (Figure 3, inset B). Assuming that enough of a concentration gradient exists for

rapid diffusion (Fick's law), the "bullet" smooths out and conforms to a Gaussian

distribution (Figure 3, inset C).

While dispersion is a force to be fought against in liquid chromatography (LC),

SIA can take advantage of it for performing on-line chemical reactions. For example,

Figure 4 is broken into five parts. In (A), the sample (red) is aspirated into the HC. In

(B), the sample is followed by a reagent (blue), and they react at their interface

forming a product (yellow). In (C), as the two zones continue to be aspirated, they

further disperse into one another forming more product. In (D), the flow is reversed

both to promote further mixing as well as to direct the product towards the detector.

Finally, in (E), depending upon the rate of the reaction, flow may be either

continuous (for a rapid reaction) through the detector's flow cell, or stopped when

the product enters the flow cell as a means to monitor the kinetics of the reaction

(known as "stopped flow SIA").
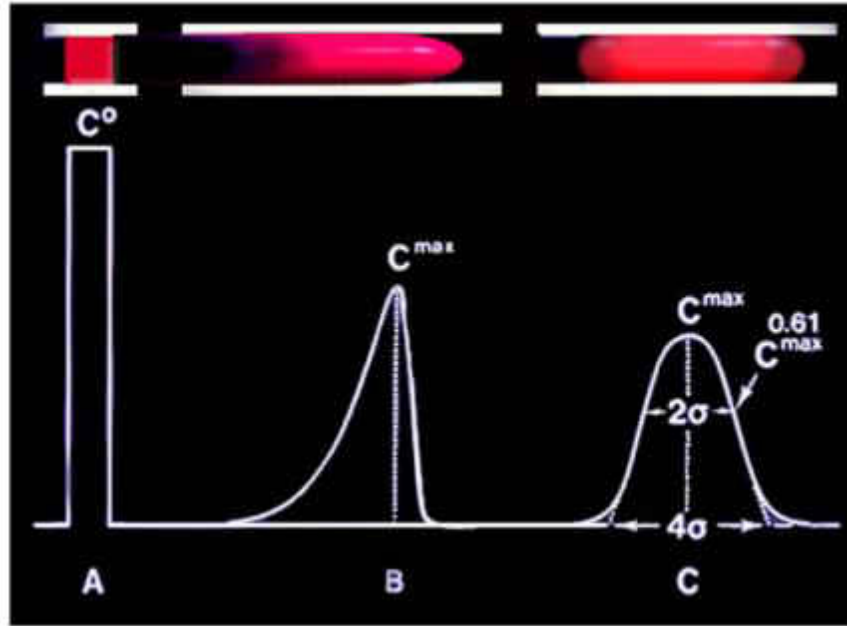
Figure 3. Timeline of concentration gradient in SIA.[25]

An experimental design and response for the determination of histamine by SIA is shown in Figure 5. In addition, on-line dilutions can be performed in a similar manner with a non-reacting diluent taking the place of the reagent.
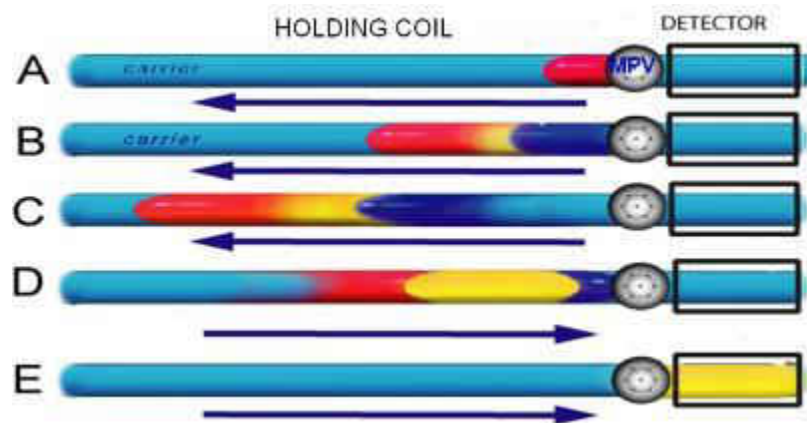
Figure 4. Illustration of advantageous use of SIA dispersion. [26]
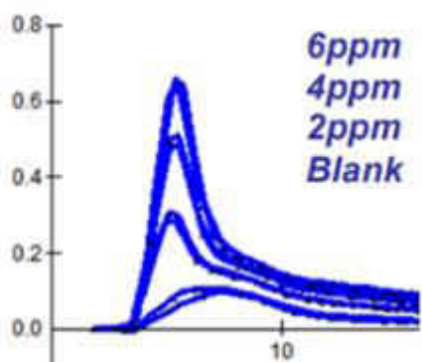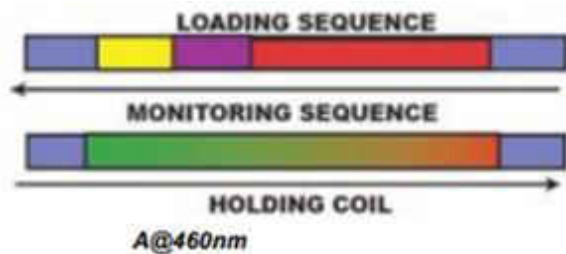
Figure 5. Example of a stop flow SIA experiment for the enzymatic assay of histamine. Adapted from Reference 22.

Yellow = Indicator

Purple = Enzyme

Red = Sample

Because of the versatility, automation capability, low reagent use, and reduced waste generation, SIA instruments are used widely as process monitors. Examples include determination of D-Lactic Acid in fermenting broth and TNT in soil samples.[27]

Additionally, immobilized chemosensor dye films have been used for metal determinations over the past few decades.[28] Agarose carbon dot hydrogel films have been shown to respond to several metal ions in low concentrations (1 pM for Cr^{+6}, 0.5 μM for Cu^{+2}, and 0.5 nM for Fe^{+3}, Pb^{+2}, and Mn^{+2}).[29] However, this method required a 12 hr incubation with the sample before determination of the metals. It should be noted that these results were obtained for standards, and not remarkably complex samples such as industrial wastewater.[29] Binding can be altered by solution conditions, such as pH and ionic strength. Additionally, interfering species which may

irreversibly alter the structure of the chemosensor molecules in the dye film or may cause the film to detach from its support can be present.

Despite the greater selectivity and sensitivity of fluorescence-based techniques over absorbance-based techniques, absorbance-based dyes are preferable to fluorescence-based dyes because fluorescing dyes are prone to undergo photobleaching.[30-31]

Figure 6 is a diagram of a conventional Z cell used for colorimetric detection. The solution flowing through an instrument equipped with such a cell flows in a "Z" shaped path (i.e., it enters A and exits B). Meanwhile, the source and detector are connected using optical fibers at points C and D. This allows for absorbance spectra to be collected for a solution which is either continuously flowing or a solution stopped between points C and D.
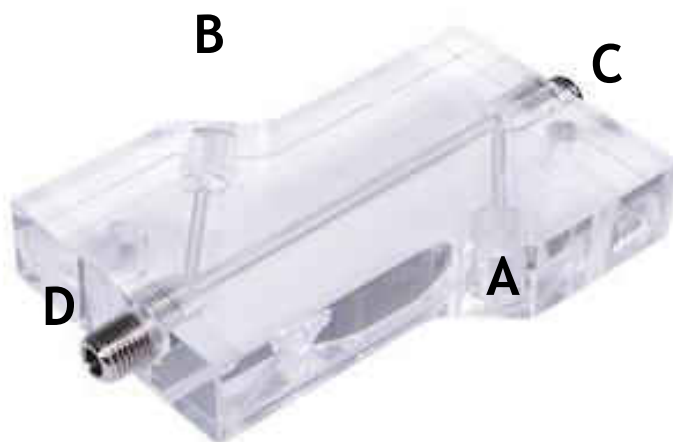
Figure 6. Photograph of a Z-cell used for colorimetry. Adapted from Reference 32.

1.4 Trace Metals in Civil War Battlefield Soils

Brawner Farm is located in the northwest corner of Manassas National Battlefield Park, which is approximately 30 miles west of Washington D.C. On August 28, 1862, a battle broke out between Confederate soldiers under the command of General Thomas "Stonewall" Jackson and Union soldiers under General Rufus King. The two-hour battle ended in a costly stalemate with one in three killed or wounded.[33]

A combination of unique factors makes Brawner Farm an exemplary environment for studying metals in soil because: (1) battle lines remained relatively fixed through most of the battle (within approximately 5 m); (2) the volume of weapons debris was deposited in a very short time frame (the engagement lasted about two hr) and was substantial because of the amount of rifle fire (as reflected by the high casualty rate); and (3) there was no additional fighting after the battle and the area remained undeveloped and uncultivated.[34] The deposition of Cu, Pb, and Hg in the weapons debris generated a linear distribution along the firing lines. These factors provide a singular opportunity to study the abundance, distribution, and transport of toxic metals in soil that has been undisturbed for ~150 years.

Researchers have been able to collect and identify physical remnants which included various accoutrements (e.g., buttons, buckles, etc.) and weapons debris (e.g., shell fragments, bullets, percussion caps)[33] as well as "chemical signatures" left behind in the soil by firearms (Pb, Cu, and Hg).[35-36] This has offered the scientific

community the ability to better understand the migration of toxic metals, with a specific focus on Pb, Cu, and Hg.

Percussion caps were used by both the Union and Confederate troops in their muzzle-loading firearms.[37] They were made from small copper cylinders with a closed end holding mercury fulminate - $Hg(CNO)_2$ - encased by foil paper. $Hg(CNO)_2$ is classified as a "primary" explosive because it is extremely shock-sensitive.[38] Percussion caps were superior to the previously used flintlock ignition system because they were more reliable and weather resistant.[39] The percussion caps were single use, and would be dropped after firing, giving rise to the elevated soil levels of Cu and Hg studied in this project.

Hg migration and deposition have long been studied because of Hg's negative impact on the environment. There have been an incredible number of studies undertaken to measure Hg transport in soils (for example, see References 40 and 41). Typical Hg transport studies measure atmospherically deposited Hg and then perform a mass balance between "through fall" (rainfall in a forest that reaches the ground) and "litter fall" (dead plant material that has fallen to the ground).[42] While revealing valuable information, such as the extent to which various species of trees accumulate Hg in their leaves, these studies are limited in scope.

An interesting and unique experiment done in Canada yielded important information that sought to answer questions such as "How long does it take newly deposited Hg to enter a watershed?"[40] In the "Mercury Experiment to Assess Atmospheric Loading in Canada and the United States" (METAALICUS), an isotopically

enriched Hg solution was manually deposited to mimic either a dry or a wet deposition (rain) event. Figures 7 and 8 show the experimental area where such a study occurred and the timeline for the project.

Figure 7. Timeline for METAALICUS study.[43]

Figure 8. Aerial photograph of Experimental Lakes Area 658.[44]

Through ICP-MS's superior LOD and ability to distinguish Hg isotopes, the experimentally applied Hg was tracked alongside the naturally occurring "old" Hg. Studies based upon this design have been used to study the photoreduction of atmospherically applied methyl Hg to elemental Hg on leaves,[45] investigate foliar flux of Hg originating from the atmosphere[46] and from underlying vegetation,[39] as well as accumulation[47] and elimination[48] of Hg in fish. Advantages include the ability to track Hg over longer periods of time than a single season, and the ability to compare behaviors for "new" and "old" Hg deposits. While this design is sufficient for fates of

newly deposited Hg in fish, and "new" dry/wet depositions of Hg, these studies are limited to a few decades.

The Brawner Farm project adds valuable information that was not addressed by the METAALICUS work. Hg deposition at Brawner Farm took place over 150 years ago and was accompanied by a much heavier level of contamination, giving an additional piece to the continuing work on how Hg transport in soil occurs; transformations which the Hg undergoes; potential environmental implications; and how those implications can be addressed and possibly mitigated.

Thesis:

In this thesis, a description of the quantification of toxic metals in two distinct environments will be presented to answer these questions:

(a) Can real-time measurements be made to make better decisions in addressing heavy metal contamination in process waste water?

(b) Can an assessment of the migration of toxic materials in soil be made?

The primary objective of this study was to develop novel methods to measure several toxic metals (Zn, Pb, Cu, Hg) over a broad concentration range in complex matrices. These metals were investigated in two quite different sample types: 1) industrial process effluents, and 2) battlefield soil samples.

The two matrices not surprisingly necessitated different procedures to identify and quantify the target metals. Specifically, for the first part of this thesis, a new

method based upon Molecular Absorption Spectroscopy was developed to determine ppm levels of Zn in the process effluent. For the Brawner Farm samples, the European Union's (EU) Community Bureau of Reference (BCR) Sequential Extraction procedure was modified and applied to fractionated core samples by using an optimized Microwave-Assisted Extraction (MAE) method. ICP-MS was used for Pb, Cu, and Hg for determining low parts per billion (μg L^{-1} or ppb) levels.

Based upon what was learned in these studies, industrial and regulatory organizations will be able to more accurately make economically and ecologically sound decisions and evaluate the risk imposed by contaminated waste materials and sites on surrounding communities.

Chapter 2 Experimental

2.1 Materials

2.1.1 Reagents for SIA Studies

Standard metal solutions were prepared by a dilution of various 1,000 ppm (mg/L) atomic absorption standards sourced from Sigma Aldrich. Buffers were prepared at pH 7.4 with equimolar amounts of 3-(N-Morpholino)propanesulfonic acid (MOPS) and MOPS sodium salt; also purchased from Sigma Aldrich. Early experiments revealed an interference caused by trace metal impurities in the buffer reagents, so buffer reagents were treated with Chelex 100 ion-exchange resin (Bio-Rad, Hercules, CA, USA) to remove these impurities.[49] Triton X-100 surfactant (Sigma Aldrich) was used to reduce scattering when aggregation was present. Reagent water with a resistivity of 18.2 MΩ cm^{-1} was used for all experiments.

2.1.2 Reagents for ICP-MS Studies

All soil extracts were prepared with Reagents for BCR Studies (section 2.3.1) and Reagents for Sequential Extraction Studies (section 2.3.2). Subsequent preparation of soil extracts for analysis by ICP-MS consisted of a 1:20 dilution in 1% (v/v) HNO_3 (Trace Metal Grade supplied from Fischer Scientific) with 18.2 MΩ cm^{-1} water.

2.1.2.1 Labware for SIA Studies

Plastic labware was used to minimize interference from metal impurities. Samples were typically prepared in Class A volumetric flasks (VITLAB PMP, Grossostheim, Germany). All labware was cleaned using Citranox detergent (Alconox, White Plains, NY, USA). Additionally, glassware was immersed in 5% (v/v) HNO_3 for a minimum of 48 hr, and then rinsed with reagent water to remove metal contaminants. Eppendorf micropipettes were used for transferring small volumes.

2.2 Instrumentation

2.2.1 SIA

2.2.1.1 Flow Cell Design

A schematic diagram of the SIA instrument is shown in Figure 9. SIA is a microscale approach to continuous flow analysis that is based upon a single bi-directional pump and multi-port selection valve. The FC was designed to incorporate the flow path of a conventional 'Z' cell, but also had a 1.076 mm thick well drilled to accommodate the 1 mm thick glass slide, and the 25.4 micron thick film, thus providing a small excess. The flow would enter at an angle with respect to the film and be dispensed to waste. The optics were oriented perpendicular to the film's surface in order to measure its absorbance.

2.2.2 SIA System Configuration

The FC well had excess space drilled to account for inconsistencies in glass slide manufacturing and lab preparation (cutting slides to size). A small piece of polyethylene tape (76.2 40 microns) with a hole punched in it was place over the film for several reasons: (a) the tape served as a gasket for the cell; (b) eliminated dead volume on the sides of the glass; and (c) kept the film aligned with the optics. The flow was originally brought in at the 90° angle to the film, however, this caused film destruction more often.[50] The flow coming in at the 45° angle was found to be less destructive.[50]

2.2.3 Quantitation Method

2.2.3.1 Dye Film Accumulation

The method used for analysis involved three steps. First, the film was rinsed with 0.1 M HCl to remove any bound metal. Second, the film was equilibrated with 0.10 M MOPS (pH 7.4 with 2 mM Triton X-100). Finally, the baseline was taken, and the buffered metal solution introduced. It was found that the flow rate needed to be kept under 20 µL/s to avoid film delamination.[50] The typical procedure was an acid wash of ~2.5 mL at 15 µL/sec followed by 1.5 mL of carrier solution (buffer) at the same rate. The metal solution was then aspirated and dispensed. Typical volumes were 2.0 mL of sample/standard at a flow rate of 12 µL/sec, followed by 0.5 mL of the 0.1 M HCl and 1.5 mL of buffer to re-equilibrate the film at the same rate.

The procedure was altered slightly based upon experimental conditions. In typical operation, after initially priming each line with the respective solution, the FC was washed with ~2 mL of 0.1 M HCl to remove any residual metal, followed by ~1.5 mL of buffered carrier to equilibrate the protonation sites on the dye at neutral pH.
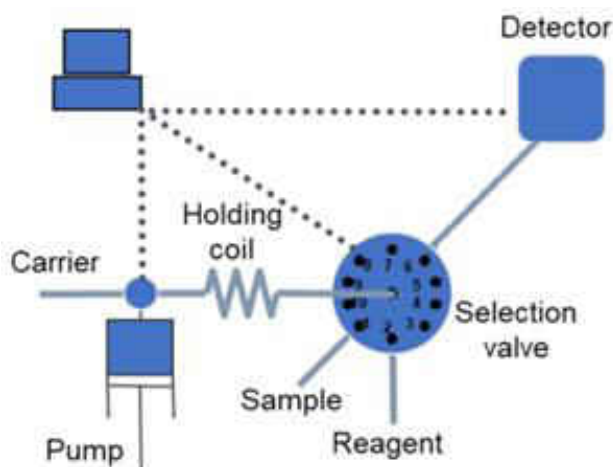
Figure 9. Schematic diagram of the SIA system. The selection valve has multiple positions, and is used to cycle between reagents, samples, standards, etc. The instrument is controlled via a computer interface (top left corner) that allows the user to easily manipulate zones of fluid to a detector. Note: the FC is considered a part of the detector. Adapted from Reference 50.

Figure 10. Photograph of the flow cell used in SIA, showing the optical path as well as the 'Z'-type flow path.[50]

Pre – Acid Wash	15 μL / sec, 4 min 27 sec, 6 min 40 sec including zone loading	
1500 μL 0.05 M MOPS buffer (pH 7.2), 300 ppm NaCl, 2mM Triton-X 100 Surfactant	2500 μL 0.1 M HCl, 2 mM Triton-X 100 Surfactant	#1

Sample / Standard	12 μL / sec, 5 min 34 sec, 7 min 47 sec including zone loading		
1500 μL 0.05 M MOPS buffer (pH 7.2), 300 ppm NaCl, 2mM Triton-X 100 Surfactant	500 μL 0.1 M HCl, 2 mM Triton-X 100 Surfactant	2000 μL 100 ppb Zn 0.05 M MOPS (pH 7.2), 300 ppm NaCl, 2 mM Triton-X 100 Surfactant	#2

Figure 11. Experimental design. Analysis would alternate between Pre – Acid Wash and Sample / Standard runs to ensure removal of previous run's metal from dye film.

2.2.3.2 Reagents for ICP-MS Studies

Samples and standards were prepared in 1% (v/v) HNO_3 within 12 hr of analysis. Sample aliquots were taken directly from labeled industrial effluent sample bottles and diluted 1:100 (v/v) in plastic 25 mL volumetric flasks. Zn standards were between 0.1 ppb and 2.0 ppb. Samples and standards were analyzed by Shimadzu ICP-MS 20-30 for M/Z values between 50 and 238. All measurements were made in triplicate, with three samples of blank (yielding nine measurements) being taken to determine limit of detection.

Before use, the instrument was turned on, and the torch allowed to stabilize for a minimum of 30 min. A 1:100 dilution of stock ICP-MS tuning solution (diluted in 1% v/v HNO_3) was used to auto-tune the instrument's torch position, gain voltage, lens voltage, and mass resolution before each day's analysis.

The ICP-MS instrument protocol for the peristaltic pump is shown in Table 2.

	Low	High
Wash Rinse	10 sec	30 sec
Sample Rinse	60 sec	60 sec
Rotation Speed	20 rpm	60 rpm

Table 2. ICP-MS Sample Introduction Protocol. Wash Rinse solution consisted of a tank of 2% (v/v) HNO_3 in 18.2 MΩ-cm water.

As the ICP-MS instrument settings did not allow for flow rate to be set in more traditional units (mL/sec), an additional experiment was performed. An ICP-MS sample tube was filled with 18.2 MΩ-cm water and weighed. Then the instrument was programmed to draw up the "sample" at a set speed and timed for 60 sec. Afterwards, the ICP-MS sample tube was weighed again, and the difference used to determine flowrate (in mL/sec). All measurements were made in triplicate.

Speed (rpm)	Average (mL/min)	s	R. Stdev	95% (n=3)
20	0.449	0.00658	1.47	0.0164
60	1.31	0.00783	0.598	0.0195

Table 3. ICP-MS flow rate experiment data. Density of water was approximated at 1.0 g/mL.

Time				
Peristaltic pump rotates at 20 rpm (0.449 mL/min) for 10 seconds and injects Wash solution	Peristaltic pump rotates at 60 rpm (1.31 mL/min) for 30 seconds and injects Wash solution	Peristaltic pump rotates at 20 rpm (0.449 mL/min) for 60 seconds and injects Sample solution	Peristaltic pump rotates at 60 rpm (1.31 mL/min) 60 seconds and injects Sample solution	Analysis
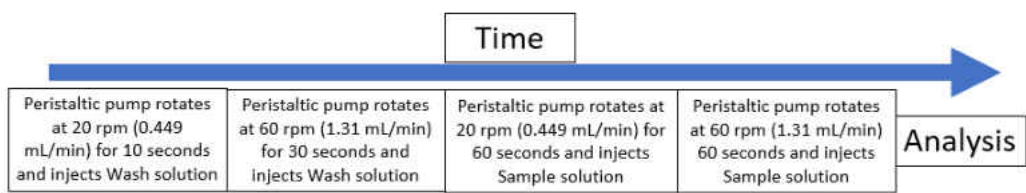
Figure 12. ICP-MS Sample introduction protocol flow chart (not to scale).

2.3.1 Reagents for BCR Studies

Chemical reagents were Trace Metal™-grade (or higher) for the reagent acids, while the other reagents were ACS-grade or higher and sourced from Fisher Scientific; unless otherwise specified. A Milli-Q ® Gradient water purification system (Millipore, Marlborough, MA) was used to prepare reagent water (18.2 MΩ-cm) from in-house deionized water. Glassware and plasticware were washed with Citranox™ detergent (Alconox, New York, NY) and soaked in 5% (v/v) HNO_3 (Sigma-Aldrich, St. Louis, MO) for at least 48 hr, and then rinsed copiously with reagent water.

2.3.2 Reagents for Sequential Extraction Studies

2.3.2.1 Exchangeable Fraction: Mobile Hg

The extractant solution for the "exchangeable" fraction of the soil samples consisted of aqueous 0.010 M Calcium Chloride dihydrate (Sigma-Aldrich), which could be stored indefinitely at room temperature in glass.

24

2.3.2.2 *Acid-Soluble Fraction: Carbonate-bound Hg*

The extractant solution for the "carbonate-bound" fraction of the soil samples consisted of 0.11 M acetic acid prepared from glacial acetic acid (Sigma-Aldrich), which could also be stored indefinitely at room temperature in HDPE.

2.3.2.3 Acid-Reducible Fraction: Oxides-bound Hg

The extractant solution for the "oxides-bound" fraction of the soil samples consisted of 0.50 M hydroxylamine hydrochloride with 1.0 M HNO_3 (Fisher Scientific) prepared from reagent hydroxylamine hydrochloride (Sigma-Aldrich). The extractant solution for the "oxides-bound" fraction of the soil samples was prepared on the day of use.

2.4.1 Soil Core Sampling

Soil cores were taken at the Brawner Farm battlefield in 2004 and 2007 by Dr. J. Aldstadt (a total of four separate trips). Figure 13 shows a map of the positions of the units involved in the battle. Samples were collected so as to follow a straight line which would include the relatively flat area where primary infantry conflict occurred, then continued down the subsequent slope of the hill to determine the extent of Hg migration in that direction (i.e., both horizontal and vertical migration). Specifically, the sampling location was chosen such that core samples transected the battle line starting at ~25 yards north of the battle line and continued in a straight line for ~125

yards. The sampling line was located ~46 yards east of a National Park Service (NPS) building that was built upon the original foundation of the Brawner family's farmhouse. South of the conifer trees, the terrain begins to slope steeply and then gradually level off near the Lee Highway (Warrenton Turnpike) ~700 yards from the ridge.
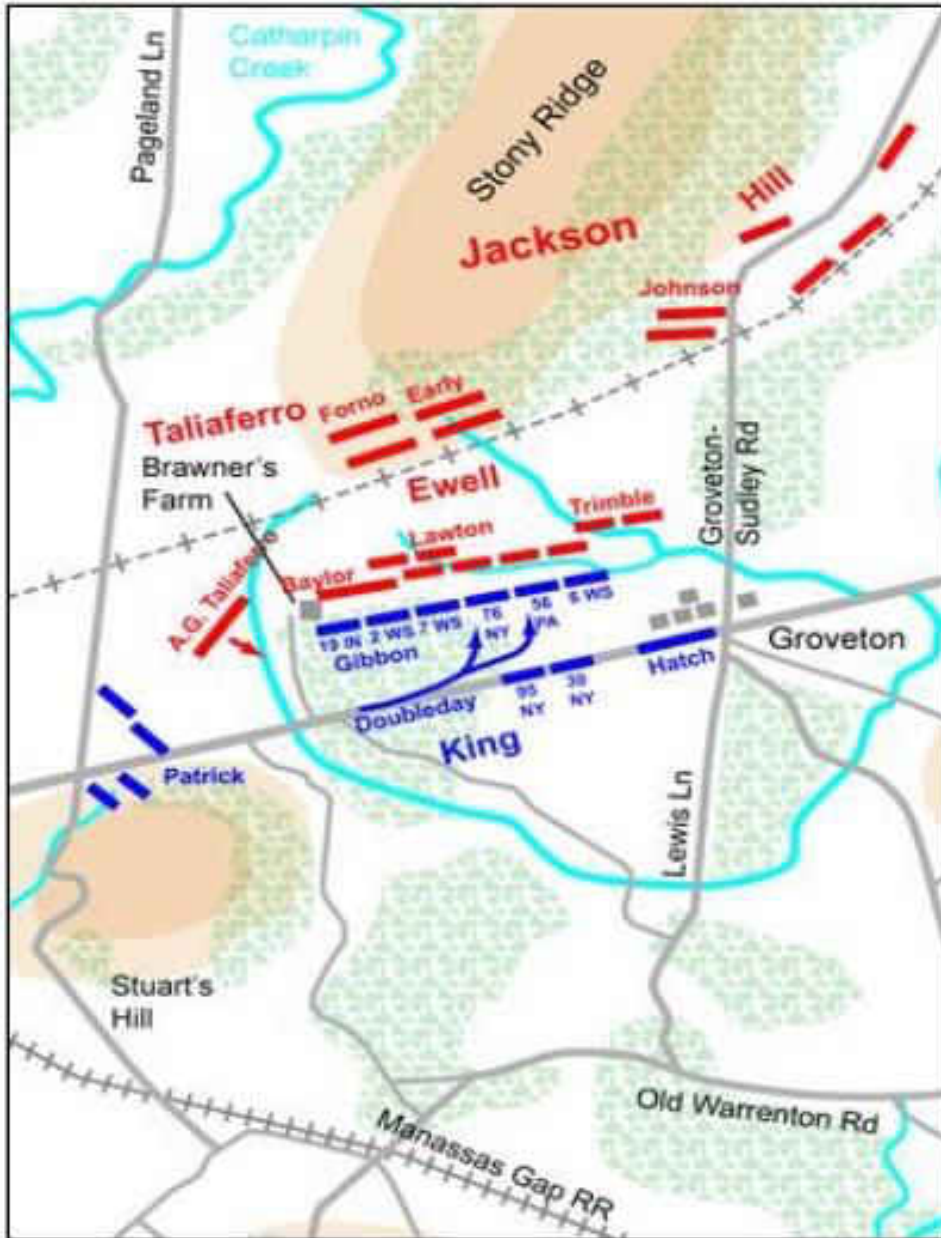
Figure 13. Unit positions at Brawner Farm. Map to troop movements at the Brawner Farm on the evening of August 28, 1862. Adapted from Reference 51.

Figure 14 shows the sampling (transect) line looking south toward the Warrenton Turnpike.

Figure 14. Photograph of sampling area. View looking south along the sampling line (orange flags); the nearest flag is sampling site #10. The Warrenton Turnpike can be seen in the distance. The yew trees and informational plaques can be seen at center left and right, respectively. Photograph by J. Aldstadt, August 2004.
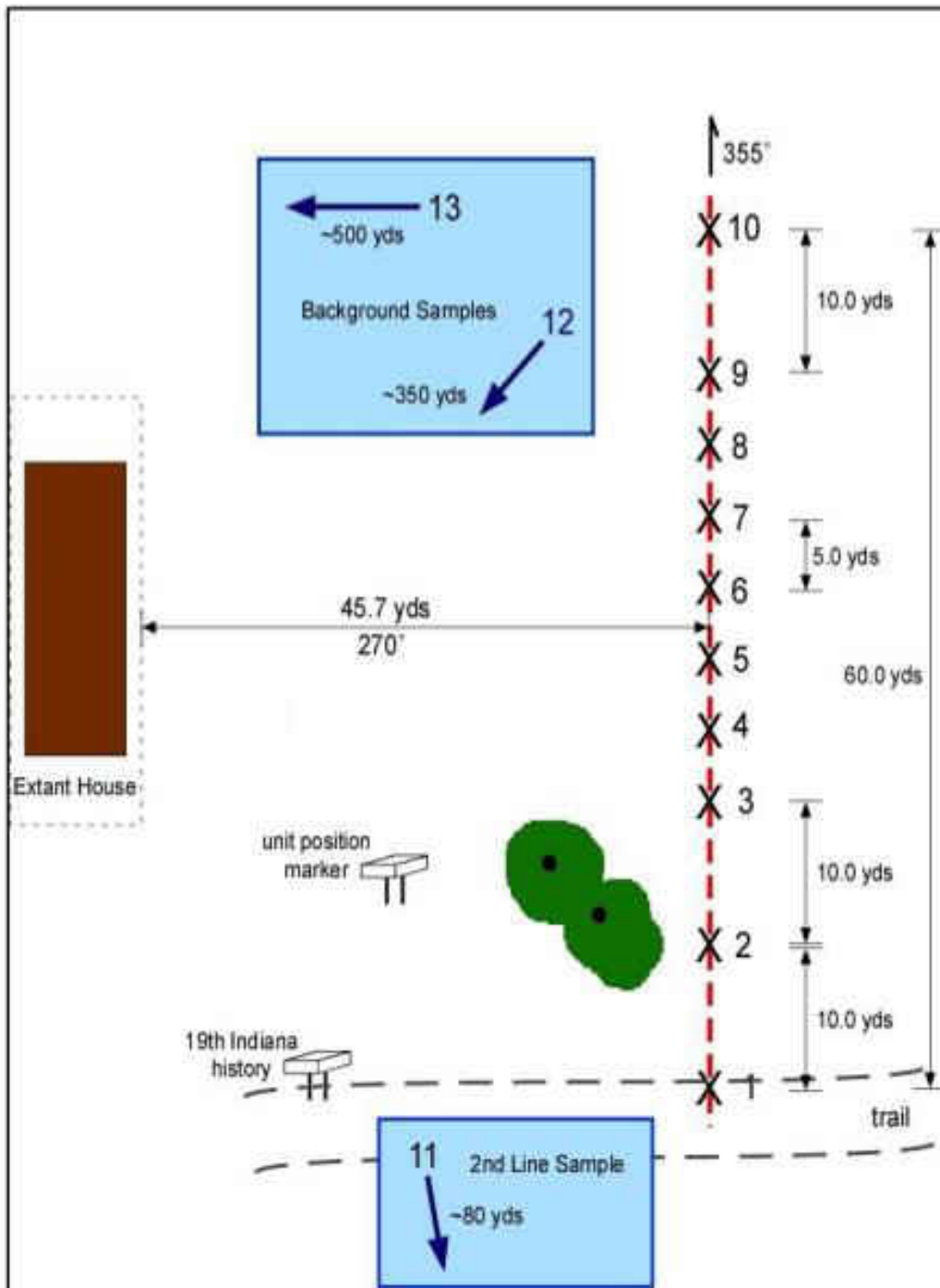
Figure 15. Map of location of soil core samples in the area where the heaviest fighting occurred; sampling sites 12-24 continue south at 10-yard intervals.[36]

Figure 16 shows a view looking west perpendicular to the transect line.

Figure 16. Photograph of sampling area. View looking west toward the reconstructed Brawner house, perpendicular to the sampling line. The informational plaques and yew trees can be seen at center left and right, respectively. Photograph by E. Christianson, June 2008.

Figure 17. Photograph of a typical soil core sample. The top of the core is orange-capped. Photograph by T. Grundl, September 2007.
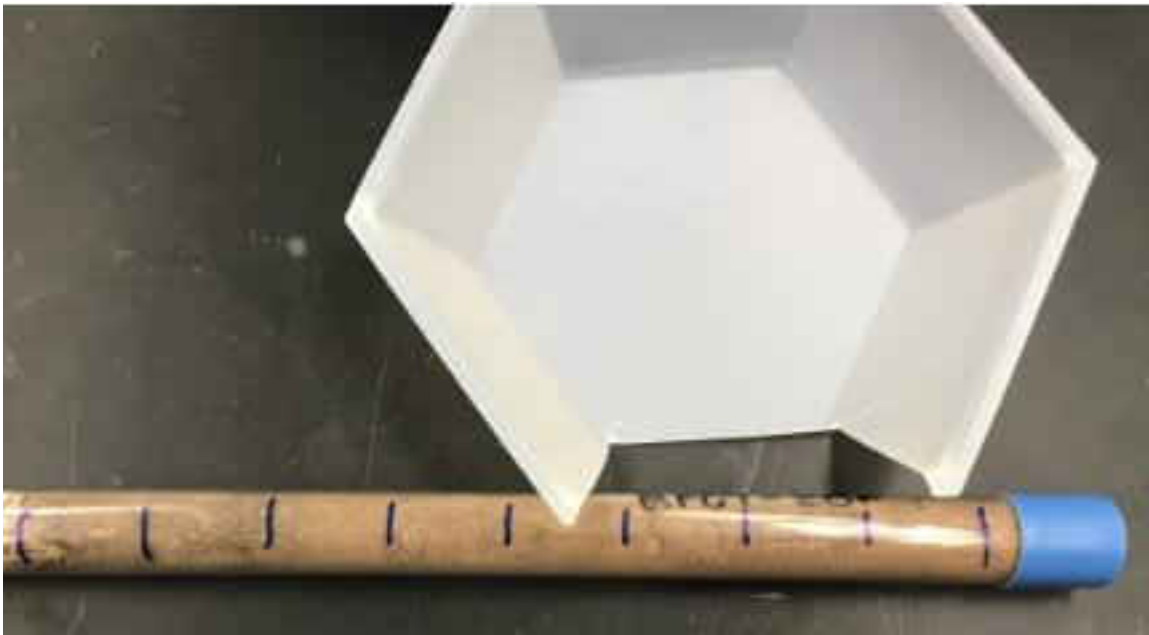
Figure 18. Photograph of improved Soil Core Marking Method with 1 inch segments pre-marked on tube. Also photographed is a 5" diameter weighing boat modified for core fractionation.

Soil cores were collected by using a stainless steel (SS) soil coring device (Forestry Suppliers, Jackson, MS) with a 1.6 cm inner diameter (i.d.) polycarbonate liner. Cores were collected to a depth of 12 inches where possible, depending on soil hardness. Tissue paper (i.e., Kim-Wipes™) was used in the portion of the tube that did not contain soil as a means to prevent shifting of the soil specimen during transport. As shown in Figure 17, an orange cap was used to denote the top of the soil column and a blue cap to distinguish the bottom of the core. Both ends were sealed with Para-Film™ and stored at room temperature. The core samples were stored in the laboratory horizontally to prevent vertical migration of material in the soil column. Cores were labeled starting with the year sampled followed by the number of the core location with respect to the battlefield. A capital letter (e.g., "A") follows the core location to indicate replicate samples.

2.4.2 Soil Core Sample Fractionation

Soil cores sampled from the battlefield were fractionated in preparation for extraction procedures. A section was cut on one side of a (new) 5″ diameter polystyrene weighing boat (see Figure 18) for each 1.0 inch sub-sample from a given core. The orange (top) cap and blue (bottom) caps of the core were removed while holding the core tube's bottom horizontally over the weigh boat without spilling soil from either end of the tube. Using a rubber stopper affixed to a ~0.5″ diameter wooden rod, the soil core was gently pushed within the tube towards the bottom end until the first 1″ of the core was exposed. The exact length was recorded. Then the

core was sawed (with a (new) plastic knife) until it fractured. The sub-sample was thereby collected in the prepared weigh boat. The procedure was continued until all desired sections of the soil core sample were fractionated.

After the sub-samples of the core were obtained, the 1.0 inch sections were ground with a porcelain mortar and pestle. Any objects that could not be ground (e.g., stone, metal, etc.) were collected and separated; all biological matter (e.g., grass, roots, etc.) was discarded. Using a clean Kim-Wipe™, remaining soil material from the mortar and pestle was brushed into the weighing boat for the particular sub-sample. In between each use of the mortar and pestle, both were washed using hot soapy (Citrinox) water and a stiff brush, rinsed with tap water, and had ~10 g of Aldrich (i.e., "clean") sand ground in it as an abrasive. The sand was disposed of, and both mortar and pestle were rinsed with generous amounts of 18.2 MΩ-cm water, rinsing away any remaining sand. Finally, both were dried completely with fresh Kim-Wipes™. It should also be noted that the National Park Service (NPS) specifically required the return of any human remains; fortunately, none were found. The sub-sample contained in the weigh boat was then be poured into a labeled polyethylene Zip-Loc™ bag and sealed tightly. Each bag was labeled with the initials for Brawner Farm (BF), followed by the year sampled, the sampling core location, and the date of fractionation into sub-samples. An example is as follows:

BF07-5A 3-4″ 21-MAR-08

33

This core was obtained at Brawner Farm in 2007 at site #5. It was the first replicate sample that was collected, and the material between 3.0 and 4.0 inches (±0.25 inches) was fractionated on March 21, 2008.

2.5 Extraction Methods

2.5.1 Sequential Extraction

2.5.1.1 *Sequential Extraction - Modern BCR Method: Microwave Assisted Extraction (MAE)*

Fractionated sub-samples were subjected to a modified Sequential Extraction procedure, as promulgated by the Standards, Measurements and Testing Program of the European Union (EU) (formerly named the Community Bureau of Reference of the European Commission BCR). The key idea behind the Sequential Extraction approach is chemical extractants of various strengths are sequentially applied to a given sample, with each successive treatment dissolving different components to release metals. Thus, a series of operationally defined fractions can be obtained.[52]

The speciation of Hg in soil was determined by a MAE method. This method is a modified Sequential Extraction procedure, originally developed by the Standards, Measurements and Testing Program of the EU. The basic theory of Sequential Extraction is the same, but employs microwave energy and a shorter extraction time (40 min), rather than much longer times in a rotary shaker (8 hr). BCR extractions were performed by Garrett Finn under the supervision of Dr. J. Aldstadt.

2.5.2.1 Sample Preparation MAE

For each core, the pulverized soil sub-samples were placed into a labeled weigh boat, then 0.5000 ± 0.001 g was weighed for each fraction, recorded, and transferred to a labeled HP500 MAE vessel. Any remaining sample was returned to the respective ZipLoc™ bag. A blank (uncontaminated sand sample, Sigma Aldrich) was prepared and exposed through each step in the BCR method.

2.5.2.2 BCR Step One: The Mobile Fraction MAE

The first-extract, 20.0 ± 0.5 mL of 0.010 M calcium chloride extraction solution (prepared as described in Section 2.3.2.1) was added to 0.5000 ± 0.001 g of soil in the HP500 MAE vessel. All vessels were capped, placed in a carousel, and the top bolt was tightened snugly (~3/4 turn) with a crescent wrench. The safety vent film was inspected so that it was properly seated in the vent cap and in good condition (14 total vessels, 1 control, 13 additional). Note: If any vessels were unused, 20.0 mL of extraction solution were placed in the vessel. Next, the temperature probe was attached and the carousel was placed in the microwave (caution was used when tightening top nut, as overtightening could damage the probe). The pressure probe was then attached to the control vessel (proper position of the pressure probe is vital to ensure that the pressure sensor does not get tangled with the temperature probe during extraction). For safety, the exhaust hose was placed in the adjacent fume hood. The microwave settings are shown in Table 4 (same microwave settings for all three fractions). After MAE was complete, ~20 min were allowed for vessels and

contents to cool. When all extractions for the day were completed, temperature and

pressure probes were removed and placed in their respective containers.

Watts	Power	Ramp Time to 110^{0}C	Hold
1200	100%	10 min	10 min

Table 4. Microwave settings for BCR extraction.

The contents were then quantitatively transferred to a labeled 50 mL Falcon

tube, and 5.0 mL of 18.2 MΩ-cm water were used to ensure quantitative transfer (the

same 50 mL centrifuge tubes were kept for each sub-sample fraction throughout the

procedure). The centrifuge tubes were centrifuged at 3000 g for 20 min, and

supernatant was decanted into a labeled 125 mL PE bottle. The resulting pellets were

washed with 5.0 mL 18.2 MΩ-cm water, and the centrifuge tubes were inverted ~10x

followed by vortexing for ~1 min to achieve good dissolution. The 50 mL tubes were

centrifuged again at 3000 g for 20 min, and the supernatant decanted to the previous

extract, which was stored until analysis. The remaining soil pellets in the Falcon tube

were saved for subsequent BCR steps.

Note: hereafter the term "work-up" will be used to describe the MAE

preparation, extraction, centrifugation, supernatant isolation, and washing steps

described above.

2.5.2.3 BCR Step Two: Carbonate-bound Fraction by MAE

To the same 50 mL Falcon tube containing the soil pellet from step one of the BCR, a total of 20.0 ± 0.5 mL of the 0.11 M acetic acid extraction solution (prepared as described in Section 2.3.2.2) were added to quantitatively transfer the pellet back into HP500 MAE vessel, and the sample was "worked-up".

2.5.2.4 BCR Step Three: Metal Oxides-bound Fraction by MAE

To the same 50 mL Falcon tube containing the soil pellet from step one of the BCR, a total of 20.0 ± 0.5 mL of the 0.50 M Hydroxylamine Hydrochloride extraction solution (prepared as described in Section 2.3.2.3) were added to quantitatively transfer the pellet back into HP500 MAE vessel, and the sample was "worked-up".

2.5.3.1 ICP-MS Determination

Unless otherwise stated, all ICP-MS protocols were identical to those employed for the industrial effluent analysis. Samples and standards were prepared in 1% (v/v) HNO_3, 1.0 ppm Au, and 50 ppb In within 12 hr of analysis. Sample aliquots were taken directly from labeled HDPE bottles and diluted 1:20 (v/v) in plastic 10 mL volumetric flasks. Hg standards were between 1 to 100 ppb. Hg concentrations in extracts of samples and standards were determined by Shimadzu ICP-MS 20-30 for M/Z values between 50 and 238. All measurements were made in triplicate, and six samples of blank were taken to determine the limit of detection.

Chapter 3 Results and Discussion

3.1 Overview

This chapter is divided into two parts. The first part (Sections 2 to 7) describes studies to develop a new method based upon SIA spectrophotometry for industrial process monitoring. The second part (Sections 8 to 10) is a study of the speciation and transport of heavy metals in soil on a Civil War battlefield.

3.2 Preparation of SIA Prototype Monitor for Field Testing

This work sought to optimize the "initial rate" method (described in Chapter One) and address potential issues which would prevent the repeatable, accurate, and real-time determination of metal cations in industrial effluent by the SIA process monitor. Therefore, an approach using absorbance data taken from 50-100 s was created to develop this "initial rate" model of measurement. As shown in previous work, both ionic strength and solution pH affect the dye films' ability to be used as a chemosensor for metal cations in solution.[50] Therefore, these two factors were among the first to be studied when characterizing the authentic industrial effluent samples. In the present work, additional factors (time frame chosen for the initial rate method and matrix effects) were examined, and the elemental makeup of the industrial effluent samples was characterized.

3.3 Ionic Strength Study

Previously, ionic strength was shown to be a factor in the dye film's rate of binding with analyte. The initial binding rate decreases with added electrolyte, because the non-analyte ions compete for binding. Figure 19 illustrates previous work on the effect of ionic strength on binding. The maximum initial rate was observed at an ionic strength of approximately 200 μM.
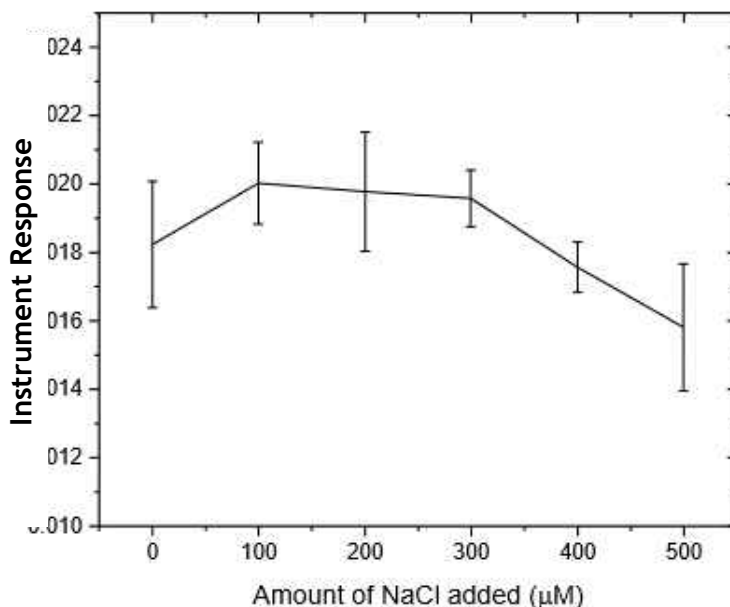
Figure 19. Dye film response vs ionic strength. Effect of ionic strength on binding rate on an Anionic PAR dye film. Error bars represent the 95% confidence interval. (n=4) Adapted from Reference 50.

Therefore, the ionic strength of the industrial samples was investigated to determine an optimal site for testing a prototype SIA process monitor system in the field. Study of the ionic strength of authentic industrial effluents was accomplished by establishing a calibration curve with varying concentrations of NaCl in 18.2 MΩ cm^{-1}

water and measuring 1:100 dilutions of the industrial samples. Between readings, 18.2 MΩ cm^{-1} water was flushed though the instrument until a return to baseline was achieved (i.e., the same response was observed as when the initial 18.2 MΩ cm^{-1} water was introduced). Because the conductivity instrument only gave readings on a numeric LED display, all readings were manually recorded. The Standard Error of the Estimate (SEE) was 1.12 response units, therefore, 95% of data should fall within 2.24 response units of the trendline. The SEE was also small compared to the lowest instrument reading (9.60 units). Additionally, the resulting calibration model was as expected, with ionic strength increasing linearly with increasing concentrations of the 1:1 electrolyte. The ionic strength of the diluted industrial samples fell within the calibration curve (Figures 20 and 21 and Table 5).
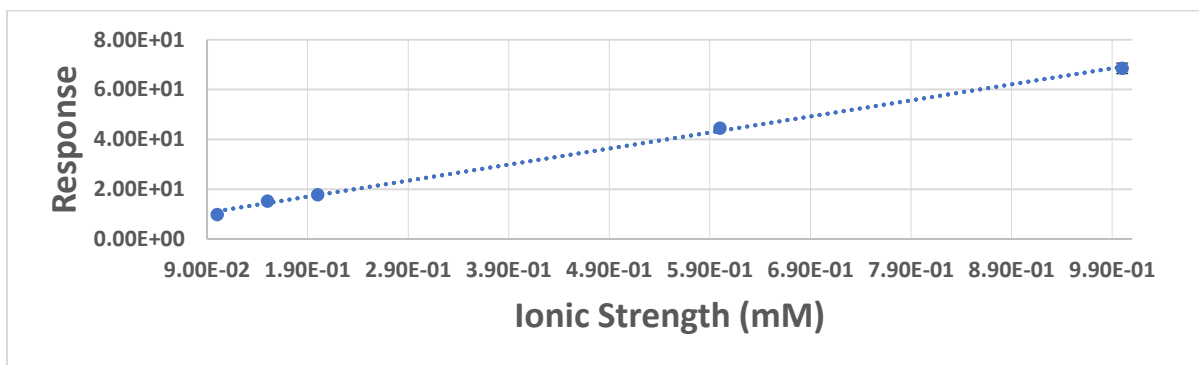
Figure 20. Conductivity calibration model. Error bars represent the Student's t value at the 95% confidence interval (n=3).

Linear Regression model: Slope = 6.45 x 10^1 Response units x Ionic Strength^{-1} Intercept = 4.73 Response units

Concentration NaCl	Average Response	s	RSD	95% (n=3)
0.10 mM	9.76E+00	1.14E-01	1.17E+00	1.42E-01
0.15 mM	1.53E+01	8.37E-02	5.49E-01	8.78E-02
0.20 mM	1.78E+01	1.38E-01	7.77E-01	1.45E-01
0.60 mM	4.45E+01	7.43E-01	1.67E+00	9.23E-01
1.0 mM	6.85E+01	1.34E+00	1.95E+00	2.13E+00

Table 5. Data set used to create calibration model in Figure 20.
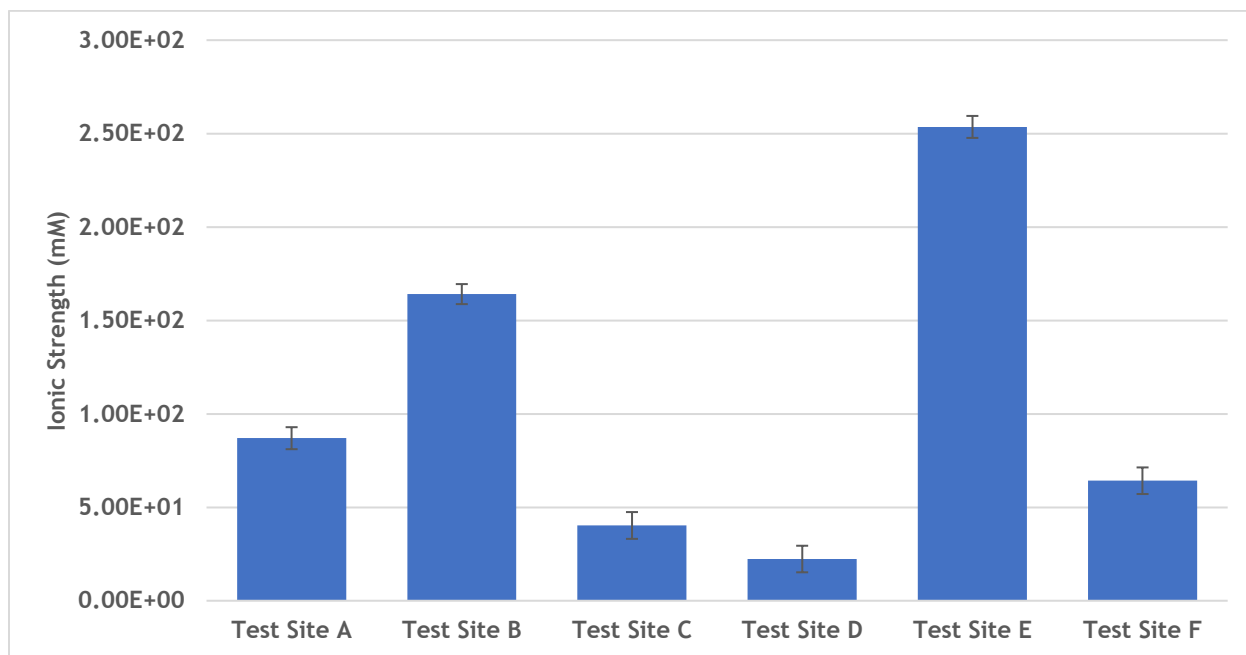
Figure 21. Ionic Strength of Industrial samples. Error bars represent the Student's t value at the 95% confidence interval (n=3).

The ionic strength of the industrial samples greatly exceeded the optimal ionic strength that was previously studied for the prototype monitor (<500 mM).[50]
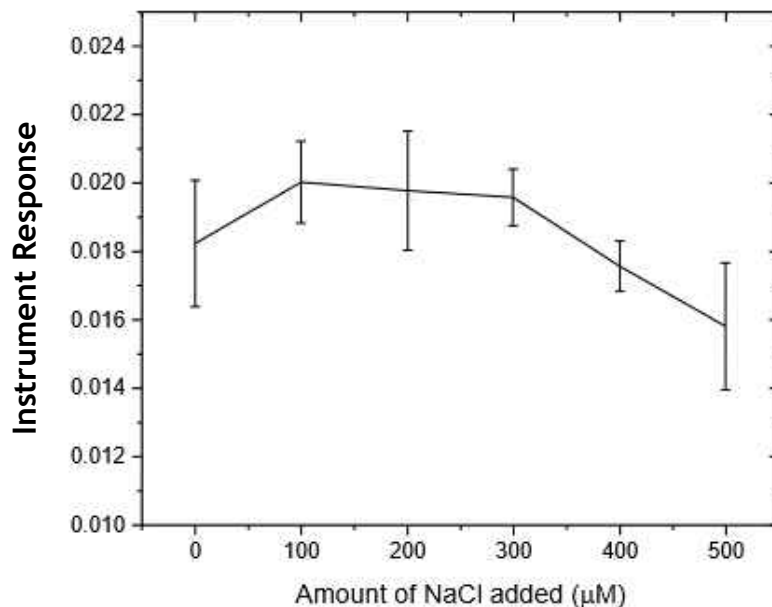
Figure 22. Effect of ionic strength on binding rate (n=4). The maximum initial rate was observed at an ionic strength of approximately 200 μM. Adapted from Reference 50.

Therefore, it would be necessary to match the ionic strength of the expected process samples if one establishes a calibration model prior to measurement of the industrial samples. Alternatively, while increasing cost, reagent use, measurement time, and complexity, a method of standard additions approach would greatly increase accuracy, because it takes into account matrix effects that include ionic strength.

3.4 pH Study

Chemosensor dyes under study were based upon 1-(2-Pyridylazo)-2-naphthol (PAN), and thus would be expected to have similar pK_a values (molecule and species distribution shown in Figure 23). A MOPS buffer was used in all samples / standards to

maintain a pH of 7.2. This pH was selected for binding solutions, because the mono-

protonated forms are required for binding, and they dominate at that pH.

Figure 23. Part (A) PAN. Part (B) shows expected species distribution based on pKa values.

PAN

$pK_1 = 2.8$ and $pK_2 = 11.6$
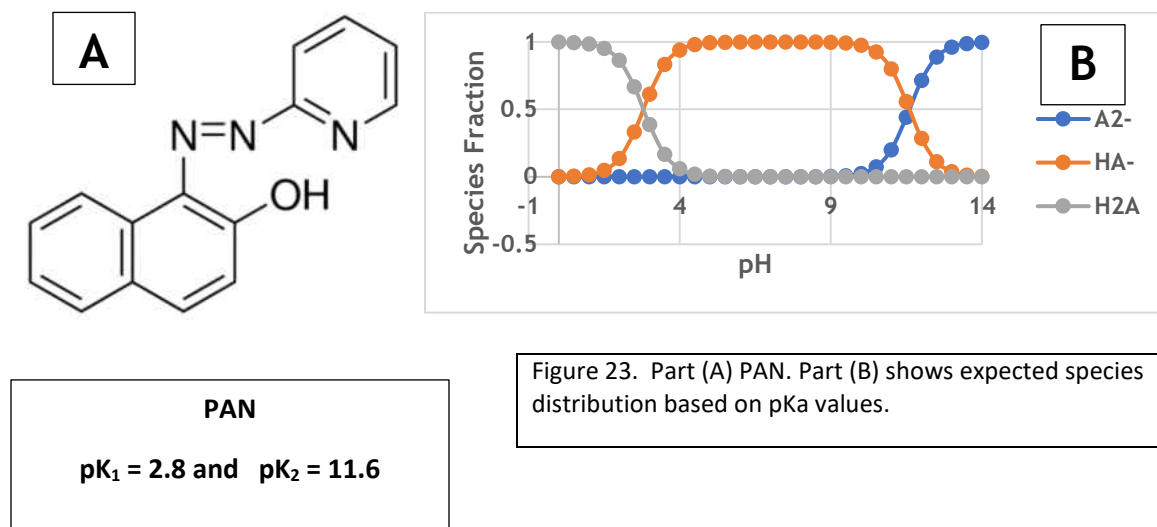
The pH of the sample has a major impact on the ability of the dye film to bind

metals, and is shown in Figure 24.
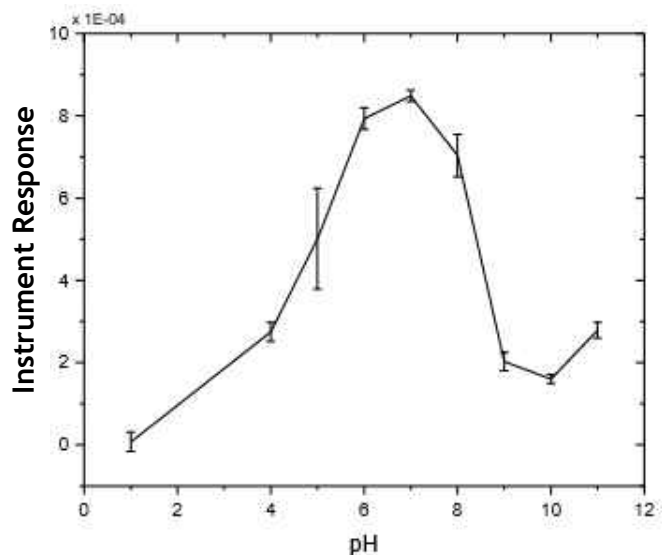
Figure 24. Dye film response vs pH. It was previously verified that neutral pH conditions were optimal for metal binding to anionic PAR dye film. Error bars represent the 95% confidence interval. (n=4) Adapted from Reference 50.

At low pH, the OH group and NH$^+$ group (both ortho to the N=N) are protonated, and do not allow for metal cation binding. Under more basic conditions, both become de-protonated, and the N=N bond breaks with the protonation of one of the N atoms involved in the double bond. Now, there are three negatively charged groups which coordinate and form a complex with a metal cation (dashed lines in figure 25). Chemosensor dyes were designed so that decreasing the film's pH would re-protonate the key groups and release bound metal, thereby regenerating the film. While giving an overall increase of practicality to the instrument, this approach does necessitate that samples / standards are buffered to maintain a constant pH during absorbance measurements.
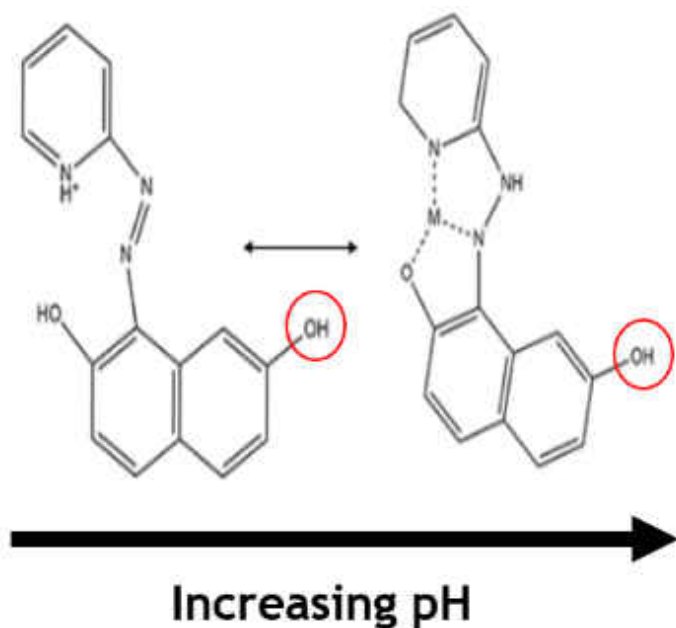
Figure 25. Reversibility of metal binding. The oxygen in circled OH group is used to covalently bind the chemosensor to the glass slide, and therefore will not de-protonate with increasing pH.

As described above, the pH of the sample has a major impact on the ability of the dye film to bind metals. The pH of all industrial samples was measured to ensure proper amounts of buffer were used to keep sample pH constant. The most common treatment method for industrial effluent is adjusting pH (by addition of NaOH) to a point where the heavy metals form hydroxides and precipitate. Therefore, having basic pH values for all samples was expected, and found to be the case in all except the samples from Test Site F as shown in Figure 26.
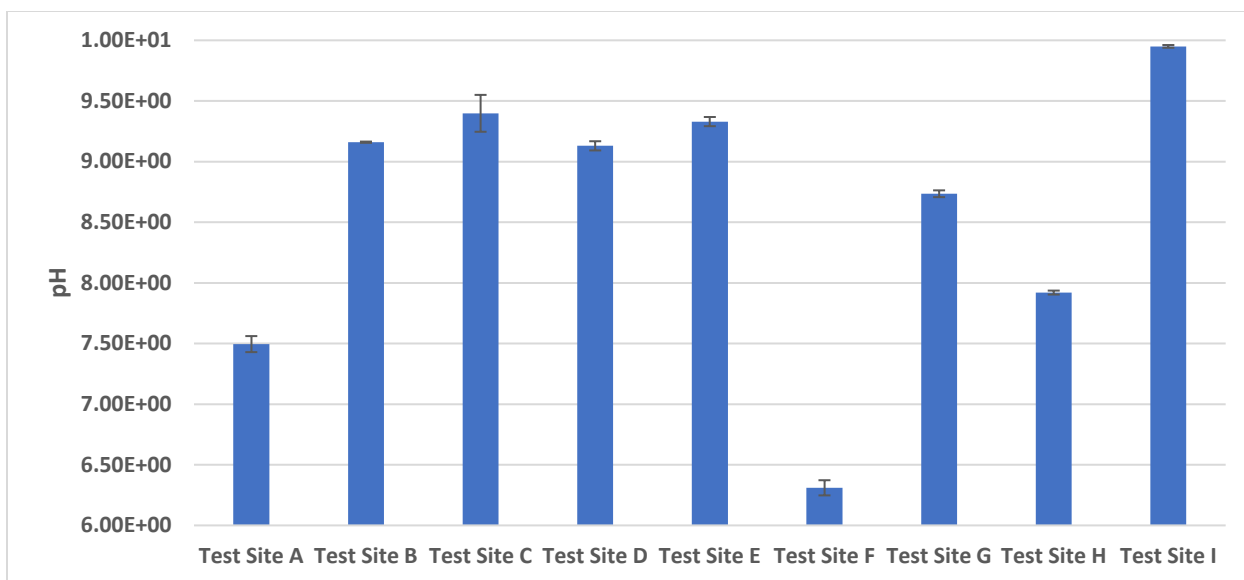
Figure 26. Raw Sample pH (measured directly via pH probe). Error bars represent the Student's t value at the 95% confidence interval (n=3).

3.5 Experimental Overview

Figure 27 is a diagram of the FC, which interfaces D to the flow system. The absorption of analyte causes a color change in the dye film, which is optically monitored by molecular absorption using a Tungsten halogen (WX) lamp and Charge Coupled Device (CCD), which are connected to the FC with optical fibers.
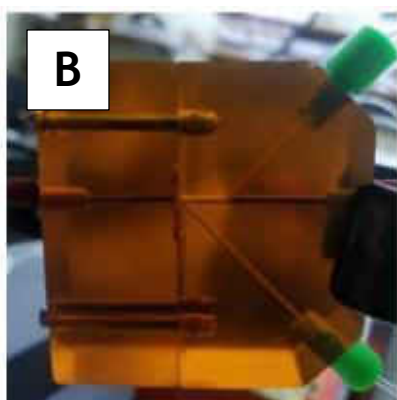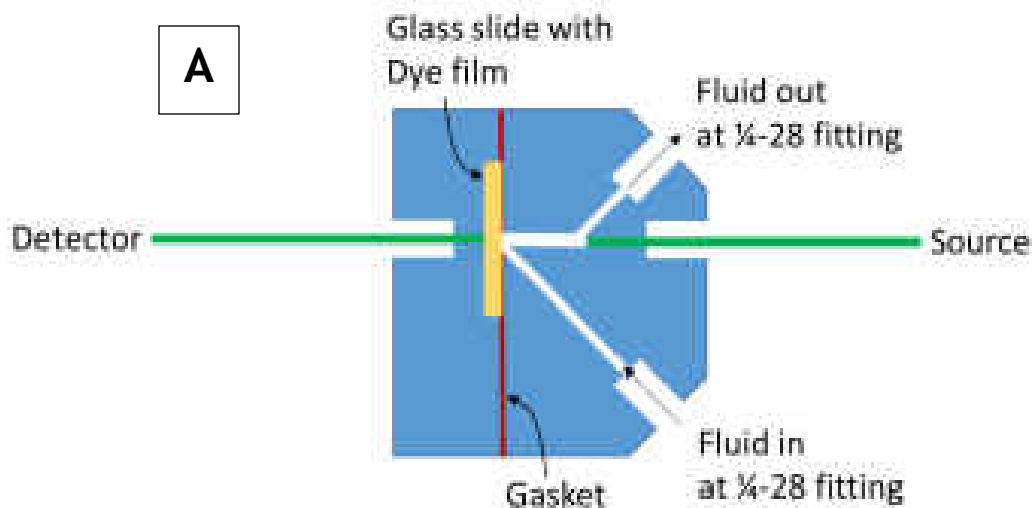
Figure 27. Schematic diagram of the FC. A chemosensor dye film is adhered to one side of the glass slide (facing the right side of part A, i.e., towards the light source) which will selectively adsorb analytes. The optical fibers are shown in green.[50]

The SIA method is based upon the manipulation of three separate zones of reagents, as shown in Figure 28. In this procedure, the MPV first moves into position 1 to aspirate 1.5 mL of the buffer reagent into the HC. Next, the port changes position to 3 to aspirate 0.5 mL of acid into the HC. The port then changes position to 4 to aspirate 2.0 mL of the sample into the HC. Thus at the conclusion of the first three steps, the three zones are "stacked" in the HC. For the measurement step, the

port changes position to 5 to connect the HC to the FC. The stacked zones are then dispensed to the FC for the absorption measurement. Three loaded solutions are pumped through and past the dye film. It is interesting to note that while the 100 ppb Zn sample is the last solution to be loaded, it is the first to flow past the dye film, and solutions must be loaded in "reverse" order, because the system pumps in opposite directions for aspiration and dispensing samples.

Sample aspiration away from the detector.

1500 μL 0.05 M MOPS buffer (pH 7.2), 300 ppm NaCl, 2mM Triton-X 100 Surfactant	500 μL 0.1 M HCl, 2 mM Triton-X 100 Surfactant	2000 μL 100 ppb Zn 0.05 M MOPS (pH 7.2), 300 ppm NaCl, 2 mM Triton-X 100 Surfactant

Sample delivery towards detector.
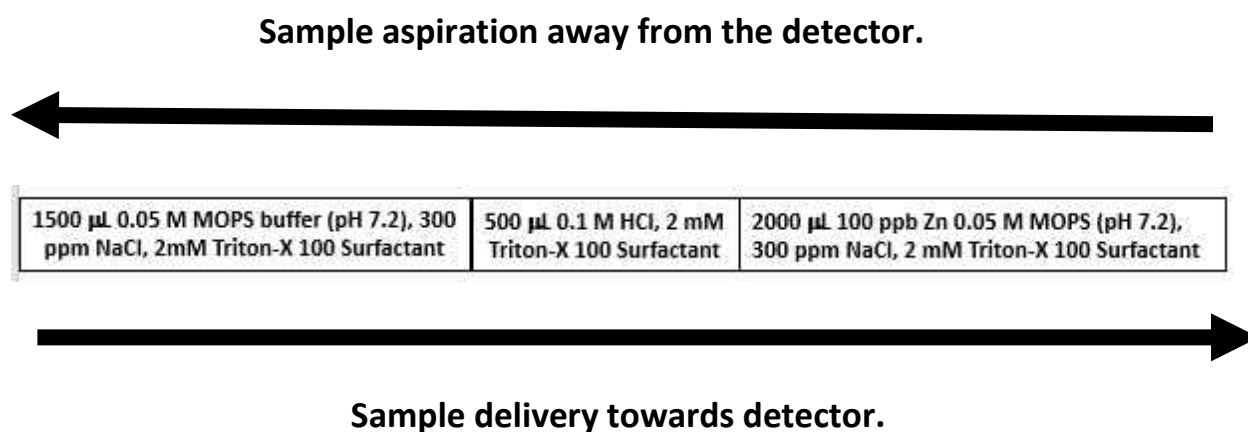
Figure 28. The experimental procedure used in the SIA method. The flow rate was 12 μL/s, to produce a sample throughput of 5 samples/hr.

While the various samples / reagents flowed past the dye film, the absorbance was monitored at 525 nm to measure changes in the dye film's bound vs unbound state. Several industrial effluent samples were studied for factors that would influence analyte binding including ionic strength; pH; and presence of interfering elements. Reagent water with a resistivity of 18.2 MΩ cm^{-1} was used for all experiments.

Initially, quantification of Zn was measured by the maximum absorbance that the dye film reached at a fixed wavelength.[50] However, two problems arose from this

approach. First, plotting the maximum absorbance reached vs concentration did not result in a linear model. Second, using only one data point for determination makes an erroneous measurement (for example, a stubborn air bubble) much more impactful than using multiple measurements. Therefore, this maximum absorbance model was abandoned for an initial rate model. In the initial rate model, the time period was chosen (typically 50 to 100 s, resulting in 100 data points) where the absorbance was measured. During this time interval, absorbance would increase, because of Zn binding to the chemosensor dye. The slope of these absorbances vs time was used for the instrument response, resulting in units of sec^{-1}.

Figure 29 contains SIA instrument data for a Zn standard. Note several key time intervals. (A) Initial time necessary for sample to reach dye film. (B) Initial increase in absorbance, while Zn binds to dye film (the spike at the beginning of time interval B is the result of an air bubble passing through the system). (C) Zn binds to the dye film, therefore, there are fewer available places where binding can occur. This causes the binding rate to decrease, which is indicated by the slower increase in absorbance. (D) Eventually, the dye film becomes "loaded" and no more binding can occur, and the absorbance vs time graph levels off. (E) To regenerate dye film for subsequent experiments, 0.1 M HCl is pumped through to protonate the dye film, and un-bind any bound ions. (F) MOPS buffer is pumped through to re-establish starting protonation state at pH of 7.2, and prepare dye film for subsequent runs.
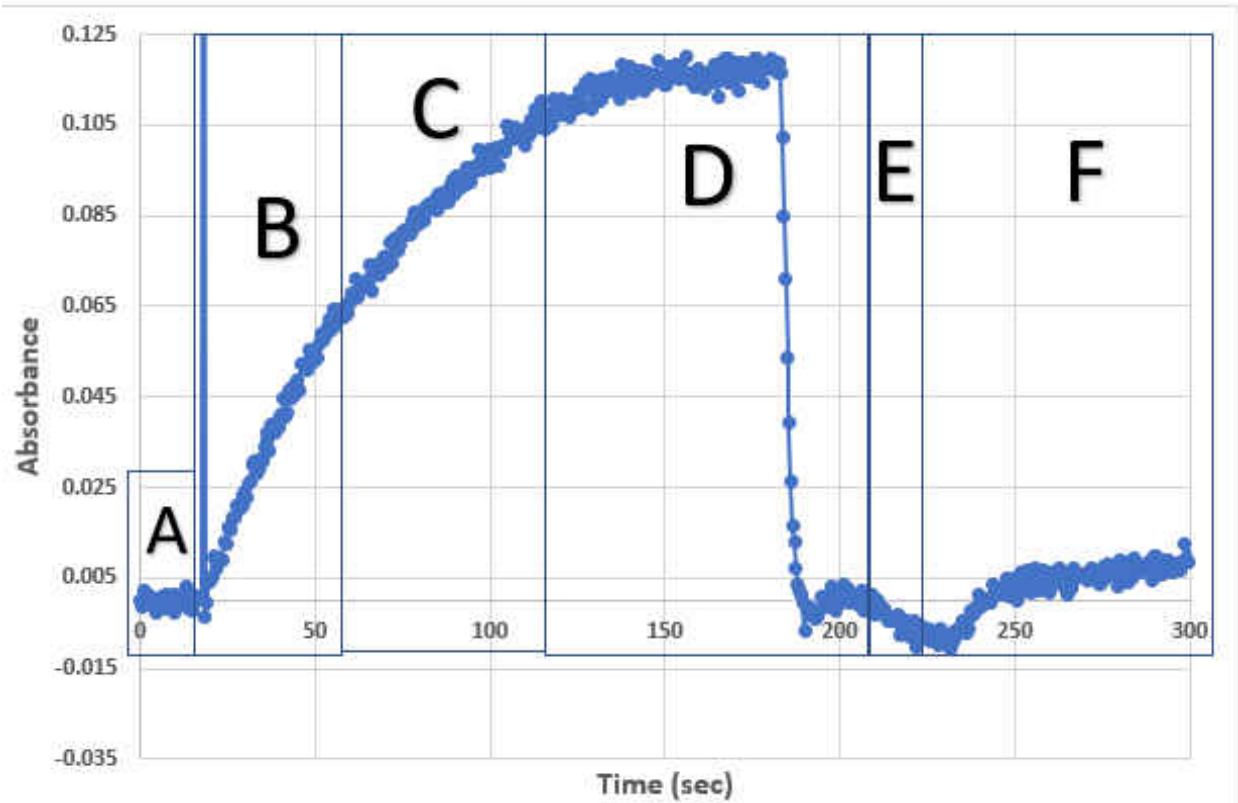
Figure 29. A vs T plot for 4.90 ppm Zn with detector set to record at 525 nm.

3.6 Study of Initial Rates for Calibration Models

Figure 30 shows the response for a 1000 ppb Zn standard. Part A consists of data collected from 0 to 300 s. Part B contains only the 50 to 100 s region used for quantification. Using the data in part B, a trendline was created in which the slope was used for quantification of Zn.

50
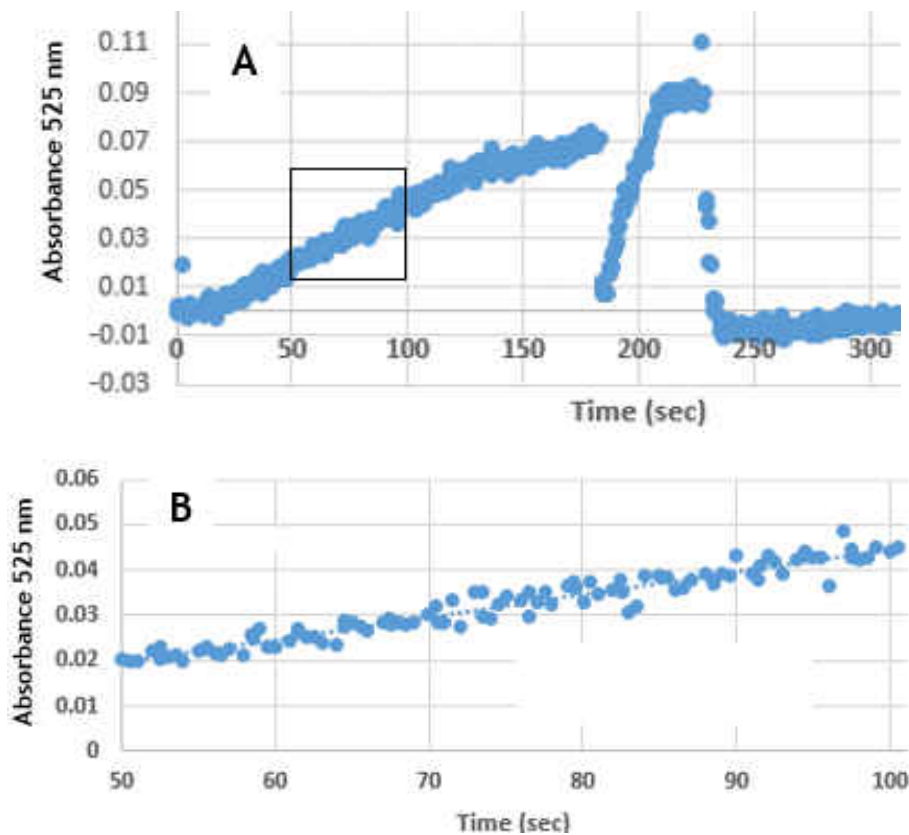
Figure 30. (A) Absorbance measurement Zn standard. Boxed region was used for quantification and shown in greater detail in part (B). (B) Absorbance data between 50 and 100 s. Slope= 5.02×10^{-4} sec^{-1} Intercept= -5.46×10^{-3} SEE= 1.93×10^{-3}

An additional benefit of the initial rate model was that it extends the dynamic range. At a relatively high concentration of Zn, the dye will have all binding sites occupied and is therefore unable to bind more Zn. However, even after this maximum absorbance level was reached, increasing the concentration of Zn will still increase the binding rate, allowing for higher levels of Zn to be quantified.

Figure 31 shows the response for four Zn standards. Initial rates were then used to create a calibration model as shown in Figure 32.
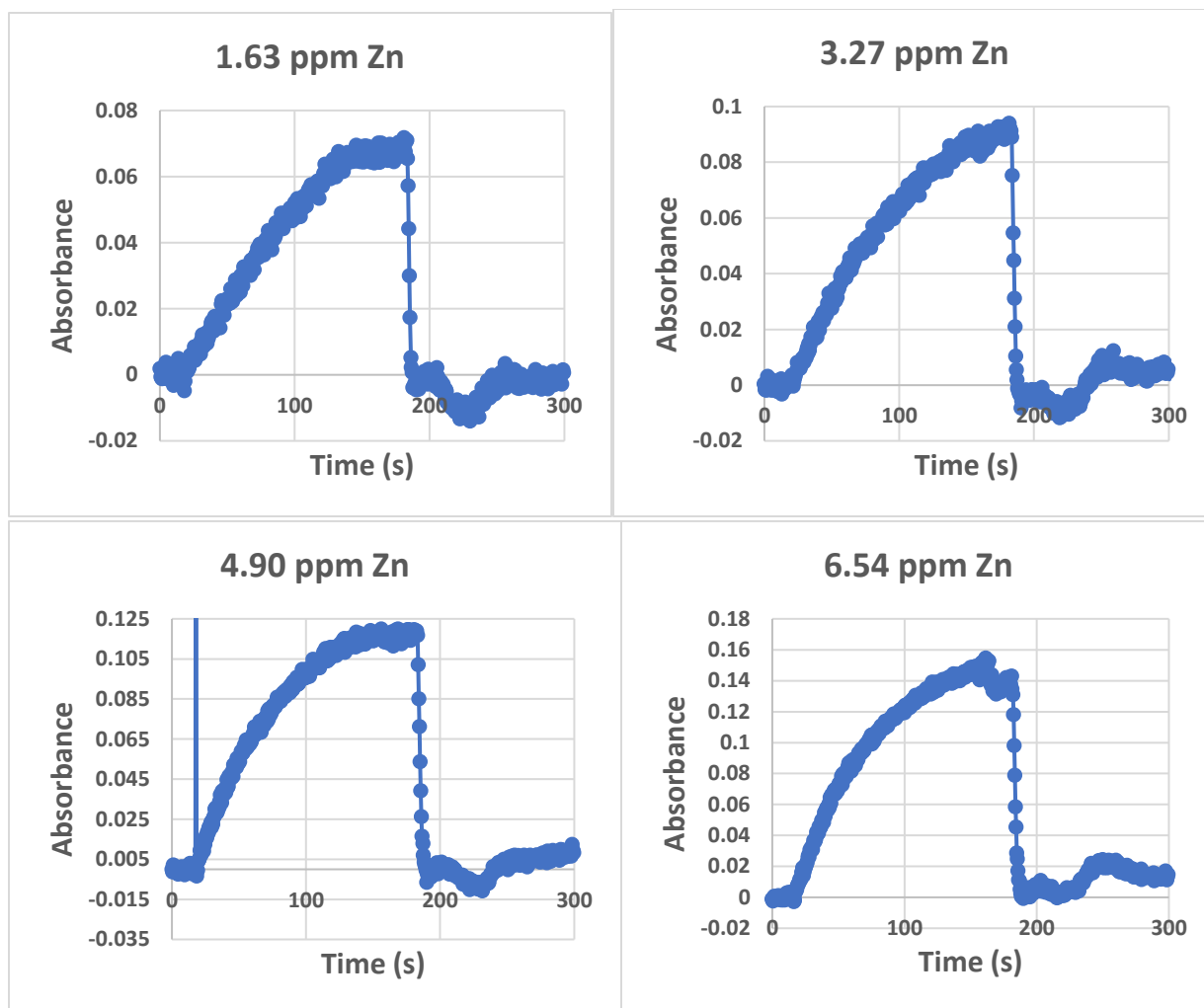
Figure 31. Dye film responses to various concentrations of Zn. Absorbance recorded at 525 nm, and all four experiments performed on the same dye film (TMH-4-034).

As expected, the initial rates increase linearly with Zn for the concentration range in Figure 35. This model was able to differentiate between 1.63 ppm and 4.90 ppm Zn, or between 3.27 ppm and 6.54 ppm Zn. Because of overlapping error bars, it was unable to distinguish between 1.63 ppm and 3.27 ppm Zn or between 4.90 ppm and 6.54 ppm Zn, therefore these data sets were not statistically different. A two-sample t-test was performed for all concentrations, shown in Table 6. Since all test

statistics are greater than the Student's t critical value at the 95% confidence level

with four degrees of freedom (2.776), all concentrations are statistically different,

despite overlapping error bars.

Higher ppm standard	Lower ppm standard	t
6.54	4.90	4.81
6.54	3.27	13.6
6.54	1.63	12.1
4.90	3.27	7.17
4.90	1.63	8.70
3.27	1.63	4.72

Table 6. Test statistics for Zn standards in Figure 32 and Table 7.

However, it was unclear why the Student's t value 95% confidence intervals

were so large. Across all concentrations measured, the second and third trials were

always in better agreement with each other than with the first trial (see Table 7). In

future use, accuracy may be improved by increasing the number of trials from three

to four, while omitting the first trial's data, since the film was in the process of

conditioning.
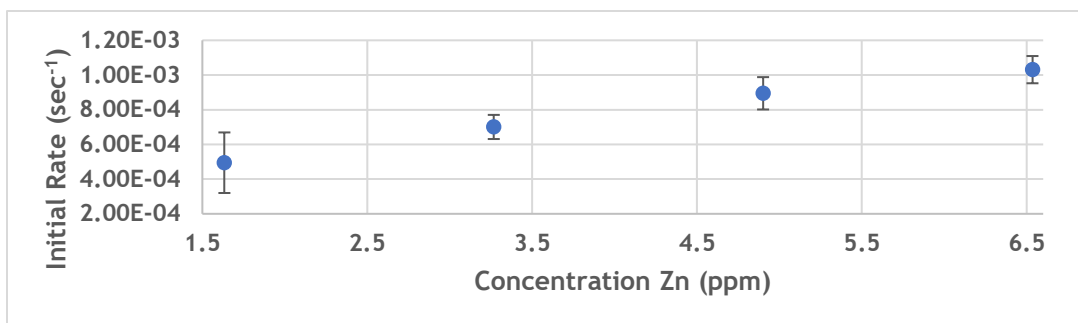
Figure 32. Zn Calibration Model plotted using dye film TMH-4-034. Error Bars represent the Student's t value at the 95% confidence interval (n=3).

Linear Regression model:

Slope = 1.10 x 10^{-4} (sec x Zn (ppm))$^{-1}$ Intercept = 3.29 x 10^{-4} sec^{-1} SEE = 4.50 x 10^{-5} sec^{-1}

Table 7 contains the data set used to create the calibration model in Figure 32. In the following tables, Standard Deviation is abbreviated as "s", Relative Standard Deviation is abbreviated as "RSD", and the Student's t value at the 95% confidence interval is abbreviated as "95% (n=3)".

Concentration Zn ppm	Slope	Average	s	RSD	95% (n=3)
1.63	5.75E-04	4.95E-04	7.03E-05	1.42E+01	1.75E-04
1.63	4.44E-04				
1.63	4.65E-04				
3.27	6.75E-04	7.01E-04	2.80E-05	4.00E+00	6.96E-05
3.27	6.97E-04				
3.27	7.30E-04				
4.90	8.54E-04	8.95E-04	3.75E-05	4.20E+00	9.33E-05
4.90	9.27E-04				
4.90	9.03E-04				
6.54	9.95E-04	1.03E-03	3.16E-05	3.06E+00	7.84E-05
6.54	1.05E-03				
.546	1.05E-03				

Table 7. Data obtained from a series of standards to create a calibration model. All standards were buffered to a pH of 7.2 using 100 mM MOPS buffer.

As shown in Figure 33 and Table 8, matrix effects were also studied by spiking standards with low levels (1:100 dilution) of industrial process samples. This allowed the resulting calibration curve to be compared to a previous one obtained with only standard. All samples were run in increasing order of concentration. As the Student's t value 95% confidence intervals follow a trend of becoming larger, it was likely that, even at a 1:100 sample dilution, matrix effects were accumulating in the dye film. For example, a metal that binds more tightly than Zn may be accumulating in the film during the experiments. This interfering metal ion would thus occupy potential binding sites in the film, competing with Zn and lowering the accumulation rate of Zn.
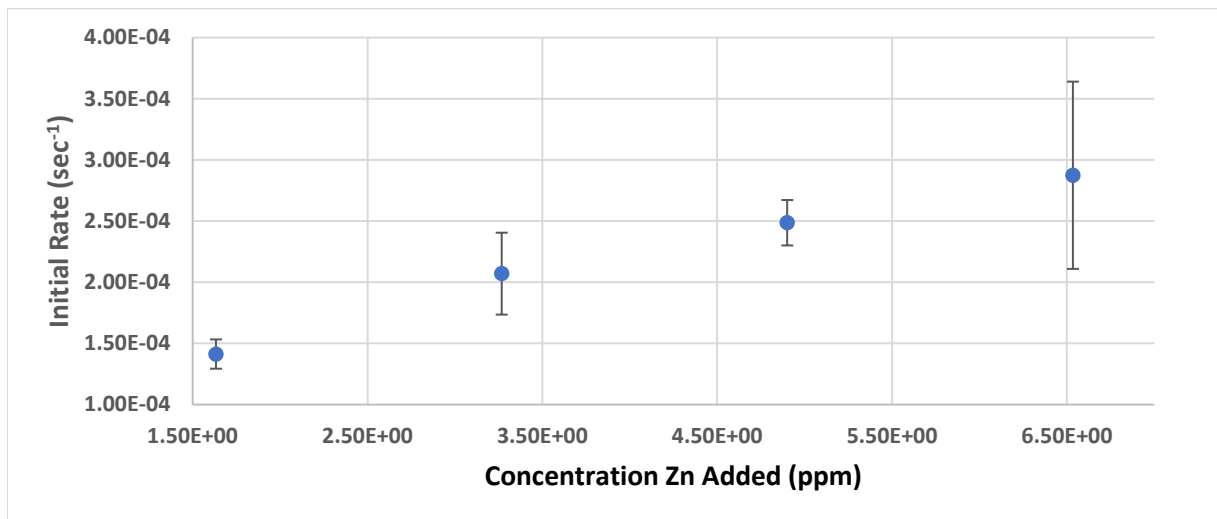
Figure 33. Zn Spiked Sample Calibration Model using dye film TMH-4-034. Error Bars represent the Student's t value at the 95% confidence interval (n=3).

 Linear Regression model:

Slope = 2.94×10^{-5} (sec x added Zn (ppm))$^{-1}$ Intercept = 1.01×10^{-4} sec^{-1} SEE = 1.74×10^{-5} sec^{-1}

Concentration Zn added					
ppm	Slope	Average	s	RSD	95% (n=3)
1.63	1.36E-04	1.41E-04	4.82E-06	3.41E+00	1.20E-05
1.63	1.43E-04				
1.63	1.45E-04				
3.27	2.20E-04	2.07E-04	1.35E-05	6.51E+00	3.35E-05
3.27	1.93E-04				
3.27	2.08E-04				
4.90	2.45E-04	2.49E-04	7.47E-06	3.01E+00	1.86E-05
4.90	2.57E-04				
4.90	2.43E-04				
6.54	3.15E-04	2.87E-04	3.08E-05	1.07E+01	7.65E-05
6.54	2.54E-04				
6.54	2.94E-04				

Table 8. Data set used to create calibration model in Figure 33.

It is unclear why the 4.90 ppm data deviates from the trend of increasing Student's t value 95% confidence intervals.

While most time frames for modeling were from 50 to 100 s in the experiment, other time frames were also investigated. Using an earlier time frame could shorten analysis time and thereby improve throughput. Various time frames in addition to the 50 to 100 s were applied to the same data set to produce several calibration models to compare the advantages or disadvantages of each. Depending on the information needed, a lowered instrument response (sec*ppm)$^{-1}$ can be offset by increased throughput and decreased reagent usage and waste generation by utilizing earlier time frames.

Figure 34 shows that initial rates increase with later time frames. During the 10-20 s time interval, there was little increase in instrument response verses Zn concentrations. While later (and longer) time frame models possess the more slowly increasing data points; the addition of later, more rapidly increasing data points offset the earlier ones, and give an overall increase in instrument response with increasing time frames. Comparing the 10-20 s and 10-30 s intervals is especially noteworthy, as adding 10 s of later data increases the response by a factor of almost 10. Another key comparison is between the 10-60 s and 15-65 s intervals. While both possess the same amount of data, there is a noticeable increase in instrument response by trading 5 s of earlier data points for 5 s of later data points.
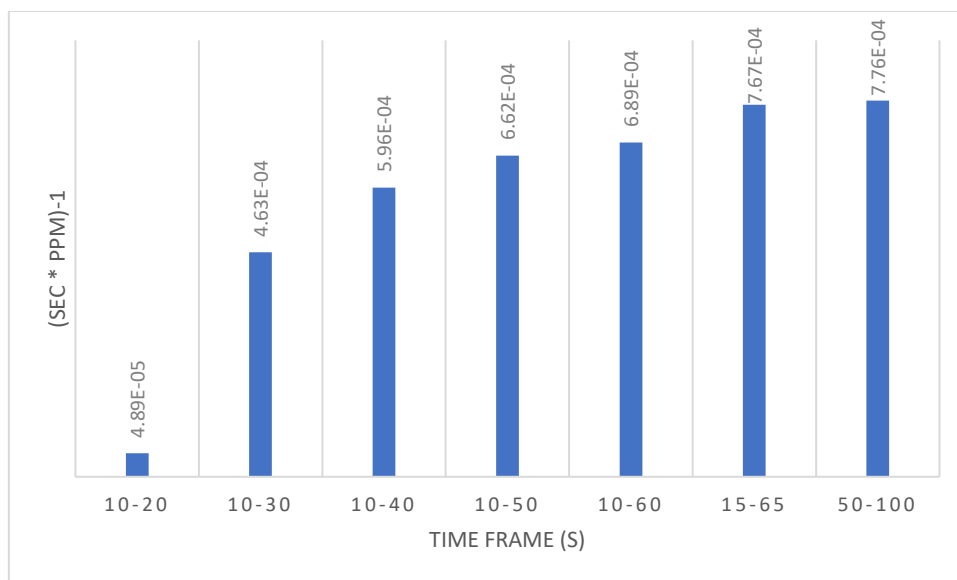
Figure 34. Variation in calibration model slope.

Figure 35 shows the variation in calibration model R^2. Aside from the 10-20 s and the 15-65 s time intervals, there was little variation in calibration model R^2 values. The 10-20 s interval was too soon for determination, as the dye film had not yet stabilized.

Figure 36 shows the variation in intercept. Aside from the 10-20 s and the 15-65 s time intervals, there was little variation in calibration model intercept across time frames. The 10-20 s and 10-65 s time intervals calibration models were also found to possess low R^2 values (0.0982 and 0.723 respectively), showing a low correlation between data and linear fit.
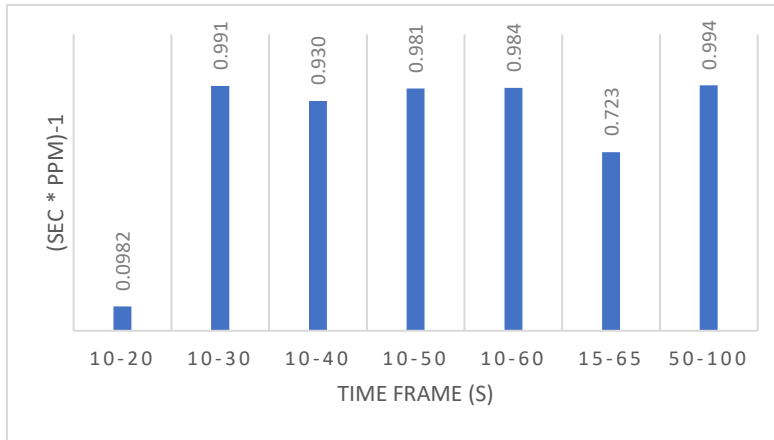
Figure 35. Variation in calibration model R^2. It is unclear why the 15-65 s time interval possesses a much lower R^2 value than the 10-60 s time interval.
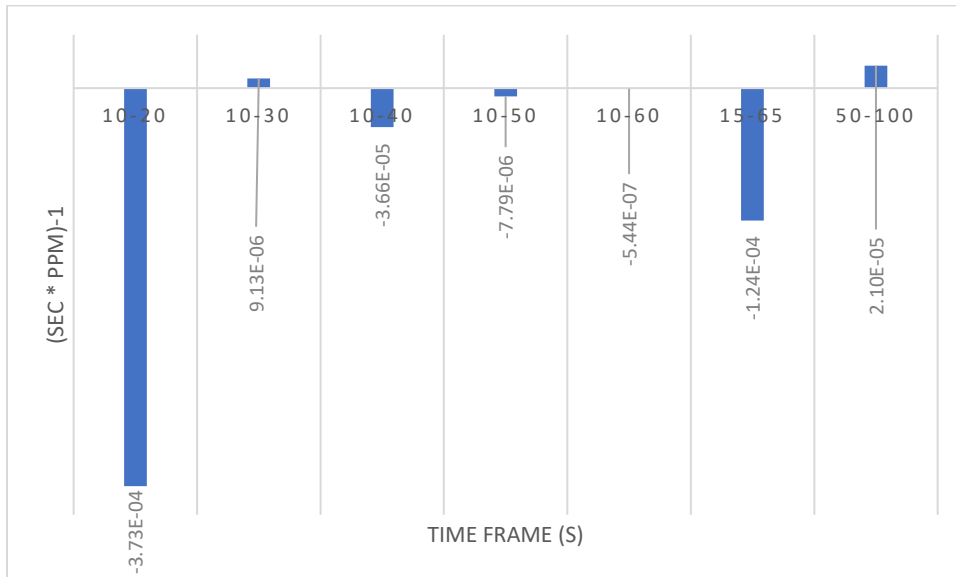
Figure 36. Variation in calibration model intercept. It is unclear why the 15-65 s time interval possess a more significant intercept than the other time intervals.

In comparing the previous three Figures, the two best choices in time are the 10-60 s and 50-100 s time intervals, as they possess the highest instrument responses, while still producing a linear response. Although the 15-65 s interval gave a higher response than the 10-60 s interval, the 15-60 s interval's R^2 value (0.723) makes it a

59

poor choice for a linear model fit; as there was a much lower correlation between the data and linear model produced.

3.7 ICP-MS Elemental Analysis of industrial effluents for SIA Project

The industrial effluent samples were compared as a means to find an optimal testing location for the prototype SIA instrument. To verify Zn concentrations, as well as to identify potential interferents (especially other divalent cations), elemental analysis was performed by ICP-MS. Because the goal was to monitor a single analyte at a time (Zn), the optimal testing location's effluent would ideally have relatively high levels of Zn and little or no interferences for the initial testing of the prototype system.

Figure 37 shows the mass spectrum for one of the industrial effluents. The instrument was calibrated with five Zn standards from 20 to 100 ppb.
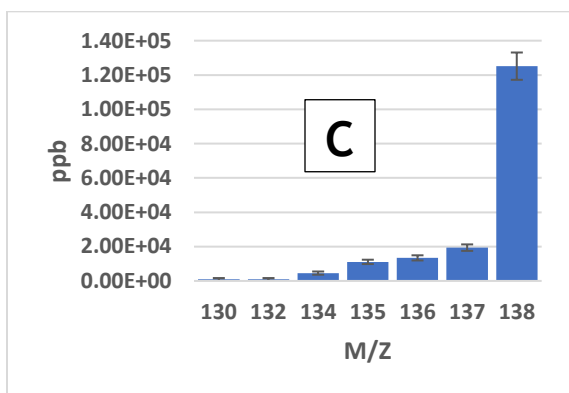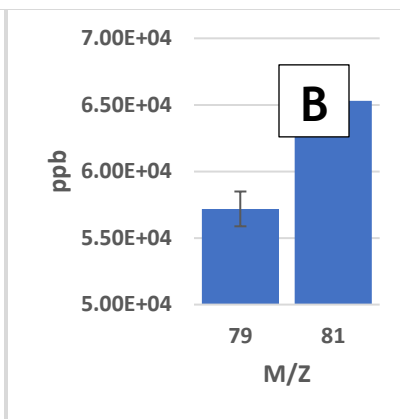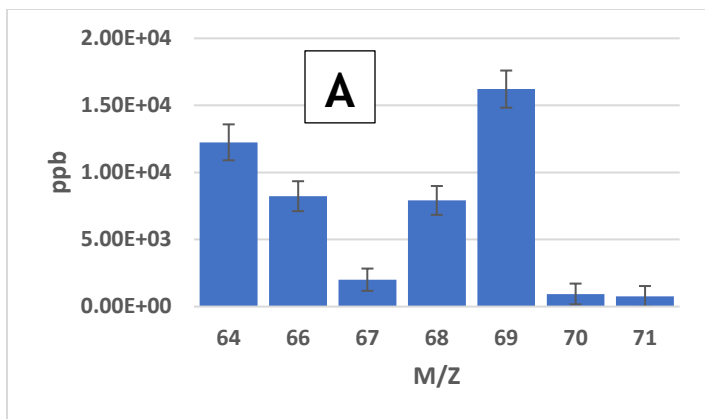
Figure 37. Mass spectrum for an industrial effluent. (A) m/z values for Zn and Ga. (B) m/z values for Br. (C) m/z values for Ba. Error bars represent the Student's t value at the 95% confidence interval (n=3).

m/z	ppb	95% (n=)
64	1.17E+04	1.40E+03
66	7.86E+03	1.16E+03
67	1.92E+03	8.39E+02
68	7.68E+03	1.14E+03
69	1.62E+04	1.61E+03
70	9.28E+02	7.75E+02
71	7.68E+02	7.66E+02
79	4.39E+04	1.96E+03
81	5.02E+04	1.99E+03
130	8.98E+02	7.69E+02
132	9.02E+02	7.70E+02
134	4.72E+03	8.51E+02
135	1.14E+04	1.07E+03
136	1.37E+04	1.09E+03
137	1.99E+04	1.31E+03
138	1.29E+05	4.09E+03

Table 9. Data from above figure. Only values with m/z values corresponding to Zn, Ga, Br, and Ba are presented. The Student's t value at the 95% confidence interval is abbreviated 95% with n=3.

Isotope	%		%		%	
61					Ni	1.140
62					Ni	3.634
63	Cu	69.17				
64			Zn	48.6	Ni	0.926
65	Cu	30.83				
66			Zn	27.9		
67			Zn	4.1		
68			Zn	18.8		
69					Ga	60.108
70	Ge	21.23	Zn	0.6		

Figure 38. When selecting which isotope to use for quantification, relative abundance Tables must be consulted, as isobaric interferences need to be either accounted for, or avoided. Adapted from Reference 53 .
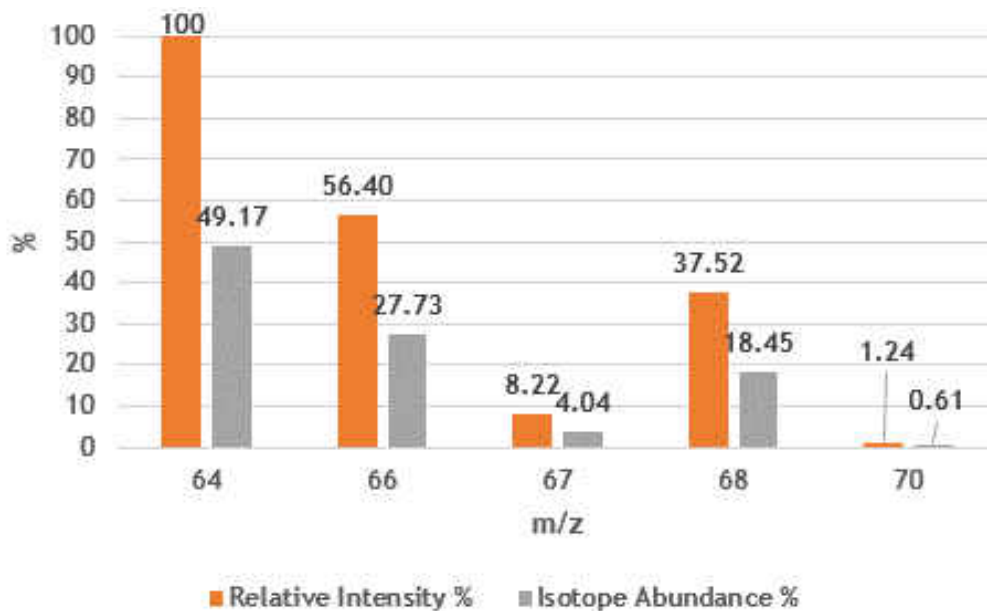
Figure 39. Expected Zn isotope distribution. Fingerprint regions for analytes should be compared to isotope patterns, to approximate extent of matrix effects. Adapted from Reference 54 .
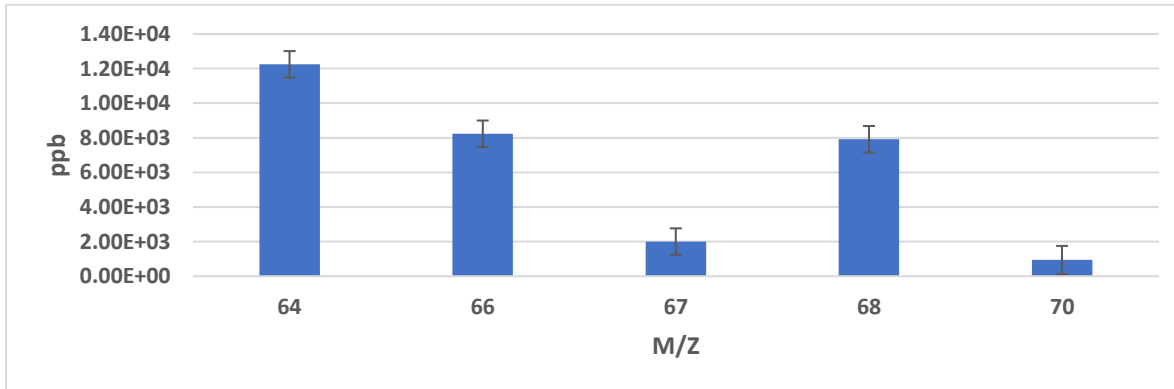
Figure 40. Uncorrected Zn fingerprint from Figure 37. Relative intensities are (from left to right) 100%, 67.2%, 16.4%, 65.6%, and 7.9%. Error Bars represent the Student's t value at the 95% confidence interval (n=3).

While which isotopes are major and which isotopes are minor corresponds with the expected isotopic abundances (see Figure 39), the relative intensities from Figure 39 and Figure 40 do not match precisely. All relative intensities (except the base

peak) will be greater than expected because isobaric interferences and polyatomic interferences are typically present.
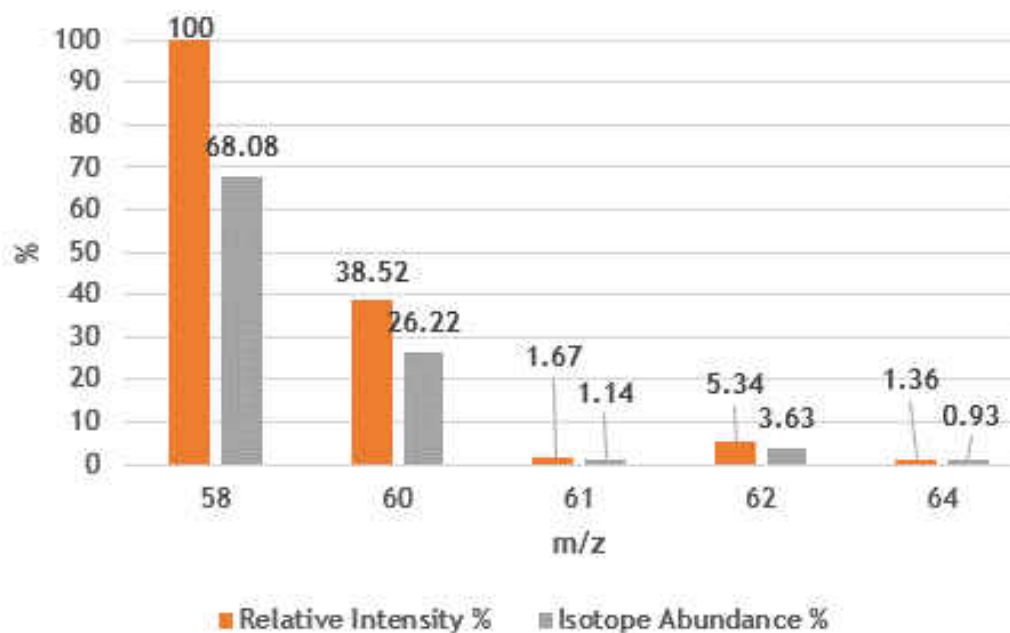
Figure 41. Expected Ni isotope distribution. Ni has a minor isotope overlapping with ^{64}Zn, however, the relative isotopic abundances ^{64}Zn's 49.17% to ^{64}Ni's 0.93% should cause only minor exaggeration. Adapted from Reference 55.
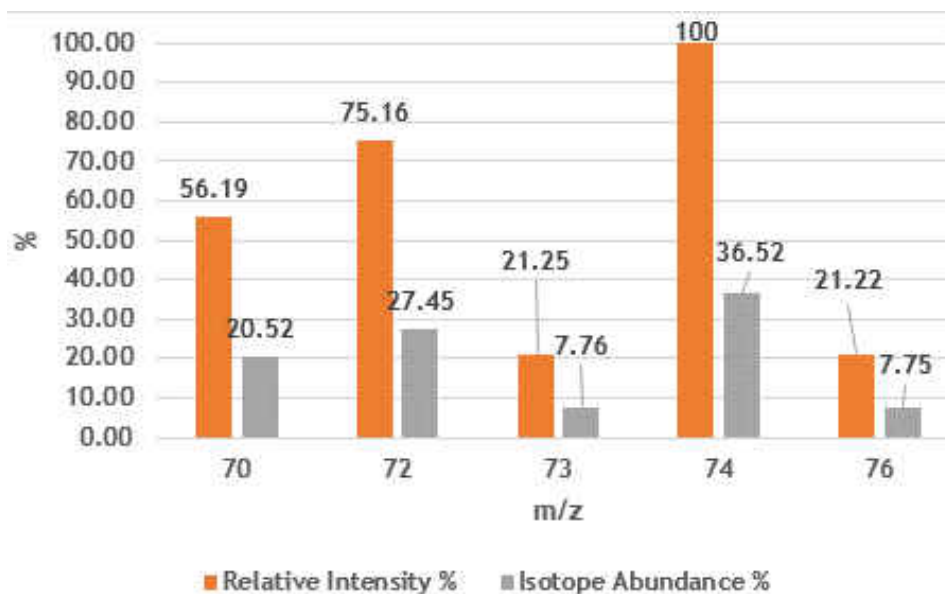
Figure 42. Expected Ge isotope distribution. Ge has an isotope overlapping with ^{70}Zn. This overlap will greatly exaggerate the ^{70}Zn isotope, because the ^{70}Ge's 20.52% relative abundance dwarfs the ^{70}Zn's relative abundance (0.61%) – it is nearly 35 times greater. Adapted from Reference 56.

Polyatomic interferences must also be taken into account when quantifying by ICP-MS. Unfortunately, the strategy of quantifying the isobaric interferences and subtracting its intensity from the analyte signal is not feasible with polyatomic interferences. However, if a higher resolution mass spectrometer were employed, the differentiation between analyte and polyatomic interferences would no longer be an issue. The ICP-MS instrument used in this study had a quadrupole mass analyzer with a unit resolution. Therefore, polyatomic interferences could not be resolved. Strategies such as in the table below should be consulted when deciding which isotope to use for quantification for particular elements that are present in the sample matrix (in addition to the vast quantities of Ar and ambient air emitted by the plasma) being of paramount concern.

Isotope	Abundance	Interference
^{64}Zn	48.89	$^{32}S^{16}O_2{}^+$, $^{48}Ti^{16}O^+$, $^{31}P^{16}O_2{}^1H^+$, $^{48}Ca^{16}O^+$, $^{32}S_2{}^+$, $^{31}P^{16}O^{17}O^+$ $^{34}S^{16}O_2{}^+$, $^{36}Ar^{14}N_2{}^+$
^{66}Zn	27.81	$^{50}Ti^{16}O^+$, $^{34}S^{16}O_2{}^+$, $^{33}S^{16}O_2{}^1H^+$, $^{32}S^{16}O^{18}O^+$, $^{32}S^{17}O_2{}^+$, $^{33}S^{16}O^{17}O^+$, $^{32}S^{34}S^+$, $^{33}S_2{}^+$
^{67}Zn	4.11	$^{35}Cl^{16}O_2{}^+$, $^{33}S^{34}S^+$, $^{34}S^{16}O_2{}^1H^+$, $^{32}S^{16}O^{18}O^1H^+$, $^{33}S^{34}S^+$, $^{34}S^{16}O^{17}O^+$, $^{33}S^{16}O^{18}O^+$, $^{32}S^{17}O^{18}O^+$, $^{33}S^{17}O_2{}^+$, $^{35}Cl^{16}O_2{}^+$
^{68}Zn	18.57	$^{36}S^{16}O_2{}^+$, $^{34}S^{16}O^{18}O^+$, $^{40}Ar^{14}N_2{}^+$, $^{35}Cl^{16}O^{17}O^+$, $^{34}S_2{}^+$, $^{36}Ar^{32}S^+$, $^{34}S^{17}O_2{}^+$, $^{33}S^{17}O^{18}O^+$, $^{32}S^{18}O_2{}^+$, $^{32}S^{36}S^+$
^{70}Zn	0.62	$^{35}Cl^{35}Cl^+$, $^{40}Ar^{14}N^{16}O^+$, $^{35}Cl^{17}O^{18}O^+$, $^{37}Cl^{16}O^{17}O^+$, $^{34}S^{18}O_2{}^+$, $^{36}S^{16}O^{18}O^+$, $^{36}S^{17}O_2{}^+$, $^{34}S^{36}S^+$, $^{36}Ar^{34}S^+$, $^{38}Ar^{32}S^+$

Figure 43. Table of potential polyatomic interferences. Because samples were 1:100 dilutions of industrial effluent in 1% (v/v) HNO_3, elements other than H, N, and O were expected to be relatively minor in concentration. Adapted from Reference 57 .

The choice of which Zn isotope to use for quantification was based upon consideration of potential interferences. ^{67}Zn and ^{70}Zn were eliminated because they possess a much lower percent abundance than the other isotopes and would thus lead to a much lower instrument response. In addition, ^{70}Zn has a major isobaric interference with ^{70}Ge. ^{64}Zn has the highest percent abundance, but has an isobaric overlap with ^{64}Ni as well as a polyatomic interference with $^{36}Ar^{14}N_2{}^+$. While ^{36}Ar is a minor isotope (0.3337% relative abundance), the Ar plasma has an overall flow rate of >10 L/min, so appreciable levels of even minor Ar isotopes will be present. The sample matrix contains high levels of N (1% v/v HNO_3 with additional N supplied by the atmosphere). Therefore, while a tri-atomic interference is unlikely to form, the presence of ^{64}Ni and $^{36}Ar^{14}N_2{}^+$ ion prevents monitoring ^{64}Zn. Lastly, ^{68}Zn was eliminated as the quantification ion because not only does it have the lowest percent abundance of the three remaining Zn isotopes (18.45% relative abundance), and

because ^{40}Ar is the Ar isotope (99.600%), $^{40}Ar^{14}N_2^+$ ion would potentially be present in even greater quantities than the $^{36}Ar^{14}N_2^+$ ion. The choice of the ^{66}Zn isotope is strengthened because it has the lowest percent error in relative abundance (see Table 10). Note that all percent errors are positive because the major sources are isobaric and polyatomic interferences contributing to the signal. Finally, there are not any isobaric interferences for ^{66}Zn.

Any unavoidable isobaric interferences can, and should be corrected by measuring the interfering species and subtracting its intensity from the analyte signal. However, this method does introduce a relatively minor amount of error into the measurement by virtue of relying on additional measurements (which also possess errors). Therefore if isobaric interferences are unavoidable, the isotope with the fewest isobaric interferences should be chosen for quantification because these minor errors are additive.

m/z	66	67	68	70
Expected	56.40	8.22	37.52	1.24
Observed	67.2	16.4	65.6	7.9
% Error	19.1	99.5	74.8	537

Table 10. Comparison of relative intensities between Figures 39 and 40. m/z 64 is not compared, as relative intensities are taken as a percentage relative to the base peak which is considered to be 100%.

Authentic industrial process samples were collected to test selectivity of the prototype instrument. Using the above strategies, elemental determinations were

made so the source of the matrix effects (as seen in Figure 33) could potentially be

determined. Additionally, an alternate method to obtain Zn concentrations in the

process samples was desired so the new "initial rate" method could be compared with

results from a proven analytical method.

Because the dye films are designed to bind positive ions, any cation may

potentially be an interferent. However, to what extent it will interfere with the

analyte depends on factors such as how well the interferent binds to the dye film

being used (i.e., charge and ionic radius), as well as its disassociation constant with

respect to the dye film (will it accumulate on the dye film over time with acid washes

being ineffective).
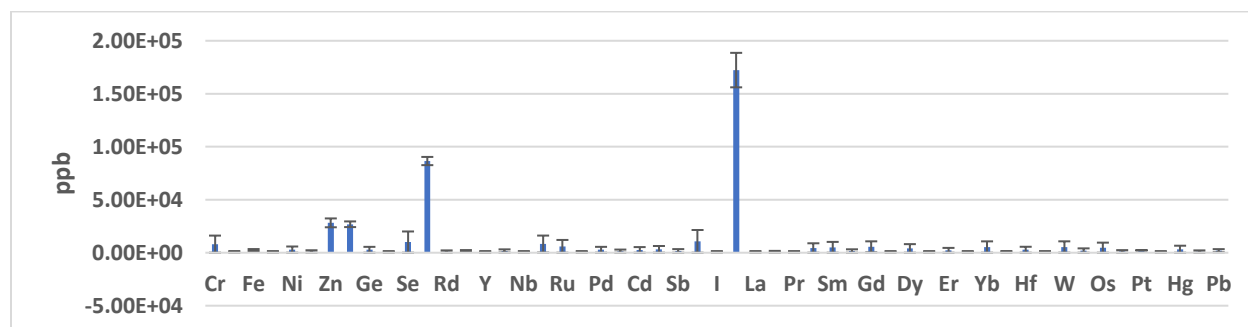
Figure 44. Selected ICP-MS Elemental Spectra for a single industrial sample. Levels were corrected as detailed above and show total elemental amounts. Error bars represent the Student's t value at the 95% confidence interval (n = 3).

Because the initial "proof of concept" testing of the prototype monitor focused

on measuring Zn, this element was present in all samples. Zn was chosen because it

sees much use in galvanization to prevent rusting of Fe, steel, and other metals. Over

900,000 tons of Zn were used in the U.S in 2019.[58] Therefore, using Zn for the initial

proof of concept would allow for a greater number of potential test sites than other analytes. Figure 45 shows a comparison of the Zn abundances that were observed in the industrial effluent samples. The Zn levels showed an average of 3.07×10^4 ppb and a range of 1.07×10^4 ppb.

Figure 45. Comparison of Zn abundance in industrial effluent samples. Error bars represent the Student's t value at the 95% confidence interval. (n = 3)

Because salts of first row transition metals are expected to form octahedral complex ions when dissolved in water,[59] ionic radii for Zn is given only for the octahedral state in Table 11.

	Ionic Radius (pm)
Zn^{+2} Octahedral	88.0

Table 11. Ionic Radius for Zn^{+2} ion. Adapted from Reference 60.

Fe is expected to enter the effluent because it travels through the industrial pipes ever-changing conditions (i.e., corrosion). This may happen either because of low pH, or because of corrosive chemicals (like $FeCl_3$) flowing through the industrial pipes. For example, Fe salts such as $FeCl_3$ can be used as part of the waste water treatment process. If treatment with $FeCl_3$ is performed upstream from the process monitor, pipes will face additional corrosion since $FeCl_3$ is exceptionally corrosive.[61] Additionally, Fe cations will also be expected upon disassociation with any Fe salts. Figure 46 shows a comparison of Fe abundances that were observed in the industrial effluent samples. The Fe levels showed an average of 2.07×10^3 ppb and a range of 8.35×10^2 ppb.
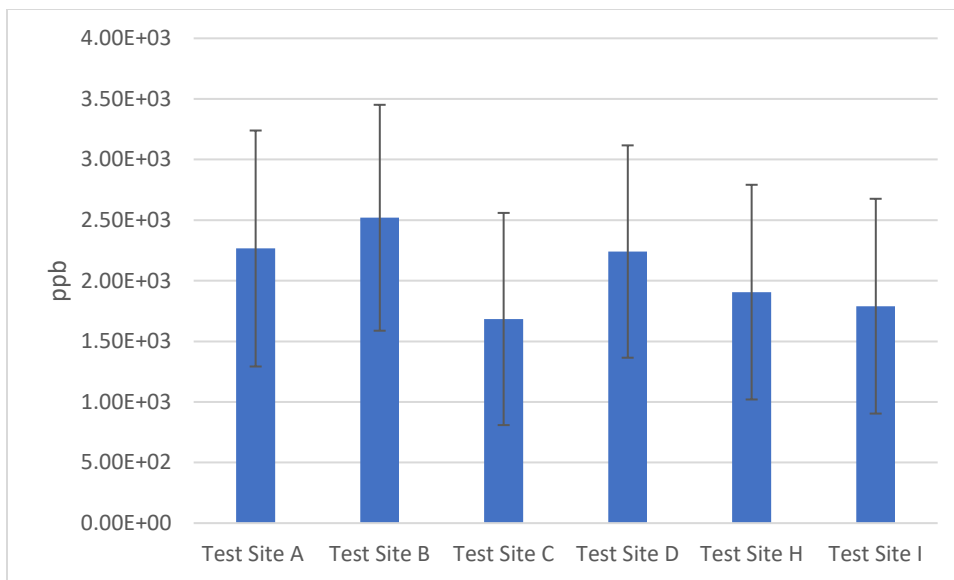
Figure 46. Comparison of Fe abundance in industrial effluent samples. Error bars represent the Student's t value at the 95% confidence interval. (n = 3)

The ionic radius of Fe depends not only on which charge state it is in, but also the coordination number of the complex. Because salts of first row transition metals are expected to form octahedral complex ions when dissolved in water, ionic radii for Fe are given only for the octahedral state in Table 12.[59] Fe^{+2} and Zn^{+2} not only are both divalent, they also possess similar ionic radii (92.0 and 88.0 pm respectively). Therefore, Fe^{+2} is expected to be a major interferent because it has the same charge state and a similar ionic radius.

	Ionic radius (pm)
Fe^{+2} Octahedral	92.0
Fe^{+3} Octahedral	78.5

Table 12. Ionic radius values for Fe cations. Only values for high spin complexes given, as Fe^{+2} forms a high spin complex with water. Adapted from Reference 62.

Ga is used in the manufacture of electronic circuits, semiconductors and light-emitting diodes. In 2018, 32,000 kg of Ga was imported into the Unites States.[63] Over 95% of Ga use is in the form of GaAs, with analog integrated circuits seeing the most consumption.[64] Figure 47 shows a comparison of the Ga abundance in the industrial effluent samples. The Ga levels showed an average of 2.93×10^4 ppb and a range of 1.00×10^4 ppb.
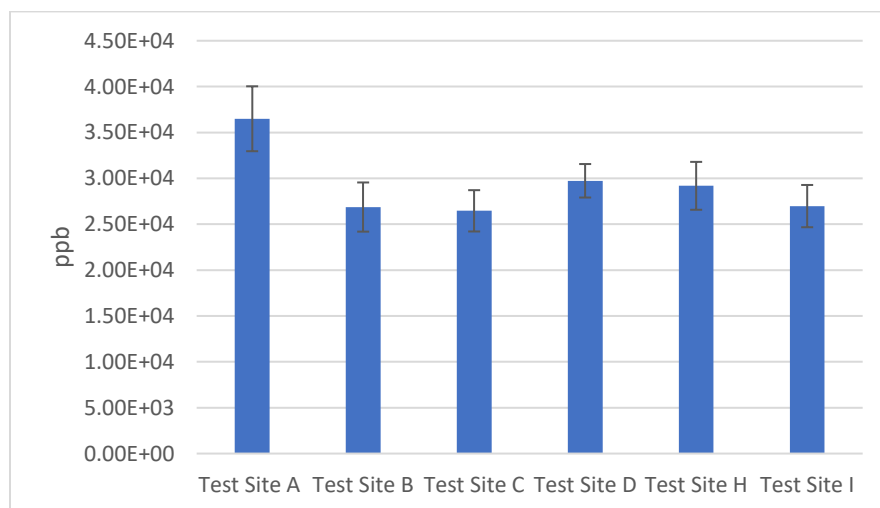
Figure 47. Comparison of Ga abundance in industrial effluent samples. Error bars represent the Student's t value at the 95% confidence interval. (n = 3)

Table 13 shows the ionic radii for Ga^{+3}. As Ga is not reactive with water in its elemental form, and a determination of which major ligating species were present was not done; the coordination state was unknown. Therefore, both coordination states had to be considered. While the ionic radius of the octahedral complex was not close to Zn^{+2} (88.0 pm), it is more charged and therefore a concern.

	Ionic Radius (pm)
Ga^{+3} tetrahedral	61
Ga^{+3} octahedral	76.0

Table 13. Ionic radii for Ga^{+3} ion. Adapted from Reference 65.

Ba is commonly found in environmental samples, but can be a concern because of "space charging" interferences in ICP-MS. Space charging occurs as the focused beam of positively charged ions travels from the plasma torch towards the detector. This tight grouping causes the like charged particles to electrostatically repel one another with the expelled ions never making it to the detector. Lighter elements are more likely to be expelled from the beam than heavier ones because they have less kinetic energy.[66-67] Therefore, space charging interferences are always of concern in ICP-MS determinations whenever an element is (1) heavier than the analyte and (2) in large excess in comparison to the analyte. This is the case with all elements presented up to this point. Ba abundance is almost an order of magnitude greater than Zn and Ga and almost two orders of magnitude greater than Fe. Figure 48 shows

a comparison of the Ba abundance in the industrial effluent samples. The Ba levels showed an average of 1.79×10^5 ppb and a range of 5.28×10^4 ppb.
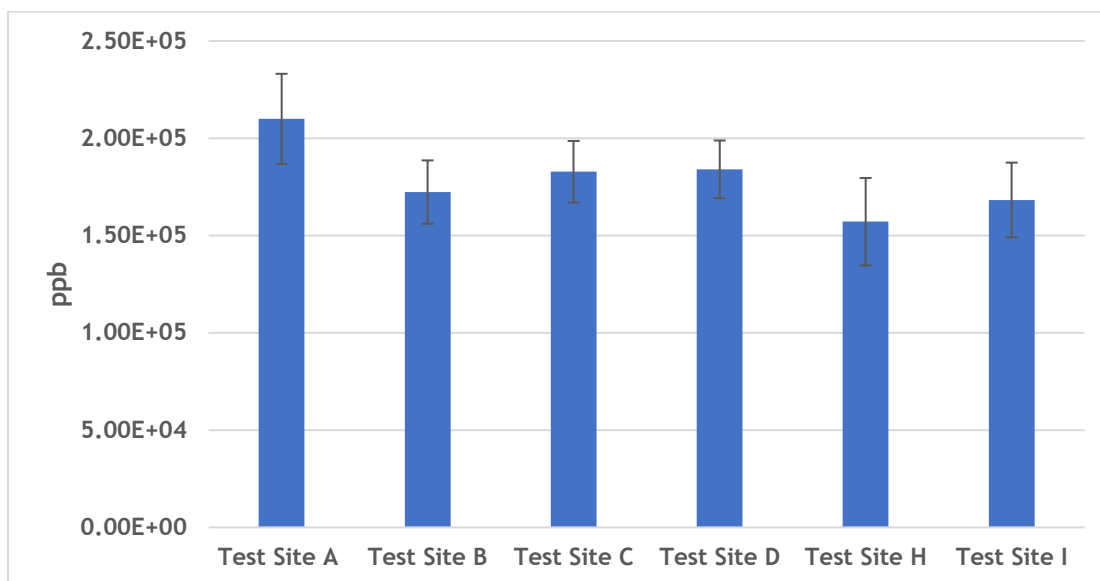
Figure 48. Comparison of Ba abundance in industrial effluent samples. Error bars represent the Student's t value at the 95% confidence interval. (n = 3)

Table 14 shows the ionic radii for Ba^{+2} complexes. Both Zn^{+2} and Ba^{+2} are both divalent. Additionally it is the major elemental species, almost an order of magnitude greater than Zn, so even if the dye film is very selective towards Zn and away from Ba, the sheer weight behind Ba may cause interferences. However, their ionic radii are different enough so that dye films which are selective enough can be engineered.

	Ionic Radius (pm)
Ba^{+2} Octahedral	149
Ba^{+2} 8 coordinate	156

Table 14. Ionic radii for Ba^{+2}. Adapted from Reference 68 .

Br containing compounds are commonly used to control buildup of bacteria, viruses, and other microorganisms during industrial processes.[69] Figure 49 shows a comparison of the Br abundance in the industrial effluent samples. The Br levels showed extreme variability with an average of 3.46 x 10^4 ppb and a range of 1.11 x 10^5 ppb. It is not clear why Br only appears in detectable amounts from two of the industrial samples.
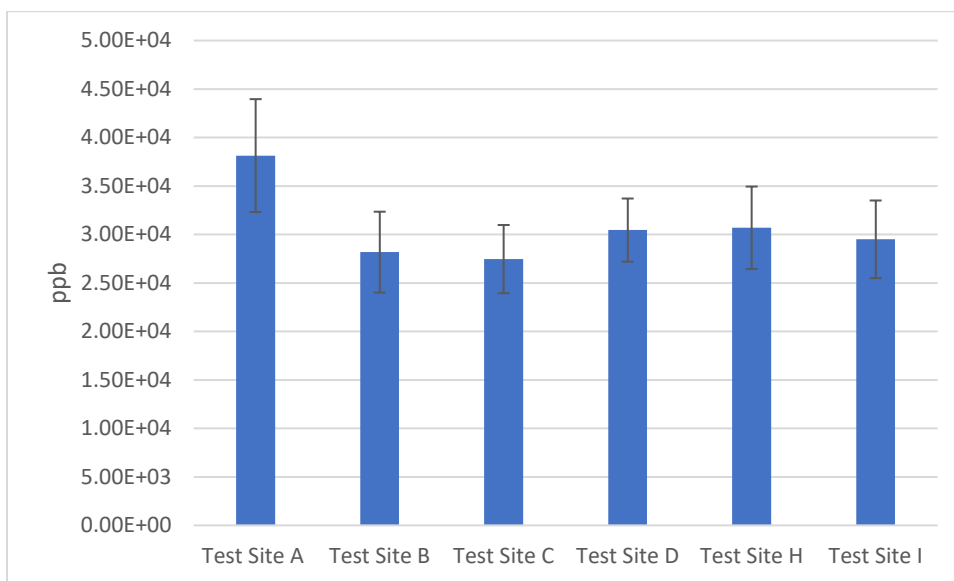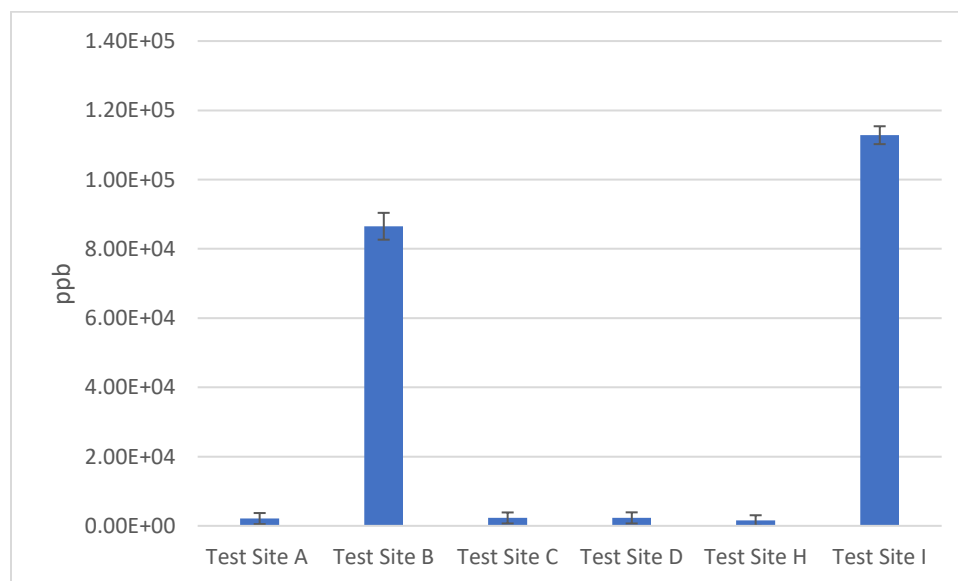

Figure 49. Comparison of Br abundance in industrial effluent samples. Error bars represent the Student's t value at the 95% confidence interval. (n = 3)

A table for the ionic radii of Br is not given because Br is an anion in solution and therefore not expected to interfere with the dye films.

The goal of the ICP-MS research was to determine candidates for the optimal initial testing site for the prototype process monitor. While the ICP-MS work uncovered the presence of several potentially interfering elements, it still remained unclear which (if any) were behind the severe matrix effects seen. The potential interfering elements in the process samples were narrowed down and levels of Zn were determined by an alternate method from dye films.

The main goals of the SIA study focused on addressing problematic issues that could arise during the determination of metal cations in industrial effluents using the SIA process monitor. Previous work had shown that ionic strength and solution pH affect the dye films' ability to be used as a chemosensor of metal cations in solution. This research used the earlier work to focus on pH and ionic strength and additionally focused on elemental matrix effects. An approach was developed using absorbance data to create an "initial rate" model of measurement and the time frame chosen for the "initial rate" method was investigated.

3.8 Overview of the Brawner Farm Study

In 2004 and 2007, soil core samples were collected from the Manassas National Battlefield in Virginia to support a study of speciation, transport, and fate of metals in soil. The soil cores were extracted with HNO_3 (0.5 M) for 24 hr with constant

stirring. ICP-MS analysis from m/z 50-238 of a 1:100 dilution of the extract was made to determine the distribution of metals in the samples.

The initial studies of the soils examined the Pb speciation, distribution, and transport, finding that in general most of the Pb (~25%) was metal oxide-bound.[35]

Subsequent research examined Cu and found more varied results. For Region A, 43% of Cu was in the metal oxide fraction with <10% found in Regions B and C. Additionally, Hg in all three regions was studied using 6 M HNO_3 instead of the metal oxide fraction of the BCR as used in the present work. It was shown that 22% of the total Hg was found in Region A and 51% was distributed in Region B. A mass balance for all fractions of the BCR procedure was undertaken for Region B. Only 13.33% of the total Hg in Region B was in the metal oxide fraction, this fraction was nevertheless chosen for study because of an unexpected phenomenon which was observed for Cu and Fe. Increasing the ramp time of the microwave extraction would be expected to show an increasing concentration of any bound analytes, with an eventual plateau after all analyte has been extracted. However, a bi-modal extraction was found instead in the metal oxide fraction of core 32. The Cu concentration increased as expected with ramp times from 13 to 17.5 min with a plateau from 17.5 to 21 min. However, an additional increase was observed when going from 21 to 25 min. After 25 min, the expected plateau continued for up to 35 min. Similar behavior was observed for Fe.[36]

Therefore, the metal oxide fraction for depths between three and four inches of soil cores 32 (32.5 yards), and adjacent core 31 (27.5 yards) and core 6 (35.0 yards)

were chosen because the goal of this project was to determine if Hg showed a similar bi-modal release as Cu and Fe showed for core 32 in previous work.[36] The first step of this project was to first isolate the cores / depths that contained Hg. This would allow for a subsequent investigation of increasing ramp times on the isolated cores / depths.

3.9 Sample Treatment

Sequential Extraction is an important tool in determining the speciation of trace metals.[70] Methods employed prior to Sequential Extraction were limited to establishing total metal concentration.[69] With the advent of Sequential Extraction in the 1970's, scientists were able to determine the speciation of metals in various "compartments".[69] This is done by extracting metals from the sample with successively harsher treatments. Therefore, levels of metals which exist in the exchangeable, carbonate-bound, metal oxide-bound, organic-bound, and refractory-bound "compartments" are able to be measured.[69]

Figure 50 shows an example of a Sequential Extraction procedure. The sample is treated with the chemicals under "Reagents" at the left and then centrifuged with the supernatant decanted for analysis. The pellet at the bottom of the centrifuge tube is then extracted with subsequent reagents.

EXTRACTION

Reagents   Extracts

S

MgCl$_2$ ──────────────   "Exchangeable"
                                            1

R

NaOAc ──────────────   "Carbonates"
                                            2

R

HONH$_2$HCl, HOAc ──────────   "Oxide"
                                            3

R

H$_2$O$_2$, HNO$_3$ ──────────
H$_2$O$_2$ ──────────
NH$_4$OAc,HNO$_3$ ──────────   "Organics"
                                            4

R

Digestion ──────────────   "Residuals"
                                            5
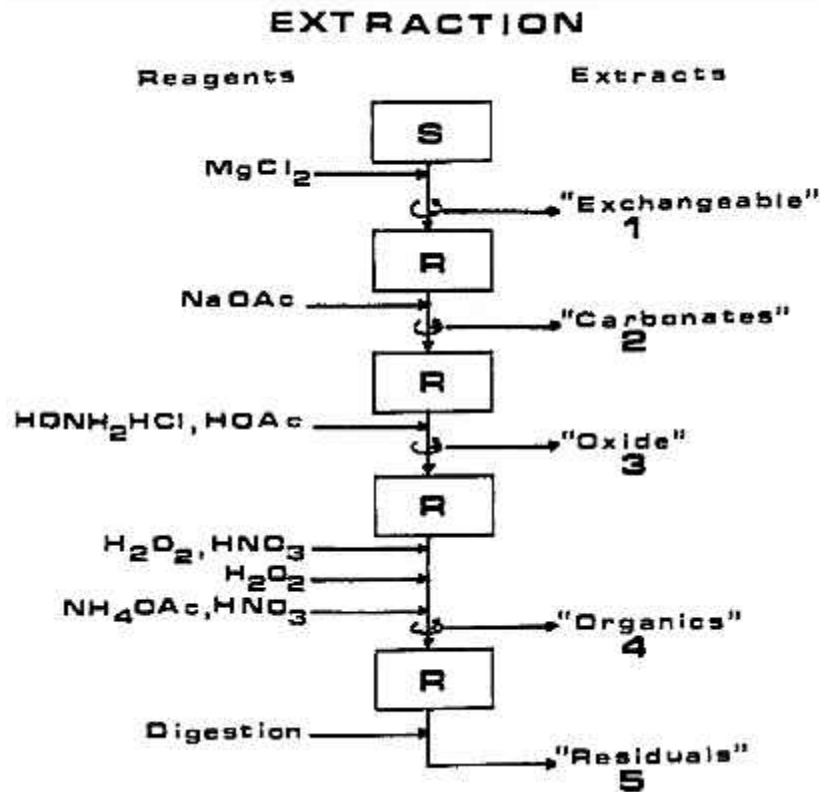
Figure 50. Example of a Sequential Extraction procedure. [71]

An initial drawback of this method was that it took an extended period of time requiring each extraction step to be mixed for 12-24 hr after each of the five treatments. To increase throughput, MAE has been reported, that is, making use of microwave energy to speed up the Sequential Extraction process.[72] Figure 51 depicts the CEM Model MARS 5 MAE system used in this project.
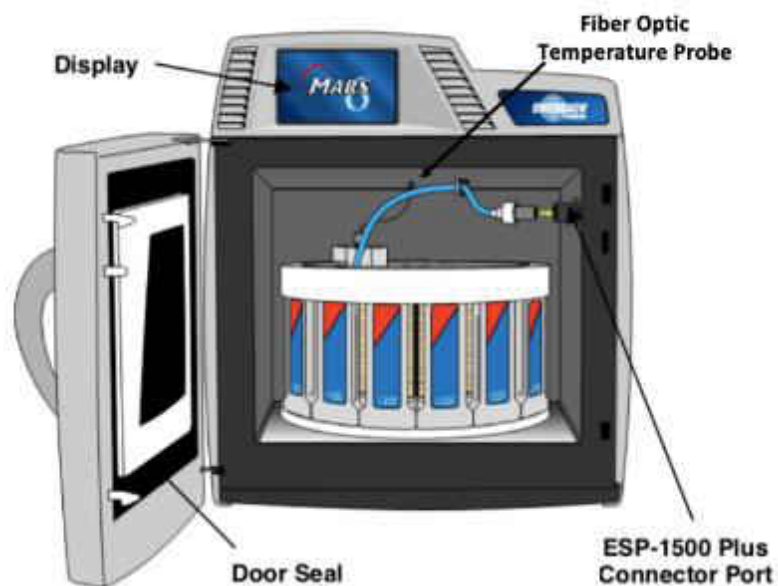
Figure 51. Schematic diagram of the MARS 5 microwave extractor. [73]

3.10 ICP-MS Elemental Analysis of BF Soil

Elements of interest were Cu, Hg, and Pb. Cu, Hg, and Pb were major components of Civil War ammunition.[74-75] Calibration models were created that corresponded to the two ICP-MS modes employed: "full scan" and "selected ion monitoring" (SIM). "Full Scan" was used to measure the presence of metals from m/z 50 to 238, with the exception of isotopes corresponding to Cu, W, Hg, and Pb. In this mode, the MS measured each m/z value for 0.80 s by averaging four scans (i.e., the integration time for each scan was 0.20 s). In SIM mode the isotopes for the elements of interest were quantified. In SIM mode, the MS measured the selected m/z values for 4.0 s (n=4) (i.e., each scan's integration time was 1.0 s). A longer integration time would of course result in a higher signal, however, this was not observed in two cases that are described below.
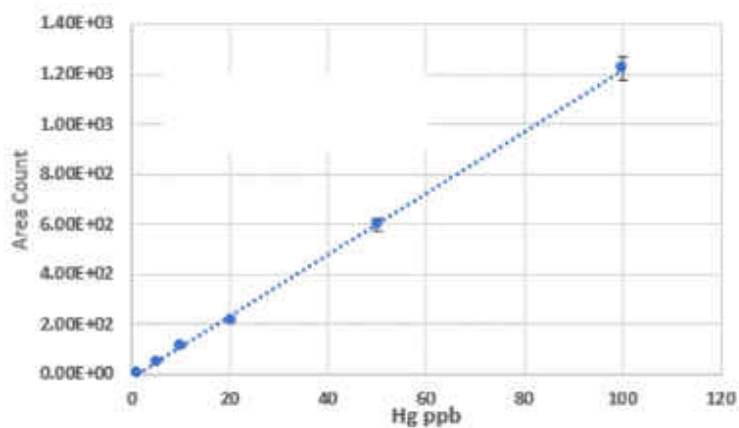
Figure 52. "Full Scan" calibration model for ^{202}Hg. The LOD was 1.81 ppb, and error bars represent the Student's t value at the 95% confidence interval (n=3).

Linear Regression Model:

Slope = 12.3 Area Count x Hg (ppb)$^{-1}$

Intercept = 11.0 Area Count

SEE = 12.3 Area Count
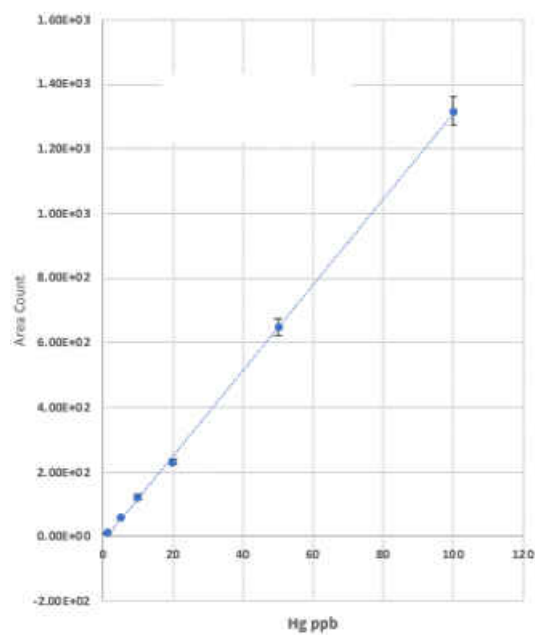
Figure 53. SIM mode calibration model of ^{202}Hg. The LOD was 2.25 ppb. All error bars represent the Student's t value at the 95% confidence interval (n=3).

Linear Regression Model:

Slope = 13.3 Area Count x Hg (ppb)$^{-1}$

Intercept = 13.6 Area Count

SEE = 13.1 Area Count

Because in SIM mode, the integration time was five times greater, it was expected that the calibration model would have a slope which was also (approximately) five times greater. However, only a modest increase (7.52%) was observed. It was unclear why this occurred because both models were created using the same set of standards. LOD (3σ) was calculated using Student's t value at 95%

confidence (n=3). The LOD in SIM mode was only 24.3% higher than in Full Scan mode

(2.25 ppb as opposed to 1.81 ppb). A LOD less than five times lower is expected in

the SIM mode because while the increased integration time increases the signals of

the calibration standards, it increases the signal noise as well. Therefore, when

comparing the Signal to Noise ratios (S/N) a small increase in the S/N of the SIM

relative to the Full Scan mode is expected for the low Hg standard (1 ppb) with larger

increases for higher standards (the noise remains constant while the signal increases,

and a longer integration time exaggerates this difference). However, when

comparing the S/N for the standards there is no discernable trend (as seen in Figure

54).
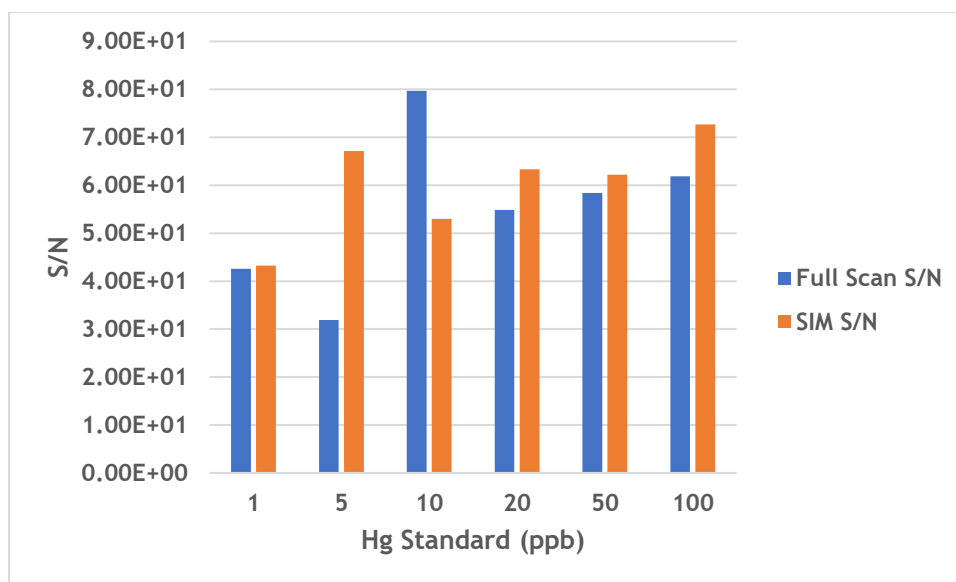
Figure 54. Comparison of S/N values for standards run in Full Scan and SIM modes.

This did not pose a problem, however, because all elements of interest were present above their respective LODs.

Soil Core Name	Position
6A	27.5 Yards
32A	32.5 Yards
32B	32.5 Yards (replicate core taken at same position as 32A)
31B	35.0 Yards

Table 15. Position of soil core samples relative to each other.

For site "6A 3-4", "6A" refers to the first replicate (A) soil core taken at the 27.5 yard mark (site 6), which is measured south from the center (origin) of the Union infantry line. "3-4" indicates that the soil depth was between 3 and 4 inches, corresponding to the year 1928±10 as determined radiometrically.[35] Results were corrected by using an internal standard (^{115}In). In was added to all samples, but it's not possible to use the ^{115}In internal standard to correct the ^{115}In itself, so only the ^{115}In is not corrected.

Geographic maps with elemental distributions are available for the continental United States. However, it should be noted that these cited values are total values in soil, and levels found in this project are specifically for elements found in metal oxides. Therefore, the levels found here are expected to be lower.

Mn has an overall crustal abundance of 774 ppm.[76] One of the areas with the lowest determined value in the continental U.S. was in eastern North Carolina (less

than 139.112 ppm) and one of the areas with the highest value determined was in northern Kentucky (more than 1336.05 ppm). In northern Virginia, Mn ranges from 958.372 to 1089.93 ppm in soil.[77] These Mn levels are about double those found in this project. Figure A1 and Table A1 show the Mn distribution in soil. While not found in Civil War bullets or primers, nevertheless, an interesting distribution was found.

Fe has an overall crustal abundance of 5.22×10^4 ppm.[78] The lowest value in the continental U.S. was determined in northern Louisiana (less than 0.643 wt% (6.43 $\times 10^6$ ppb)) and the highest value was determined in northern California (more than 5.343 wt% (5.343×10^7 ppb)). In northern Virginia, Fe ranges from 3.792 to 4.361 wt% (3.792×10^7 to 4.361×10^7 ppb) in soil.[79] These values are about ten times higher than those found in this project. Figure A2 and Table A2 show the Fe distribution in soil.

Co has an overall crustal abundance of 26.6 ppm.[80] The lowest value in the continental U.S. was determined in southern Florida (less than 0.555 ppm) and the highest value was determined in eastern Oklahoma (more than 15.31 ppm). In northern Virginia, Co ranges from 12.171 to 15.309 ppm in soil.[81] These values are about four times lower than those found in this project. However, the unusually high Co levels may have come in part from broken medicine bottles which used the element for coloring.[82] While the cobalt blue bottles have the most obvious connection, Co compounds were used in the production of the other colors of glass as well.[83] Figure A3 and Table A3 show the Co distribution in soil.

Ni also has an overall crustal abundance of 26.6 ppm.[84] The lowest value in the continental U.S. was determined in southeastern Utah (less than 3.542 ppm) and the highest value was determined in central Arizona (more than 46.59 ppm). In northern Virginia, Ni ranges from 10.615 to 11.902 ppm in soil.[85] These values are close to those found in this project.

Figure A4 and Table A4 show the Ni distribution in soil. While present in Pb shot, it is a very minor component (0.5% w/w), and likely did not contribute much to levels that would have been otherwise present without the battle having taken place. Additionally, all samples (except 32B 6-7) fall within error bars of the Sand Blank.

Cu has an overall crustal abundance of 27 ppb.[86] The lowest value in the continental U.S. was determined in central Nebraska (less than 3.338 ppm) and the highest value was determined in southwestern Oregon (more than 40.764 ppm). In northern Virginia, Cu ranges from 21.493 to 24.408 ppm in soil.[87] These values vary between two and five times those found in this project.

Figure A5 and Table A5 show the Cu distribution in soil. Cu is a major component of Civil War primers. While Cu was found in the metal oxide fraction of soil core 32 during previous work (Table 16),[36] the results presented in the appendix here are not statistically different from each other (including the Sand Blank). Additionally, error bars include zero, so the null hypothesis cannot be rejected. Because the Student's t values at the 95% confidence interval for this work (Table 19) and previous work (Table 16)[36] overlap, the two results are not statistically different.

	Cu (ppb)	95%
32 B 3-4	3.05E+03	9.09E+02
32 B 4-5	2.69E+03	3.47E+02
32 B 5-6	1.97E+03	3.14E+02
32 B 6-7	1.20E+03	2.74E+02
31 A 3-4	4.52E+03	6.74E+02
31 A 4-5	4.25E+03	9.50E+02
31 A 5-6	4.27E+03	4.14E+02
31 A 6-7	3.51E+03	7.76E+02

Table 16. Adapted from Reference 36.

Zn has an overall crustal abundance of 72 ppm.[88] The lowest value in the continental U.S. was determined in southern Mississippi (less than 14.949 ppm) and the highest value was determined in eastern Pennsylvania (more than 119.065 ppm). In northern Virginia, Zn ranges from 62.593 to 66.182 ppm in soil.[89] These values are about four times those found in this project. Figure A6 and Table A6 show the Zn distribution in soil. All samples (except 31B 3-4) fall within the error bars of the Sand Blank.

Ga has an overall crustal abundance of 16 ppm.[90] The lowest value in the continental U.S. was determined in northern Louisiana (less than 2.738 ppm) and the highest value was determined in central Oregon (more than 24.128 ppm). In northern Virginia, Ga ranges from 9.0343 to 10.02 ppm in soil.[91] These values are about the same as those found in this project. Figure A7 and Table A7 show the Ga distribution in soil.

Ba has an overall crustal abundance of 456 ppm.[92] The lowest value in the continental U.S. was determined in southeastern Georgia (less than 33.483 ppm) and

the highest value was determined in northeastern South Dakota (more than 840.013 ppm). In northern Virginia, Ba ranges from 124.67 to 164.663 ppm in soil.[93] These values are comparable to those found in this project.

Figure A8 and Table A8 show the Ba distribution in soil.   Ba is ever present in natural sources, and was expected to be a major element, if not the major element measured.

La has an overall crustal abundance of 0.3 ppm.[94] The lowest value in the continental U.S. was determined in southern Florida (less than 9.285 ppm) and the highest value was determined in central South Carolina (more than 117.526 ppm). In northern Virginia, La ranges from 34.331 to 36.704 ppm in soil.[95] These values are about three times those found in this project. Figure A9 and Table A9 show the La distribution in soil.

Ce also has an overall crustal abundance of 0.3 ppm.[96] The lowest value in the continental U.S. was determined in northern Michigan (less than 29.067 ppm) and the highest value was determined in north central Idaho (more than 153.821 ppm). In northern Virginia, Ce ranges from 51.486 to 54.15 ppm in soil.[97] These values are about five times those found in this project.

Figure A10 and Table A10 show the Ce distribution in soil. While not found in Civil War bullets or primers, nevertheless, an interesting distribution was found. It is unclear why 32B 6-7 has higher levels of Ce than other cores and depths.

Au has an overall crustal abundance of 0.0013 ppm.[98] The lowest value in the continental U.S. was determined in northwestern North Carolina (less than 0.239 ppb)

and the highest value was determined in northeastern Colorado (more than 7.708 ppb). In northern Virginia, Au ranges from 0.295 to 0.374 ppb in soil.[99] These values are dwarfed by those found in this project.

Figure A11 and Table A11 show the Au distribution in soil. While not found in Civil War bullets or primers, all samples and standards had Au standard added to make them 1.0 ppm. This is done because the Au helps to stabilize Hg for ICP-MS analysis. However, it is unclear why Au was only present in significant levels for the Sand Blank.

Hg has an overall crustal abundance of 0.03 ppm.[100] The lowest value in the continental U.S. was determined in northern Missouri (less than 0.008 ppm) and the highest value was determined in northern Virginia (more than 0.136 ppm).[101] These values are about fifty times lower than those found in this project.

Figure A12 and Table A12 show the Hg distribution in soil. Hg is a major component of the explosive compound ($Hg(CNO)_2$) in Civil War primers. While found in levels which exceeded the LOD, all samples were not statistically different from each other (including the Sand Blank). Additionally, all error bars go through zero. While these values (Table 19) agree with those found in previous work (Table 17),[36] a different extraction method was used. In this work, ppb values were obtained for the metal oxide fraction of soil samples. In previous work, Hg levels were evaluated in a similar manner, but concentrated HNO_3 was used as the extractant. The work in this study used successively harsher chemicals for extractions. Because the values found in the previous work[36] are within error bars of the values found here, they are not

statistically different. However, no definitive conclusions can be drawn as to how much Hg is speciated in the metal oxide fraction because the error bars found in this project go through zero. Additionally, all fractions studied here are not statistically different than the Sand Blank. Unfortunately, no studies for Hg were performed where both the same soil cores and the same method coincided.

	Hg (ppb)	95% (n=3)
6A 3-4	8.19E+01	6.10E+00
6A 4-5	7.17E+01	9.44E+00
6A 5-6	6.07E+01	4.22E+00
6A 6-7	4.63E+01	4.95E+00

Table 17. Adapted from Reference 36.

Pb has an overall crustal abundance of 11 ppm.[102] The lowest value in the continental US was determined in central Washington (less than 8.887 ppm) and the highest value was determined in central Colorado (more than 41.314 ppm). In northern Virginia, Pb ranges from 28.822 to 32.477 ppm in soil.[103]

Figure A13 and Table A13 show the Pb distribution in soil. Pb is a major component of Civil War shot (97% (w/w)). An interesting distribution was observed in that as Pb levels are distributed through the various depths of 6A and 31B, most Pb found from site 32 was observed between 3 and 4 inches (depth was dated 1948) (Table A13). The next deeper fraction (32A 4-5) was dated 1883. Tetraethyl Pb was discovered as an anti-knock additive for gasoline in the early 1920's and made commercially available shortly afterwards.[104] The emissions could have added to the

soil levels of any depth dated during the time period when tetraethyl Pb was in use

(early 1920's to 1996).[105] However, it was previously shown that by using isotopic

fingerprints that new Pb can be differentiated from the Pb deposited through the Civil

War battle.[35] Moreover, it was shown that a soil sample taken next to a highway near

the battle site had a different isotopic fingerprint than soil samples taken directly

from the battlefield.[35] While different Pb values were found for the same depths, the

compared values are for cores 2.5 yards before and after the core used previously.[35]

Additionally, somewhat different extraction methods were used. While all chemicals

and centrifuging protocols were the same, this work used microwave energy to reduce

extraction time (~40 min) and the previous work used a rotary shaker (over 16 hr).[35]

	Pb (ppb)	95%
5A 3-4	7.36E+01	1.81E+01
5A 4-5	9.42E+01	2.50E+01

Table 18. Values previously found for Pb for cores closest to cores used in this study. Core 5A is positioned at 30 yards, 6A at 27.5 yards, 32 (A and B) at 32.5 yards, and 31 at 35.0 yards. Adapted from Reference 35.

Figure A14 and Table A14 show the 50 ppb Hg Quality Control (QC) sample

data. The QC standard was verified as every third sample, (not including the

standards used during calibration). Because all 50 ppb Hg QC samples fall within error

bars of each other, little instrument drift occurred.

Figure A15 and Table A15 show the In distribution across samples. 50 ppb In

was used as the internal standard across all soil samples.

Soil Core	Pb average (ppb)	Pb (95%)	Cu average (ppb)	Cu (95%)	Hg average (ppb)	Hg (95%)
6A 3-4	2.26E+05	1.39E+04	4.37E+03	8.06E+03	3.12E+03	3.48E+03
6A 4-5	2.17E+05	1.09E+04	5.89E+03	1.14E+04	3.54E+03	3.86E+03
6A 5-6	1.15E+05	8.07E+03	5.01E+03	9.50E+03	3.08E+03	3.39E+03
6A 6-7	1.51E+05	9.08E+03	7.24E+03	1.35E+04	5.60E+03	6.17E+03
32A 3-4	1.78E+05	1.24E+04	9.60E+03	1.87E+04	4.84E+03	5.20E+03
32A 4-5	5.84E+04	4.33E+03	1.05E+04	2.07E+04	5.24E+03	5.75E+03
32B 5-6	4.79E+04	3.92E+03	1.15E+04	2.28E+04	4.80E+03	5.21E+03
32B 6-7	5.22E+04	2.94E+03	1.25E+04	2.49E+04	5.19E+03	5.68E+03
31B 3-4	1.71E+05	9.90E+03	6.11E+03	1.12E+04	4.77E+03	5.11E+03
31B 4-5	1.20E+05	4.67E+03	5.05E+03	9.08E+03	4.75E+03	5.18E+03
31B 5-6	1.17E+05	7.61E+03	6.64E+03	1.24E+04	4.44E+03	4.86E+03
31B 6-7	7.67E+04	3.52E+03	5.08E+03	9.29E+03	4.06E+03	4.52E+03
Sand Blank	2.89E+03	2.13E+03	1.68E+03	2.07E+03	3.80E+03	4.05E+03

Table 19. Summary data for Pb, Cu, and Hg.

Chapter 4: Conclusions and Future Work

In this thesis, methods for measuring toxic metals over a broad concentration range in complex matrices were successfully developed and applied to authentic samples. The commonality between these projects was determining toxic metals at relatively high (ppm) and low (ppb) concentrations as well as their presence in notoriously difficult matrices - industrial wastes and soil extracts. In the first project, a novel method using a prototype monitor based upon flow analysis coupled to spectrophotometry was developed. This method was applied to the determination of Zn at low ppm levels in industrial wastewater samples. In the second project, the abundance and distribution of a range of heavy metals that had been deposited in Civil War battlefield soil over 150 years ago was studied. The SIA study thus focused more on quantitative analysis, solidly in the "analytical chemistry" realm of scientific inquiry, whereas the soil study was more qualitative in nature, decidedly in the "environmental chemistry" domain.

Heavy metal contamination has an important and often detrimental impact on the environment. Contamination can spread through the atmosphere, soil, sediment, water, and biota. The work presented in this thesis was based upon two separate projects to study heavy metals in the environment. The SIA project focused upon the development, optimization, and application of a real-time monitor for Zn in industrial process waste streams. Two significant problems that were encountered should be studied further: (a) the influence of instrument drift on measurement integrity, and (b) the physical de-lamination of the sensor film in the flow cells. The Brawner Farm

project was concerned with identifying Hg in the soil along the sampling transect. Examination of specific MAE conditions (e.g., temperature ramp design) should be further studied to determine whether Hg also demonstrates a bi-modal release, as observed in previous studies.[35]

4.1 SIA Process Monitor Prototype

The studies described herein showed severe matrix effects on the dye films (even with 1:100 dilutions for three of the industrial effluents). These matrix effects caused significant instrument drift, resulting in greater variability (as shown in the larger error bars) or irreversible alteration of the dye film's response to Zn. Additionally, physical detachment of the dye film from the glass slides ("de-lamination") typically occurred after less than 20 experiments, which is an impractical situation for an industrial process monitor. These two problems showed the need for the development of more robust dye films (i.e., both chemically and mechanically). Future work should also include changing the number of initial rate experiments from three to four. Once these issues are addressed, future studies should focus on other metal analytes in industrial waste effluents with an array of dye films to determine multiple metals simultaneously. Such an instrument would provide a cost-effective and reliable means of monitoring metals in (near) real-time.

4.2 Brawner Farm

Further "mapping out" of the Hg in the soil as well as a more detailed study of the release of Hg during the MAE process should be undertaken in the future. Additionally, the ICP-MS method should be optimized. Specifically, in the work described herein, the ICP-MS method for the Brawner Farm soil samples was changed in three ways (Table 20).

	SIA Prototype	Brawner Farm	Reduction
Number of scans of the m/z range	10	4	60%
Sample throughput	20 min / sample	10 min / sample	50%
Integration period	2000 ms	800 ms	60%
Sample Volume	10 mL	5 mL	50%

Table 20. Changed to the ICP-MS method for the Brawner Farm samples compared to the method used to support the SIA Prototype study.

However, the resulting loss of resolution for the Brawner Farm samples came at too great of a cost for several analytes. Therefore, the ICP-MS method as used for the SIA Prototype should be applied to the Brawner Farm samples.

Furthermore, although Hg was previously determined using concentrated HNO_3 in soil core 6A,[36] the work done here studying the metal oxide at 6A was inconclusive. Future work should re-examine the four Sequential Extraction steps by using the MAE BCR method to isolate which fractions contain Hg. Increasing ramp times in the MAE method should also be examined to determine whether Hg shows the same bi-modal behavior as revealed in previous work.[36]

Additional methods could be explored in subsequent work as well. While the BCR technique is capable of showing the type of interaction (mobile, carbonate, metal oxide, organic), it is not capable of determining the size and distribution of the particles to which they are attached. There are multiple approaches (elastic scattering spectroscopies) that should be explored to address metal speciation in relation to particle size.[95-97]

Rate zonal centrifugation is a relatively inexpensive and an accessible separation technique.[106] With rate zonal centrifugation, a centrifuge tube is filled with different layers of varying densities and a zone of sample placed on top. When centrifuged, the particles travel at different rates and appear as specific zones in the sample tube. For example, the fractionation of 20, 30, 40, 60, 80, 150, and 250 nm particles has been achieved.[97] However, a drawback to this method is that density variability in the soil sample can prove problematic.[96] Nonetheless, after separation a multitude of analytical techniques such as AAS or ICP-MS may be used to determine the speciation of analytes.

Another separation technique is Field-Flow Fractionation (FFF).[96] FFF uses a narrow channel with two forces acting upon it. A convective force is created by the pumping of aqueous carrier along the channel axis where a second force acts orthogonal to it. The orthogonal force can take many forms (magnetic, electrical, centrifugal, or another pumped solution). The combination of these two forces is then used to separate particles based upon their size and shape. Potential advantages include better fractionation resolution compared to other separation techniques (such as dialysis and filtration). Another advantage is the ability to couple

the FFF instrument directly to detectors such as particle analyzers, atomic

spectrometers,[107] and mass spectrometers.[108]

Literature Cited:

1) *Elements and their Compounds in the Environment: Occurrence, Analysis and Biological Relevance*; Merian, E., Anke, M., Ihnat, M., Stoeppler, M., Eds.; Wiley-VCH: Weinheim, 2004.

2) *Environmental Chemistry*; Baird, C; W.H. Freeman: New York, 1998.

3) Mercury and health. https://www.who.int/news-room/fact-sheets/detail/mercury-and-health.

4) Little, B. Killer Clothing Was All the Rage In the 19th Century. https://www.nationalgeographic.com/news/2016/10/dress-hat-fashion-clothing-mercury-arsenic-poison-history/ (accessed 2020).

5) NIH. Mercuric nitrate. https://pubchem.ncbi.nlm.nih.gov/compound/Mercuric-nitrate (accessed 2020).

6) Nix, E. Where did the phrase "mad as a hatter" come from? https://www.history.com/news/where-did-the-phrase-mad-as-a-hatter-come-from (accessed 2020).

7) National Primary Drinking Water Regulations. https://www.epa.gov/ground-water-and-drinking-water/national-primary-drinking-water-regulations (accessed 2020).

8) npwdr_complete_table.pdf https://www.epa.gov/sites/production/files/2016-06/documents/npwdr_complete_table.pdf (accessed 2020).

9) Peitzman, S. J. The Flame Photometer as Engine of Nephrology: A Biography. *American Journal of Kidney Diseases* **2010**, *56* (2), 379–386.

10) A Guide to Single Channel Flame Photometer Analysis. http://www.sherwood-scientific.com/flame/flameanalysis.html (accessed 2020).

11) Skoog, D. A.; Crouch, S. R.; Holler, F. J. *Principles of Instrumental Analysis*, 6th ed.; Thomson Brooks/Cole: Belmont, CA, 2007.

12) Robinson, J. W. *Atomic Spectroscopy*, 2nd ed.; Marcel Dekker: New York, 1996.

13) Method 7000B. https://www.epa.gov/sites/production/files/2015-12/documents/7000b.pdf (accessed 2020).

14) Bobaker, A. M.; Alakili, I.; Sarmani, S. B.; Al-Ansari, N.; Yaseen, Z. M. Determination and Assessment of the Toxic Heavy Metal Elements Abstracted from the Traditional Plant Cosmetics and Medical Remedies: Case Study of Libya. *International Journal of Environmental Research and Public Health* **2019**, *16* (11).

15) Skoog, D. A.; Holler, F. J.; Crouch, S. R. *Principles of Instrumental Analysis*, 7th ed.; Cengage Learning: Australia, 2018.

16) Coverly, S. In *Encyclopedia of Analytical Science*; Worsfold, P. J., Poole, C. F., Townshend, A., Eds.; Elsevier/Acad. Press: Amsterdam, 2005; pp 210–216.

17) Ruzicka, J.; Hansen, E. H. Retro-Review of Flow-Injection Analysis. *TrAC Trends in Analytical Chemistry* **2008**, *27* (5), 390–393.

18) Ruzicka, J. Concentration Gradient. https://www.flowinjectiontutorial.com/Introduction%20I.3.%20The%20Concentration%20Gradient.html (accessed 2020).

19) Ruzicka, J.; Marshall, G. D. Sequential Injection: a New Concept for Chemical Sensors, Process Analysis and Laboratory Assays. *Analytica Chimica Acta* **1990**, *237*, 329–343.

20) Fang, Z. *Flow Injection Separation and Preconcentration*; VCH: Weinheim, Germany, 1993.

21) Ruzicka, J. Configurations of SIA Systems. https://flowinjectiontutorial.com/Methods%202.1.4.%20Configurations%20of%20SIA%20Systems.html (accessed 2020).

22) Sequential Injection Analysis. https://www.flowinjection.com/images/Sequential_Injection.pdf (accessed 2020).

23) Fenske, Tyler G., "A Study in Molecular Recognition: Synthesis of a B-sheet Mimic & Quantitation of Metal Ions in Aqueous Solutions Through Solid Supported Semi-selective Chemosensors" (2019). Theses and Dissertations.

24) Ruzicka, J. Straight Open Pipes. https://flowinjectiontutorial.com/Theory%200.2.2.%20Straight%20Open%20Pipes.html (accessed 2020).

25) Ruzicka, J. Dispersion in FIA System. https://flowinjectiontutorial.com/Theory%200.2.4.%20Dispersion%20in%20FIA%20System.html (accessed 2020).

26) Ruzicka, J. Flow Programming. https://flowinjectiontutorial.com/Methods%202.1.2.%20Flow%20Programming.html (accessed 2020).

27) Aldstadt, J. H.; Olson, D. C.; Wolcott, D. K.; Marshall, G. D.; Stieg, S. W. Flow and Sequential Injection Analysis Techniques in Process Analysis. *Encyclopedia of Analytical Chemistry* **2006**.

28) Upadhyay, S.; Singh, A.; Sinha, R.; Omer, S.; Negi, K. Colorimetric Chemosensors for d-Metal Ions: A Review in the Past, Present and Future Prospect. *Journal of Molecular Structure* **2019**, *1193*, 89–102.

29) Gogoi, N.; Barooah, M.; Majumdar, G.; Chowdhury, D. Carbon Dots Rooted Agarose Hydrogel Hybrid Platform for Optical Detection and Separation of Heavy Metal Ions. *Applied Materials & Interfaces* **2015**, *7* (5), 3058–3067.

30) Karlsson, J. K. G.; Woodford, O. J.; Al-Aqar, R.; Harriman, A. Effects of Temperature and Concentration on the Rate of Photobleaching of Erythrosine in Water. *The Journal of Physical Chemistry A* **2017**, *121* (45), 8569–8576.

31) Eggeling, C.; Widengren, J.; Rigler, R.; Seidel, C. A. M. Photobleaching of Fluorescent Dyes under Conditions Used for Single-Molecule Detection: Evidence of Two-Step Photolysis. *Analytical Chemistry* **1998**, *70* (13), 2651–2659.

32) https://www.flowinjection.com/hardware/flow-cells/sma-z-series (accessed 2020).

33) At Second Manassas, Stonewall Jackson's Attack On Brawner's Farm Ended In A Bloody Stalemate. https://nationalinterest.org/blog/reboot/second-manassas-stonewall-jacksons-attack-brawners-farm-ended-bloody-stalemate-169524 (accessed 2020).

34) Potter, S.R., Sonderman, R.C., Creveling, M.C., Dean, S.L., *"No Maneuvering and Very Little Tactics: Archaeology and the Battle of Brawner Farm"*, Gainesville, FL, 2000.

35) Schlipp, S. A. Determination of Trace Levels of Pb(II) in Battlefield Soil Extracts by Sequential Extraction and Electrothermal Atomic Absorption Spectroscopy. dissertation, 2011.

36) Salske, S. C. Speciation, Transport, and Fate of Heavy Metals in Soils from a Civil War Battlefield: Development of a Novel MAE-GF-AAS Method. dissertation, 2020.

37) Brain, M. The Flintlock's Replacement: Percussion Cap. https://science.howstuffworks.com/flintlock5.htm (accessed 2020).

38) Fadala, S., *"The Complete Blackpowder Handbook"*, 5th ed.; DBI Books: 1996; Vol. 41.

39) Winant, L., *"Early Percussion Firearms; a History of Early Percussion Firearms Ignition, from Forsyth to Winchester"*, N.Y. Morrow: 1959.

40) Graydon, J. A.; Louis, V. L. S.; Hintelmann, H.; Lindberg, S. E.; Sandilands, K. A.; Rudd, J. W. M.; Kelly, C. A.; Tate, M. T.; Krabbenhoft, D. P.; Lehnherr, I. Investigation of Uptake and Retention of Atmospheric Hg(II) by Boreal Forest Plants

Using Stable Hg Isotopes. *Environmental Science & Technology* **2009**, *43* (13), 4960–4966.

41) Hintelmann, H.; Harris, R.; Heyes, A.; Hurley, J. P.; Kelly, C. A.; Krabbenhoft, D. P.; Lindberg, S.; Rudd, J. W. M.; Scott, K. J.; St.louis, V. L. Reactivity and Mobility of New and Old Mercury Deposition in a Boreal Forest Ecosystem during the First Year of the METAALICUS Study. *Environmental Science & Technology* **2002**, *36* (23), 5034–5040.

42) Graydon, J. A.; Louis, V. L. S.; Hintelmann, H.; Lindberg, S. E.; Sandilands, K. A.; Rudd, J. W. M.; Kelly, C. A.; Hall, B. D.; Mowat, L. D. Long-Term Wet and Dry Deposition of Total and Methyl Mercury in the Remote Boreal Ecoregion of Canada. *Environmental Science & Technology* **2008**, *42* (22), 8345–8351.

43) USGS. The METAALICUS project. https://wi.water.usgs.gov/mercury/metaalicus-project.html (accessed 2020).

44) USGS. *Aerial photo of lake*.

45) Mowat, L. D.; Louis, V. L. S.; Graydon, J. A.; Lehnherr, I. Influence of Forest Canopies on the Deposition of Methylmercury to Boreal Ecosystem Watersheds. *Environmental Science & Technology* **2011**, *45* (12), 5178–5185.

46) Graydon, J. A.; Louis, V. L. S.; Lindberg, S. E.; Hintelmann, H.; Krabbenhoft, D. P. Investigation of Mercury Exchange between Forest Canopy Vegetation and the Atmosphere Using a New Dynamic Chamber†. *Environmental Science & Technology* **2006**, *40* (15), 4680–4688.

47) Hrenchuk, L. E.; Blanchfield, P. J.; Paterson, M. J.; Hintelmann, H. H. Dietary and Waterborne Mercury Accumulation by Yellow Perch: A Field Experiment. *Environmental Science & Technology* **2011**, *46* (1), 509–516.

48) Walleghem, J. L. A. V.; Blanchfield, P. J.; Hintelmann, H. Elimination of Mercury by Yellow Perch in the Wild. *Environmental Science & Technology* **2007**, *41* (16), 5895–5901.

49) Aragay, G.; Pons, J.; Merkoçi, A. Recent Trends in Macro-, Micro-, and NanomaterialBased Tools and Strategies for Heavy-Metal Detection. Chem. Rev. 2011, 111 (5), 3433– 3458.

50) Labeots, J. T. A Real-time Approach to Process Monitoring of Heavy Metals: Spectrophotometric Characterization and Application of Novel Azo Dyes. thesis, 2019.

51) Jespersen, H. Second Bull Run Aug28. *cwmaps*, 2013.

52) Sutherland, R., Tack, F. Fractionation of Cu, Pb and Zn in certified reference soils SRM 2710 and SRM 2711 using the optimized BCR sequential extraction procedure. Elsevier. 2003, 8, 37-50.

53) Thomas, R. A Beginner's Guide to ICP-MS Part XII — A Review of Interferences. *Spectroscopy* **2002**, *17* (10), 24–31.

54) Winter, M. Zinc: isotope data. https://www.webelements.com/zinc/isotopes.html (accessed 2020).

55) Winter, M. Nickel: isotope data. https://www.webelements.com/nickel/isotopes.html (accessed 2020).

56) Winter, M. Germanium: isotope data. https://www.webelements.com/germanium/isotopes.html (accessed 2020).

57) May, T. W.; Wiedmeyer, R. H. A Table of Polyatomic Interferences in ICP-MS. *Atomic Spectroscopy* **1998**, *19* (5), 150–155.

58) USGS; Fatah , H. A. National Minerals Information Center: Reston, VA, 2020; pp 1–10.

59) Aqueous Metal Ions. https://www.chem.purdue.edu/jmol/cchem/aqua2.html (accessed 2020).

60) Winter, M. Zinc: radii of atoms and ions. https://www.webelements.com/zinc/atom_sizes.html (accessed 2020).

61) Alum and Ferric Chloride: Pros, Cons, and Substitutes for Treating Water. https://atsinnovawatertreatment.com/blog/alum-and-ferric-chloride-substitutes/ (accessed 2020).

62) Winter, M. Iron: radii of atoms and ions. https://www.webelements.com/iron/atom_sizes.html (accessed 2020).

63) Jaskula, B. W. mcs2020.pdf - Mineral Commodity Summaries 2020. https://pubs.usgs.gov/periodicals/mcs2020/mcs2020-gallium.pdf (accessed 2020).

64) National Minerals Information Center. https://www.usgs.gov/centers/nmic/gallium-statistics-and-information (accessed 2020).

65) Winter, M. Gallium: radii of atoms and ions. https://www.webelements.com/gallium/atom_sizes.html (accessed 2020).

66) Praphairaksit, N.; Houk, R. S. Reduction of Space Charge Effects in Inductively Coupled Plasma Mass Spectrometry Using a Supplemental Electron Source inside the Skimmer: Ion Transmission and Mass Spectral Characteristics. *Analytical Chemistry* **2000**, *72* (11), 2356–2361.

67) Praphairaksit, N.; Houk, R. S. Attenuation of Matrix Effects in Inductively Coupled Plasma Mass Spectrometry with a Supplemental Electron Source inside the Skimmer. *Analytical Chemistry* **2000**, *72* (11), 2351–2355.

68) Winter, M. Barium: radii of atoms and ions. https://www.webelements.com/barium/atom_sizes.html (accessed 2020).

69) Water treatment. https://www.bsef.com/uses-innovations/water-treatment/ (accessed 2020).

70) Tessier, A., Campbell, P.G.C., Bisson, M. "Sequential Extraction Procedure for the Speciation of Particulate Trace Metals", *Journal of Analyitical Chemistry* **1979,** *51,* 844-851.

71) Kheboian, C.; Bauer, C. F. Accuracy of Selective Extraction Procedures for Metal Speciation in Model Aquatic Sediments. *Analytical Chemistry* **1987**, *59* (10), 1417–1423.

72) Reid, M. K.; Spencer , K. L.; Shotbolt, L. An Appraisal of Microwave-Assisted Tessier and BCR Sequential Extraction Methods for the Analysis of Metals in Sediments and Soils. *Journal of Soils and Sediments* **2011**, *11*, 518–528.

73) *"CEM Corporation MARS 5 Microwave Accelerated Reaction System Operation Manual"*, Rev. 0 ed.; CEM Corporation: Matthews, North Carolina, 1999.

74) Howey, A. W. Minie Ball. https://www.historynet.com/minie-ball (accessed 2020).

75) National Parks Service. Firing Black Powder Rifles. https://www.nps.gov/vick/planyourvisit/firing-black-powder-rifles.htm (accessed 2020).

76) RCS. Manganese - Element information, properties and uses: Periodic Table. https://www.rsc.org/periodic-table/element/25/manganese (accessed 2020).

77) USGS; Grossman, J. *Analysis for Manganese (Mn) in the National Geochemical Survey database*, 2016.

78) RCS. Iron - Element information, properties and uses: Periodic Table. https://www.rsc.org/periodic-table/element/26/iron (accessed 2020).

79) USGS; Grossman, J. *Analysis for Iron (Fe) in the National Geochemical Survey database*, 2016.

80) RCS. Cobalt - Element information, properties and uses: Periodic Table. https://www.rsc.org/periodic-table/element/27/cobalt (accessed 2020).

81) USGS; Grossman, J. *Analysis for Cobalt (Co) in the National Geochemical Survey database*, 2018.

82) Echols, M.; Arbittier, D. USA Hosp. Dept. cobalt blue oval bottle. http://www.medicalantiques.com/civilwar/Civil_War_Articles/U_S_A_Hosp_Dept_cobalt_blue_oval_bottle.htm (accessed 2020).

83) Bowey, A. M. Cobalt Blue Glass from the Glass Encyclopedia. http://www.glassencyclopedia.com/cobaltglass.html (accessed 2020).

84) RCS. Nickel - Element information, properties and uses: Periodic Table. https://www.rsc.org/periodic-table/element/28/nickel (accessed 2020).

85) USGS; Grossman, J. *Analysis for Nickel (Ni) in the National Geochemical Survey database*, 2016.

86) RCS. Copper - Element information, properties and uses: Periodic Table. https://www.rsc.org/periodic-table/element/29/copper (accessed 2020).

87) USGS; Grossman, J. *Analysis for Copper (Cu) in the National Geochemical Survey database*, 2016.

88) RCS. Zinc - Element information, properties and uses: Periodic Table. https://www.rsc.org/periodic-table/element/30/zinc (accessed 2020).

89) USGS; Grossman, J. *Analysis for Zinc (Zn) in the National Geochemical Survey database*, 2016.

90) RCS. Gallium - Element information, properties and uses: Periodic Table. https://www.rsc.org/periodic-table/element/31/gallium (accessed 2020).

91) USGS; Grossman, J. *Analysis for Gallium (Ga) in the National Geochemical Survey database*, 2016.

92) RCS. Barium - Element information, properties and uses: Periodic Table. https://www.rsc.org/periodic-table/element/56/barium (accessed 2020).

93) USGS; Grossman, J. *Analysis for Barium (Ba) in the National Geochemical Survey database*, 2018.

94) RCS. Lanthanum - Element information, properties and uses: Periodic Table. https://www.rsc.org/periodic-table/element/57/lanthanum (accessed 2020).

95) USGS; Grossman, J. *Analysis for Lanthanum (La) in the National Geochemical Survey database*, 2018.

96) RCS. Cerium - Element information, properties and uses: Periodic Table. https://www.rsc.org/periodic-table/element/58/cerium (accessed 2020).

97) USGS; Grossman, J. *Analysis for Cerium (Ce) in the National Geochemical Survey database*, 2016.

98) RCS. Gold - Element information, properties and uses: Periodic Table. https://www.rsc.org/periodic-table/element/79/gold (accessed 2020).

99) USGS; Grossman, J. *Analysis for Gold (Au) in the National Geochemical Survey database*, 2018.

100) RCS. Mercury - Element information, properties and uses: Periodic Table. https://www.rsc.org/periodic-table/element/80/mercury (accessed 2020).

101) USGS; Grossman, J. *Analysis for Mercury (Hg) in the National Geochemical Survey database*, 2016.

102) RCS. Lead - Element information, properties and uses: Periodic Table. https://www.rsc.org/periodic-table/element/82/lead (accessed 2020).

103) USGS; Grossman, J. *Analysis for Lead (Pb) in the National Geochemical Survey database*, 2016.

104) Nriagu, J. O. The Rise and Fall of Leaded Gasoline. *Science of The Total Environment* **1989**, *92*, 13–28.

105) U.S. Energy Information Administration - EIA - Independent Statistics and Analysis. https://www.eia.gov/energyexplained/gasoline/gasoline-and-the-environment-leaded-gasoline.php (accessed 2020).

106) Ermolin, M. S.; Fedotov, P. S. Separation and Characterization of Environmental Nano- and Submicron Particles. *Reviews in Analytical Chemistry* **2016**, *35* (4), 185–199.

107) Santoro, A.; Terzano, R.; Medici, L.; Beciani, M.; Pagnoni, A.; Blo, G. Colloidal Mercury (Hg) Distribution in Soil Samples by Sedimentation Field-Flow Fractionation Coupled to Mercury Cold Vapour Generation Atomic Absorption Spectroscopy. *Journal of Environmental Monitoring* **2012**, No. 14, 138–145.

108) Hassellöv, M.; Lyvén, B.; Haraldsson, C.; Sirinawin, W. Determination of Continuous Size and Trace Element Distribution of Colloidal Material in Natural Water by On-Line Coupling of Flow Field-Flow Fractionation with ICPMS. *Analytical Chemistry* **1999**, No. 71, 3497–3502.
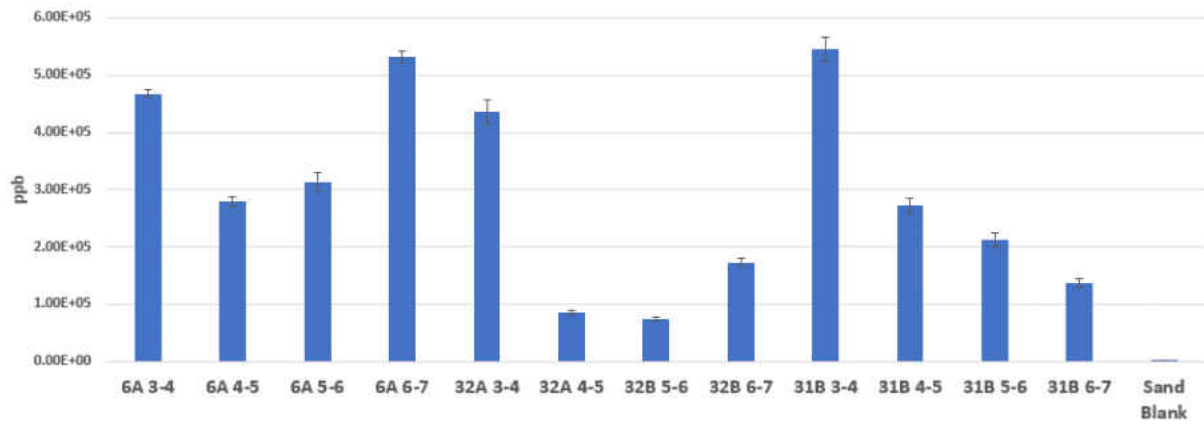
Appendix

Figure A1. Mn distribution in soil. Error bars represent the Student's t value at the 95% confidence interval (n = 3).

	Average (ppb)	95% (n=3)
6A 3-4	4.68E+05	6.63E+03
6A 4-5	2.79E+05	7.42E+03
6A 5-6	3.13E+05	1.63E+04
6A 6-7	5.33E+05	9.92E+03
32A 3-4	4.35E+05	2.14E+04
32A 4-5	8.62E+04	3.35E+03
32B 5-6	7.40E+04	4.21E+03
32B 6-7	1.73E+05	6.78E+03
31B 3-4	5.45E+05	2.20E+04
31B 4-5	2.72E+05	1.33E+04
31B 5-6	2.13E+05	1.30E+04
31B 6-7	1.36E+05	7.64E+03
Sand Blank	8.60E+02	8.24E+02

Table A1. Values for the Mn distribution in soil shown in Figure A1.

Figure A2. Fe distribution in soil. Error bars represent the Student's t value at the 95% confidence interval (n = 3).

	Average (ppb)	95% (n=3)
6A 3-4	2.18E+06	2.75E+04
6A 4-5	2.45E+06	1.34E+04
6A 5-6	2.50E+06	6.99E+04
6A 6-7	4.44E+06	8.62E+04
32A 3-4	2.55E+06	9.08E+04
32A 4-5	3.92E+06	6.44E+04
32B 5-6	3.31E+06	7.98E+04
32B 6-7	2.92E+06	5.05E+04
31B 3-4	2.43E+06	5.50E+04
31B 4-5	1.96E+06	7.76E+04
31B 5-6	2.38E+06	8.29E+04
31B 6-7	1.85E+06	5.74E+04
Sand Blank	7.04E+03	1.48E+03

Table A2. Values for the Fe distribution in soil shown in Figure A2.
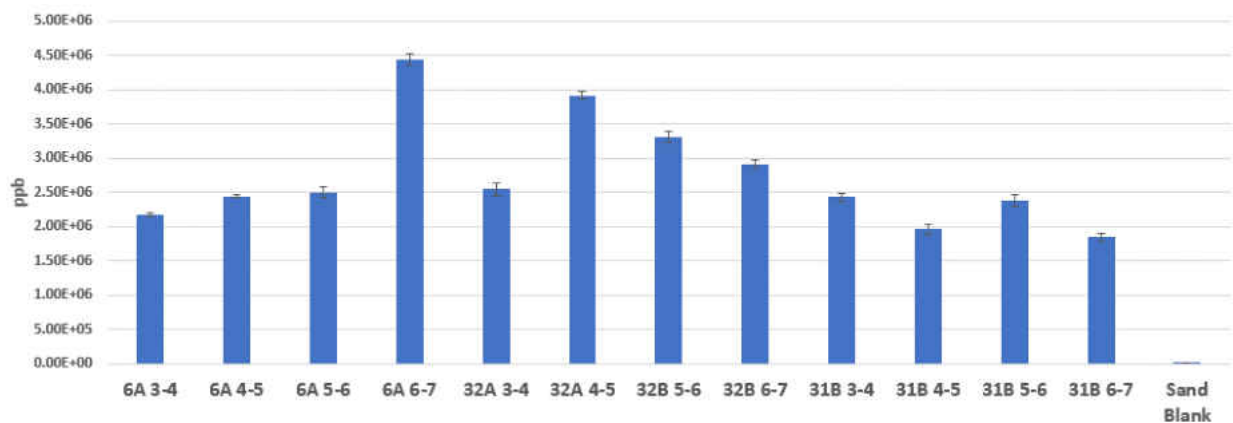
Figure A3. Co distribution in soil. Error bars represent the Student's t value at the 95% confidence interval (n = 3).

	Average (ppb)	95% (n=3)
6A 3-4	6.34E+04	1.78E+03
6A 4-5	3.89E+04	1.22E+03
6A 5-6	4.24E+04	2.41E+03
6A 6-7	8.38E+04	2.46E+03
32A 3-4	7.21E+04	4.14E+03
32A 4-5	2.19E+04	1.85E+03
32B 5-6	3.86E+04	1.94E+03
32B 6-7	4.15E+04	1.34E+03
31B 3-4	6.89E+04	2.12E+03
31B 4-5	4.05E+04	1.95E+03
31B 5-6	4.26E+04	3.03E+03
31B 6-7	3.46E+04	2.38E+03
Sand Blank	8.22E+02	8.14E+02

Table A3. Values for the Co distribution in soil shown in Figure A3.
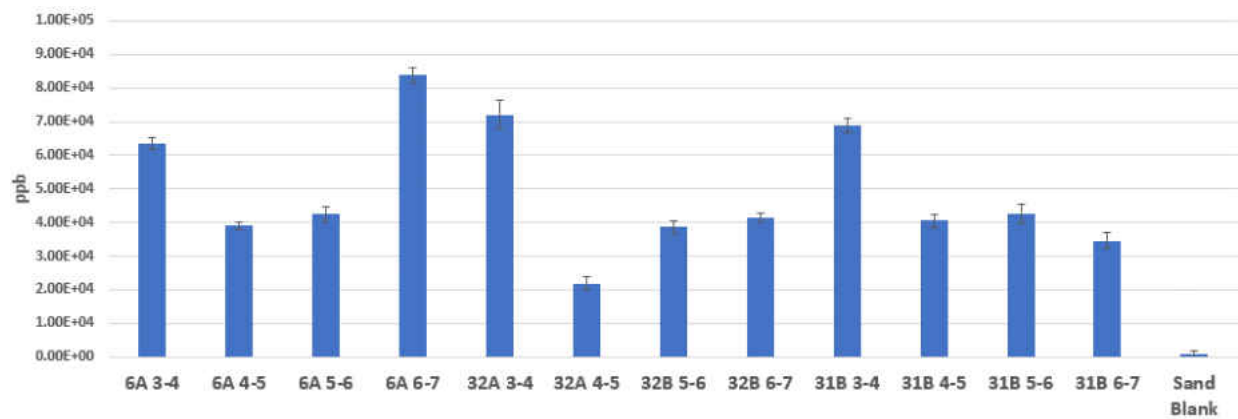
Figure A4. Ni distribution in soil. Error bars represent the Student's t value at the 95% confidence interval (n = 3).

	Average (ppb)	95% (n=3)
6A 3-4	7.54E+03	2.91E+03
6A 4-5	5.80E+03	2.95E+03
6A 5-6	5.95E+03	3.03E+03
6A 6-7	1.01E+04	4.44E+03
32A 3-4	9.92E+03	4.22E+03
32A 4-5	7.59E+03	4.12E+03
32B 5-6	8.38E+03	4.34E+03
32B 6-7	1.58E+04	4.20E+03
31B 3-4	9.86E+03	4.07E+03
31B 4-5	7.11E+03	3.79E+03
31B 5-6	7.29E+03	4.04E+03
31B 6-7	5.15E+03	3.69E+03
Sand Blank	3.58E+03	3.40E+03

Table A4. Values for the Ni distribution in soil shown in Figure A4.
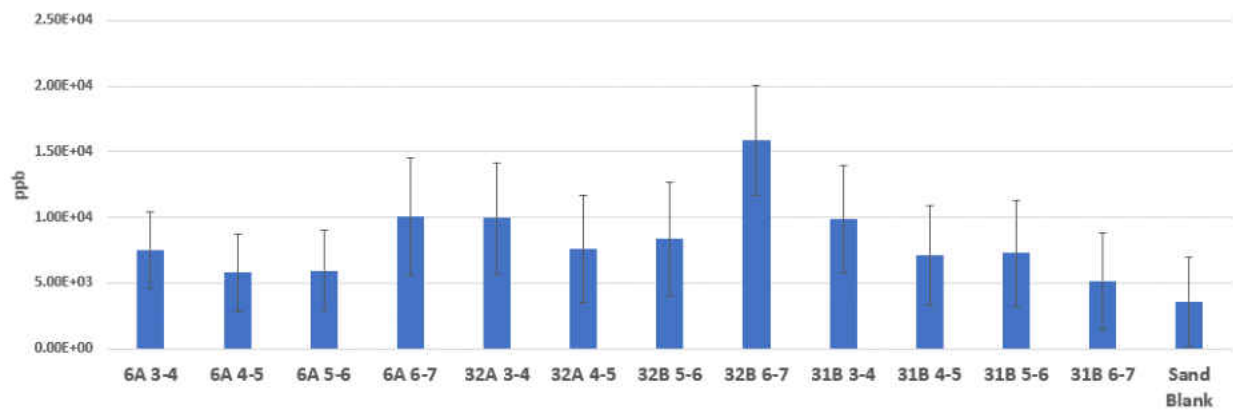
Figure A5. Cu distribution in soil. Error bars represent the Student's t value at the 95% confidence interval (n = 3).

	Average (ppb)	95% (n=3)
6A 3-4	4.37E+03	8.06E+03
6A 4-5	5.89E+03	1.14E+04
6A 5-6	5.01E+03	9.50E+03
6A 6-7	7.24E+03	1.35E+04
32A 3-4	9.60E+03	1.87E+04
32A 4-5	1.05E+04	2.07E+04
32B 5-6	1.15E+04	2.28E+04
32B 6-7	1.25E+04	2.49E+04
31B 3-4	6.11E+03	1.12E+04
31B 4-5	5.05E+03	9.08E+03
31B 5-6	6.64E+03	1.24E+04
31B 6-7	5.08E+03	9.29E+03
Sand Blank	1.68E+03	2.07E+03

Table A5 Values for the Cu distribution in soil shown in Figure A5.
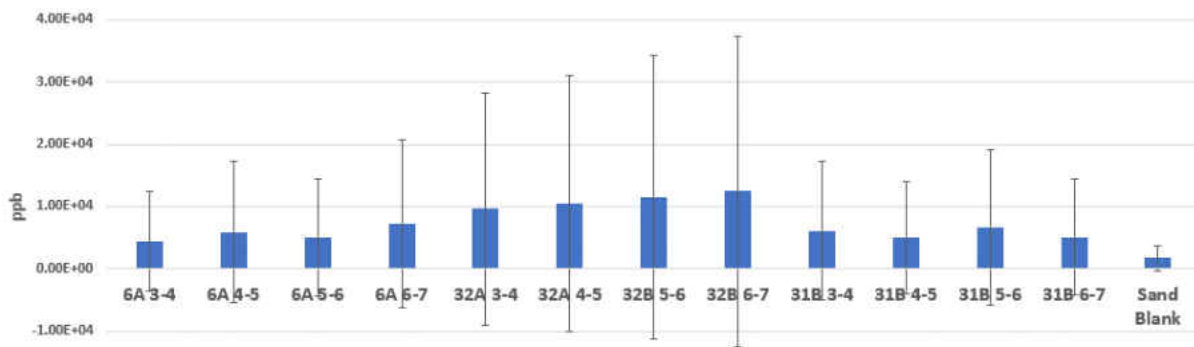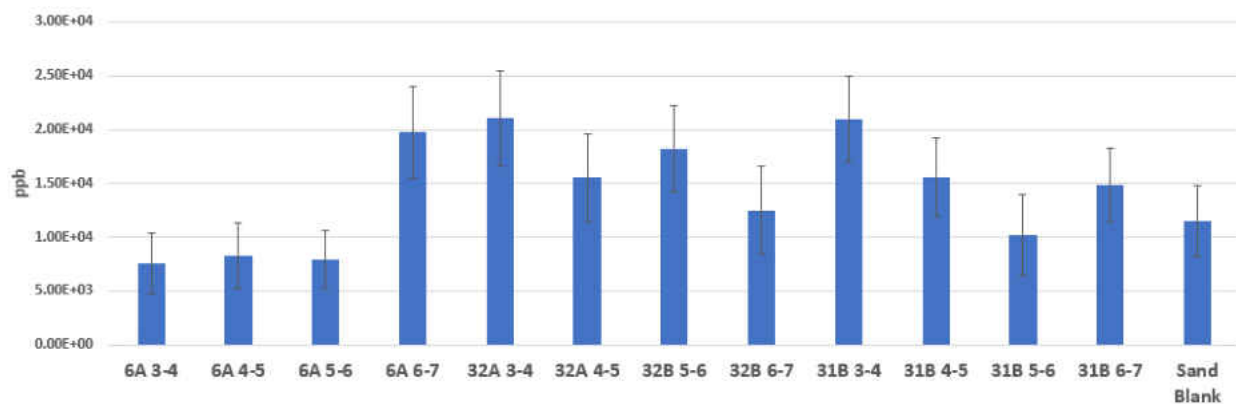
Figure A6. Zn distribution in soil. Error bars represent the Student's t value at the 95% confidence interval (n = 3).

	Average (ppb)	95% (n=3)
6A 3-4	7.53E+03	2.79E+03
6A 4-5	8.29E+03	3.06E+03
6A 5-6	7.91E+03	2.66E+03
6A 6-7	1.98E+04	4.28E+03
32A 3-4	2.10E+04	4.46E+03
32A 4-5	1.55E+04	4.06E+03
32B 5-6	1.82E+04	4.01E+03
32B 6-7	1.25E+04	4.08E+03
31B 3-4	2.10E+04	3.99E+03
31B 4-5	1.56E+04	3.63E+03
31B 5-6	1.02E+04	3.76E+03
31B 6-7	1.48E+04	3.42E+03
Sand Blank	1.15E+04	3.30E+03

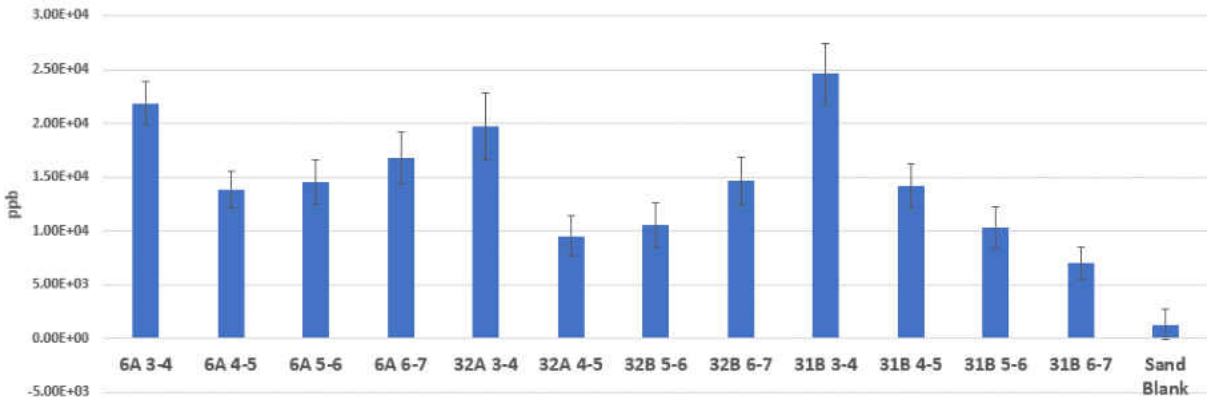Table A6. Values for the Zn distribution in soil shown in Figure A6.

Figure A7. Ga distribution in soil. Error bars represent the Student's t value at the 95% confidence interval (n = 3).

	Average (ppb)	95% (n=3)
6A 3-4	2.18E+04	1.99E+03
6A 4-5	1.39E+04	1.71E+03
6A 5-6	1.45E+04	2.10E+03
6A 6-7	1.68E+04	2.39E+03
32A 3-4	1.97E+04	3.13E+03
32A 4-5	9.53E+03	1.86E+03
32B 5-6	1.06E+04	2.04E+03
32B 6-7	1.46E+04	2.19E+03
31B 3-4	2.46E+04	2.83E+03
31B 4-5	1.42E+04	2.11E+03
31B 5-6	1.03E+04	1.97E+03
31B 6-7	7.01E+03	1.48E+03
Sand Blank	1.31E+03	1.37E+03

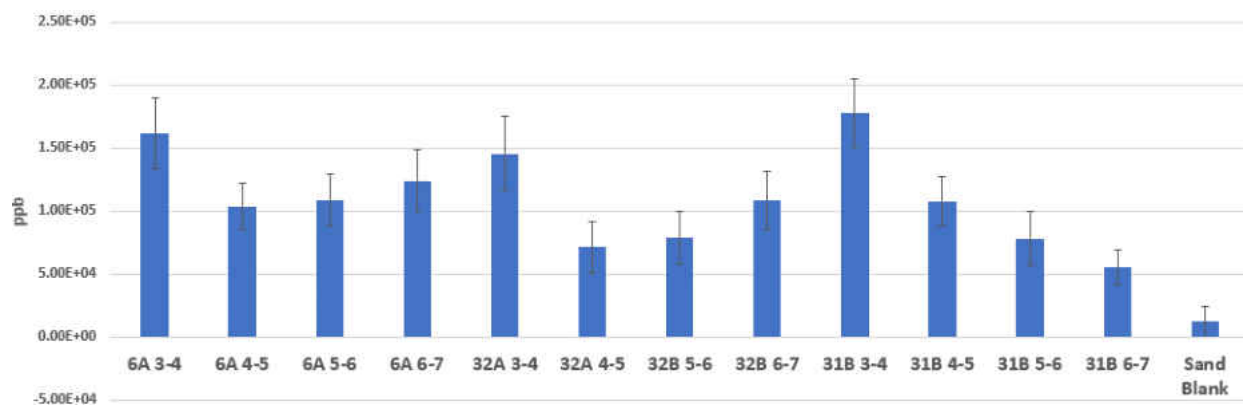Table A7. Values for the Ga distribution in soil shown in Figure A7.

Figure A8. Ba distribution in soil. Error bars represent the Student's t value at the 95% confidence interval (n = 3).

	Average (ppb)	95% (n=3)
6A 3-4	1.61E+05	2.83E+04
6A 4-5	1.04E+05	1.86E+04
6A 5-6	1.09E+05	2.08E+04
6A 6-7	1.24E+05	2.44E+04
32A 3-4	1.46E+05	2.96E+04
32A 4-5	7.14E+04	2.04E+04
32B 5-6	7.90E+04	2.09E+04
32B 6-7	1.09E+05	2.30E+04
31B 3-4	1.78E+05	2.69E+04
31B 4-5	1.08E+05	1.93E+04
31B 5-6	7.84E+04	2.10E+04
31B 6-7	5.53E+04	1.40E+04
Sand Blank	1.22E+04	1.24E+04

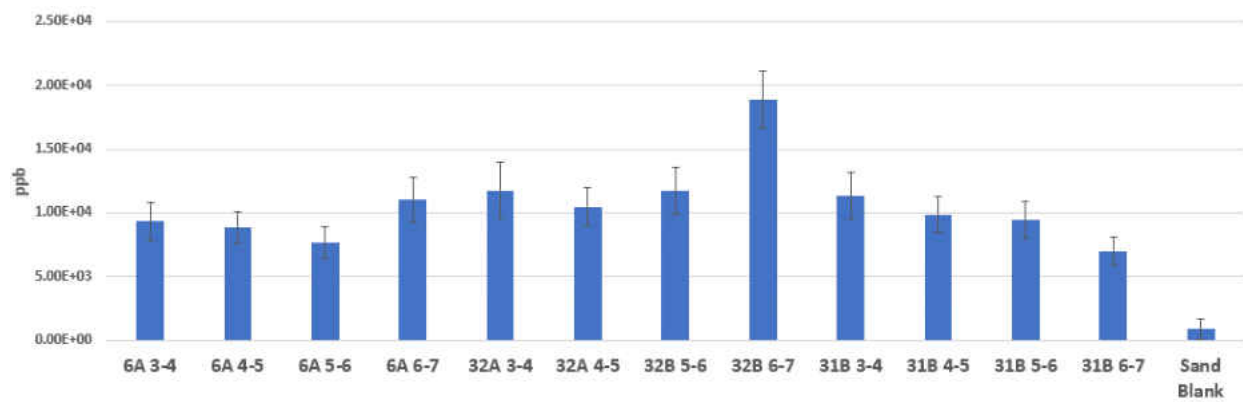Table A8. Values for the Ba distribution in soil shown in Figure A8.

Figure A9. La distribution in soil. Error bars represent the Student's t value at the 95% confidence interval (n = 3).

	Average (ppb)	95% (n=3)
6A 3-4	9.32E+03	1.49E+03
6A 4-5	8.83E+03	1.26E+03
6A 5-6	7.70E+03	1.25E+03
6A 6-7	1.10E+04	1.70E+03
32A 3-4	1.17E+04	2.19E+03
32A 4-5	1.05E+04	1.49E+03
32B 5-6	1.17E+04	1.83E+03
32B 6-7	1.89E+04	2.23E+03
31B 3-4	1.13E+04	1.85E+03
31B 4-5	9.87E+03	1.40E+03
31B 5-6	9.42E+03	1.46E+03
31B 6-7	6.99E+03	1.09E+03
Sand Blank	8.58E+02	8.23E+02

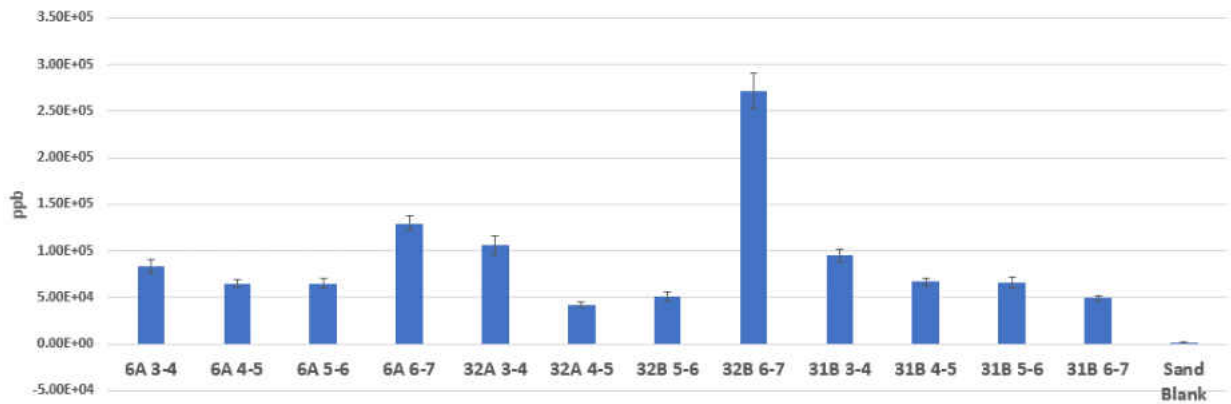Table A9. Values for the La distribution in soil shown in Figure A9.

Figure A10. Ce distribution in soil. Error bars represent the Student's t value at the 95% confidence interval (n = 3).

	Average (ppb)	95% (n=3)
6A 3-4	8.35E+04	7.50E+03
6A 4-5	6.50E+04	4.38E+03
6A 5-6	6.47E+04	5.43E+03
6A 6-7	1.29E+05	7.87E+03
32A 3-4	1.06E+05	1.02E+04
32A 4-5	4.24E+04	2.77E+03
32B 5-6	5.16E+04	4.81E+03
32B 6-7	2.72E+05	1.84E+04
31B 3-4	9.51E+04	6.77E+03
31B 4-5	6.69E+04	3.61E+03
31B 5-6	6.61E+04	6.44E+03
31B 6-7	4.94E+04	2.98E+03
Sand Blank	8.93E+02	9.60E+02

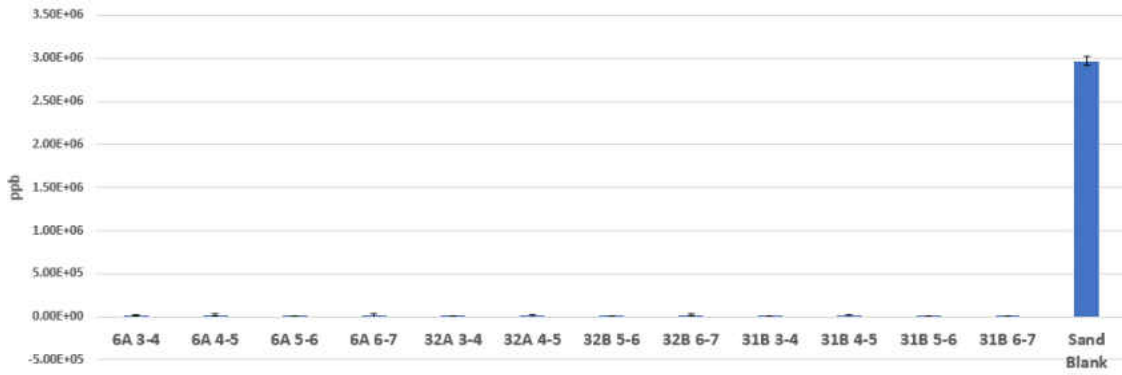Table A10. Values for the Ce distribution in soil shown in Figure A10.

Figure A11. Au distribution in soil. Error bars represent the Student's t value at the 95% confidence interval (n = 3).

	Average (ppb)	95% (n=3)
6A 3-4	1.25E+04	9.74E+03
6A 4-5	1.90E+04	1.29E+04
6A 5-6	8.57E+03	1.60E+03
6A 6-7	1.33E+04	1.80E+04
32A 3-4	1.22E+04	1.34E+03
32A 4-5	1.35E+04	1.36E+04
32B 5-6	1.34E+04	1.29E+03
32B 6-7	1.66E+04	1.48E+04
31B 3-4	4.36E+03	1.52E+03
31B 4-5	1.07E+04	1.21E+04
31B 5-6	9.60E+03	1.97E+03
31B 6-7	6.47E+03	1.42E+03
Sand Blank	2.97E+06	5.09E+04

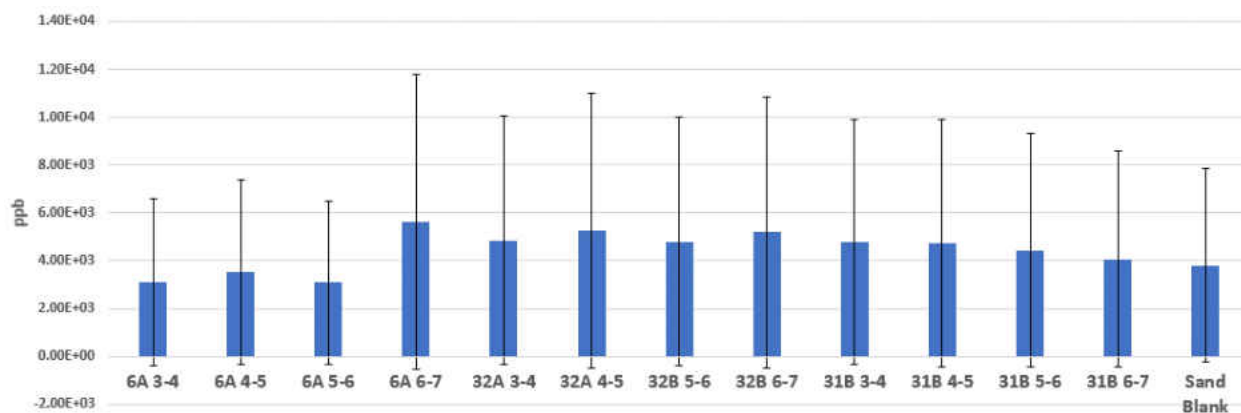Table A11. Values for the Au distribution in soil shown in Figure A11.

Figure A12. Hg distribution in soil. Error bars represent the Student's t value at the 95% confidence interval (n = 3).

	Average (ppb)	95% (n=3)
6A 3-4	3.12E+03	3.48E+03
6A 4-5	3.54E+03	3.86E+03
6A 5-6	3.08E+03	3.39E+03
6A 6-7	5.60E+03	6.17E+03
32A 3-4	4.84E+03	5.20E+03
32A 4-5	5.24E+03	5.75E+03
32B 5-6	4.80E+03	5.21E+03
32B 6-7	5.19E+03	5.68E+03
31B 3-4	4.77E+03	5.11E+03
31B 4-5	4.75E+03	5.18E+03
31B 5-6	4.44E+03	4.86E+03
31B 6-7	4.06E+03	4.52E+03
Sand Blank	3.80E+03	4.05E+03

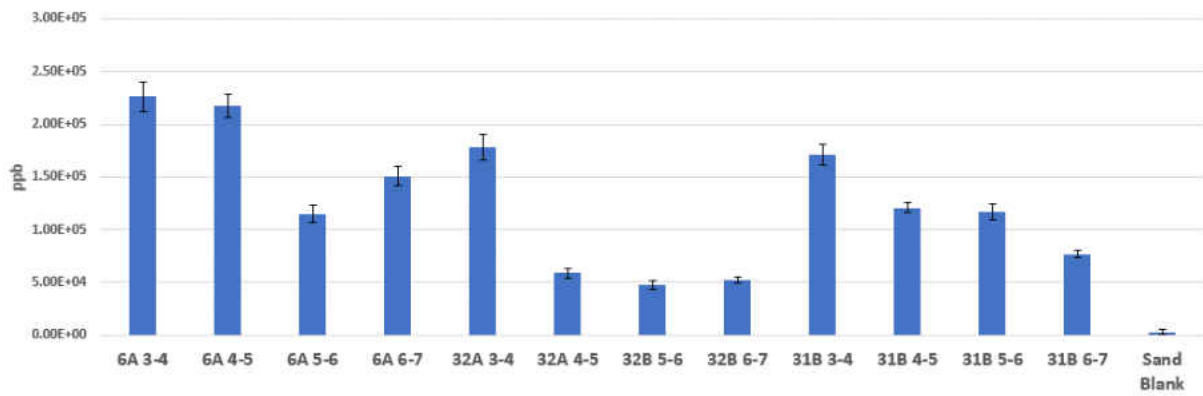Table A12. Values for the Hg distribution in soil shown in Figure A12.

Figure A13. Pb distribution in soil. Error bars represent the Student's t value at the 95% confidence interval (n = 3).

	Average (ppb)	95% (n=3)
6A 3-4	2.26E+05	1.39E+04
6A 4-5	2.17E+05	1.09E+04
6A 5-6	1.15E+05	8.07E+03
6A 6-7	1.51E+05	9.08E+03
32A 3-4	1.78E+05	1.24E+04
32A 4-5	5.85E+04	4.33E+03
32B 5-6	4.79E+04	3.92E+03
32B 6-7	5.22E+04	2.94E+03
31B 3-4	1.71E+05	9.90E+03
31B 4-5	1.20E+05	4.67E+03
31B 5-6	1.17E+05	7.61E+03
31B 6-7	7.67E+04	3.52E+03
Sand Blank	2.89E+03	2.13E+03

Table A13. Values for the Pb distribution in soil shown in Figure A13.
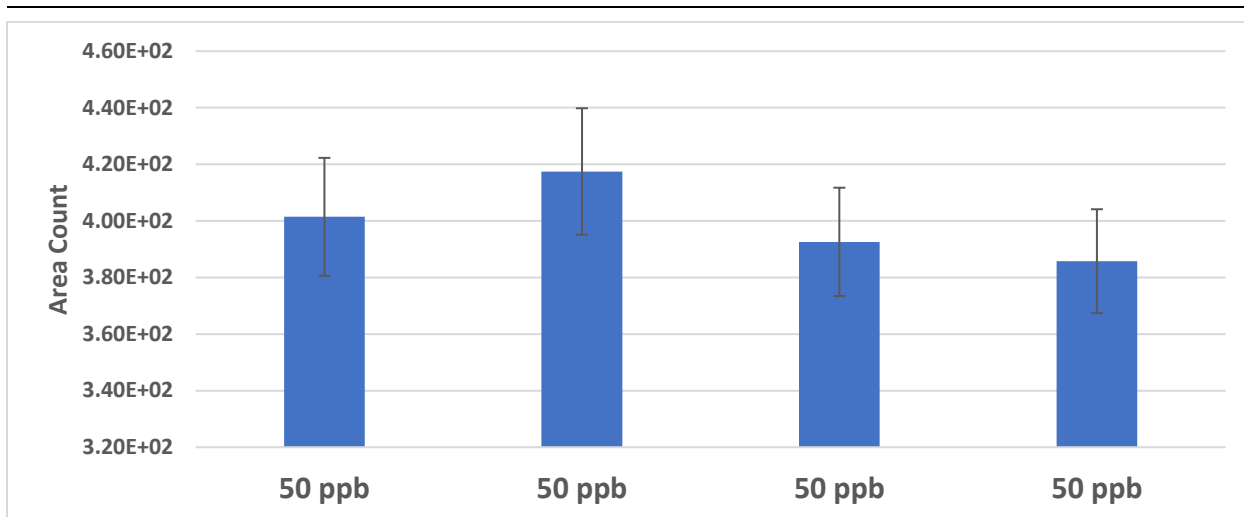
Figure A14. 50 ppb Hg QC samples. All error bars represent the Student's t value at the 95% confidence interval (n=3).

	Average Area Count	95% (n=3)
50 ppb Hg	4.01E+02	2.08E+01
50 ppb Hg	4.17E+02	2.24E+01
50 ppb Hg	3.93E+02	1.92E+01
50 ppb Hg	3.86E+02	1.84E+01

Table A14. Data Table for 50 ppb Hg QC samples in Figure A14. represents the Student's t value at the 95% confidence interval (n = 3).
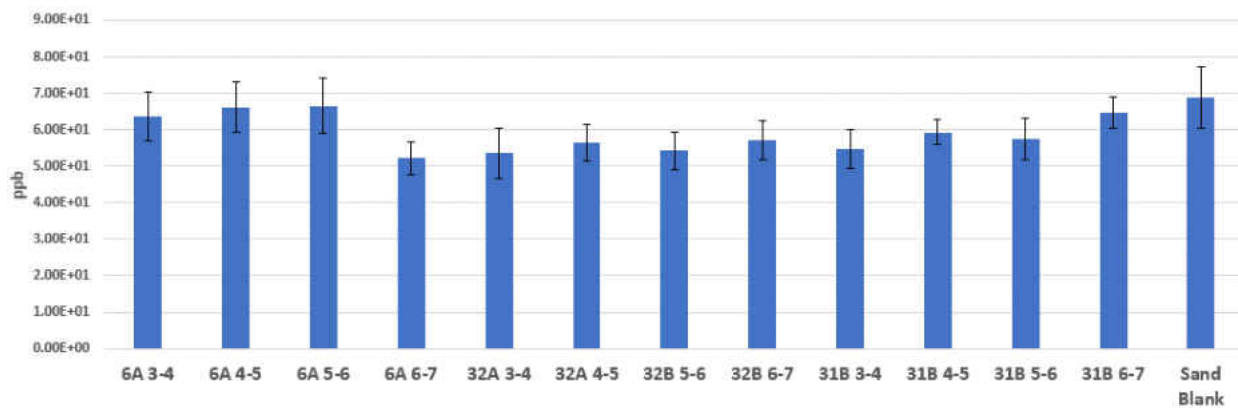
Figure A15. 50 ppb In internal standard tracked across all samples (not internal standard corrected). Error bars represent the Student's t value at the 95% confidence interval (n = 3).

	Average (ppb)	95% (n=3)
6A 3-4	6.36E+01	6.72E+00
6A 4-5	6.62E+01	6.79E+00
6A 5-6	6.65E+01	7.51E+00
6A 6-7	5.22E+01	4.48E+00
32A 3-4	5.35E+01	7.01E+00
32A 4-5	5.65E+01	5.06E+00
32B 5-6	5.42E+01	5.16E+00
32B 6-7	5.72E+01	5.27E+00
31B 3-4	5.47E+01	5.42E+00
31B 4-5	5.94E+01	3.44E+00
31B 5-6	5.75E+01	5.61E+00
31B 6-7	6.47E+01	4.22E+00
Sand Blank	6.89E+01	8.35E+00

Table A15. Values for the In internal standard across soil samples shown in Figure A15.